Atmospheric Pressure Desorption by Impulsive Vibrational Excitation Mass Spectrometry (AP-DIVE-MS)

Dissertation submitted by

Yinfei LU

Dissertation with the aim of achieving a doctoral degree at the

Faculty of Mathematics, Informatics and Natural Sciences

Department of Physics of University of Hamburg

November 2017

Supervisor: Prof. Dr. R.J. Dwayne Miller

co-Supervisor: Prof. Dr. Nils Huse

MPSD – Max Planck Institute for the Structure and Dynamics of Matter

Gutachter der Dissertation: Prof. Dr. R.J. Dwayne Miller

Prof. Dr. Nils Huse

Datum der Disputation: 14.12.2017

Hiermit erkläre ich an Eides statt, dass ich die vorliegende Dissertationsschrift selbst verfasst und keine anderen als die angegebenen Quellen und Hilfsmittle benutzt habe.

I hereby declare, on oath, that I have written the present dissertation by my own and have not used other than the acknowledge resources and aids.

Hamburg, 06.11.2017

.....

(**Yinfei LU**)

Contents

Abstract

Recently it was demonstrated that a picosecond infrared laser (PIRL), with wavelengths centered at 2.94 μm and pulse duration from ten to few hundred picoseconds, can be used for 'soft' laser desorption to eject water-rich samples into the gas phase without inducing compositional or structural changes to biomolecules. PIRL ablation works under the mechanism of desorption by impulsive vibrational excitation (DIVE), where the picosecond pulse duration of PIRL is longer than the thermalization of the vibrational excitation of the OH stretch mode of water and shorter than the thermal diffusion and acoustic expansion times of the excited volume. In addition, a wavelength centered at 2.94 μm is resonant with the OH stretch mode of the water molecule, which is directly coupled to the O-O translational motions via the hydrogen bond interaction, i.e., the very motion needed to drive ablation. Therefore the laser energy of PIRL is most efficiently coupled from the vibrational motions of water molecules into translational motions for ablation without energy leaking out of the excited volume via shock-wave generation or heat propagation. The impulsive heat drives a phase transition of analytes in aqueous solution under superheating condition into the gas phase with minimum damage of the structures for further study by mass spectrometry (MS).

In this doctoral thesis, two home-designed online systems that directly couple PIRL ablation to a Bruker ion trap mass spectrometer in atmospheric pressure will be presented, and the results obtained will be discussed. The first online system exploiting PIRL-DIVE for MS studies, including charging mechanism and detection

limits, is the AP-DIVE-MS with continuous aqueous sample delivery. A bead of aqueous sample was formed in front of the inlet of the MS via a capillary transfer tubing connected to a syringe and a syringe pump with a flow rate comparable to nano-electrospray. Small molecules, molecule mixtures, as well as peptides and proteins in pure water, acidic water and buffer solutions have been extracted by PIRL and directly transferred into the MS inlet for further analysis. The novelty of this interface is that no post-ionization device or nebulizer is needed for obtaining highly charged ions, which is comparable to electrospray. In addition, no high voltage is applied directly to the aqueous solution. The instrumentation, characterization, and main results from AP-DIVE-MS with continuous sample delivery will be introduced and discussed in this thesis. Last but not the least, the potential charging mechanism of AP-DIVE-MS will be discussed in detail by comparing with several existing models, and possible charging processes will be proposed.

The second online system is the AP-DIVE-MS coupled by a lab-on-a-chip (LOC) interface, where picoliter solutions were localized inside a well of 300 nm in depth and 100 μm in diameter. The localized picoliter aqueous sample was then ablated from the back by PIRL, which was aligned to the center of the well and the inlet of the MS. Due to the gradient of surface roughness and instable contact line angle, 'dynamic wetting' was achieved on the picoliter chip by sliding a bead of aqueous sample over the chip arrays. The picoliter chip was aligned and scanned automatically by using a fiducial algorithm developed in our group. The translation stage for chip mounting and the optical shutter control of PIRL were synchronized in order to increase system sensitivity. Ion signals from single-row and single-well scans were obtained and the resulting mass spectra are presented and discussed. Preliminary results from peptides are also presented to highlight the fascinating potential applications of the chip for biomedical analysis using MS. It is noted that limits of detection with this first ambient atmosphere injection system place the sensitivity limits in the 10 attomole range. There are known losses in collection that can be completely avoided by an direct internal MS vacuum interface to improve sensitivity limits by orders of magnitude. This work indicates that detection limits in the zeptomole to single

molecule range needed for single cell analysis are possible.

Zusammenfassung

Kürzlich wurde nachgewiesen, dass ein Pikosekunden-IR-Laser (PIRL), mit einer Zentralwellenlänge von 2.94 μm und einer Pulsdauer von zehn bis zu einigen hundert Pikosekunden, zur 'sanften' Laser-Desorption verwendet werden kann, um wasserreiche Proben direkt in die Gasphase zu bringen, ohne dabei die Zusammensetzung oder Struktur der Biomoleküle zu verändern. PIRL-Ablation erfolgt durch den Mechanismus der impulsiven Anregung intramolekularer Vibrationszustände ('desorption by impulsive vibrational excitation', DIVE), wobei die Pikosekunden-Pulsdauer von PIRL länger als die Thermalisierung der Vibrationsanregung der OH-Streckmode von Wasser und kürzer als die thermische Diffusionszeit und akustische Expansionszeit des angeregten Volumens der Flüssigkeit ist. Desweiteren ist eine Zentralwellenlänge bei 2.94 μm resonant mit der OH-Streckschwingung des Wassermoleküls, die über die Wasserstoffbrücken-Wechselwirkung direkt mit den O-O Translationsbewegungen gekoppelt ist, d.h. mit genau der Bewegung, die die Ablation antreibt. Daher wird die Laserenergie von PIRL am effizientesten von den Schwingungsbewegungen der Wassermoleküle an die Translationsbewegungen für die Ablation gekoppelt, ohne dass dabei Energie aus dem angeregten Volumen durch die Erzeugung von Schockwellen und Wärmeausbreitung entweicht. Die gepulste Hitze treibt einen Phasenübergang von Analyten in wässriger Lösung im überhitzten Zustand in die Gasphase bei minimaler Schädigung ihrer Struktur, um sie anschließend mit Massenspektrometrie (MS) zu untersuchen.

In dieser Dissertation werden zwei selbst designte Online-Systeme vorgestellt, die

PIRL-Ablation direkt mit einem Bruker Ionenfallen-Massenspektrometer unter Atmosphärendruck verbinden, und die damit erzielten Resultate werden diskutiert. Das erste Online-System, das PIRL-DIVE für massenspektroskopische Studien verwendet, inklusive zum Aufladungsmechanismus und Detektionslimit, ist das AP-DIVE-MS (DIVE-Massenspektrometer unter Atmosphärendruck) mit kontinuierlicher Zufuhr von wässrigen Proben. Ein kugelförmiger Tropfen der wässrigen Probe wurde vor der Einlassöffnung des Massenspektrometers mittels eines Transfer-Kapillarröhrchens geformt, das mit einer Spritze verbunden ist. Eine Spritzenpumpe liefert eine kontrollierte Durchflussrate vergleichbar zu der in Nano-Elektrospray. Kleine Moleküle, Molekülmischungen, sowie Peptide und Proteine in reinen Wasser-, in sauren Wasser- und in Pufferlösungen wurden mit PIRL extrahiert und direkt in die Einlassöffnung des Massenspektrometers zur weiteren Analyse transferiert. Die Neuheit dieses Interfaces ist, dass eine Vorrichtung zur Nachionisation oder ein Zerstäuber nicht benötigt wird, um hochgeladene Ionen zu erhalten, was mit Elektrospray vergleichbar ist. Außerdem wird keine hohe Spannung direkt an die wässrige Lösung angelegt. In dieser Arbeit werden die Instrumentierung, Charakterisierung und wichtigsten Resultate des AP-DIVE-MS mit kontinuierlicher Probenzufuhr präsentiert und im Detail diskutiert. Darüber hinaus wird der mögliche Aufladungsmechanismus von AP-DIVE-MS durch Vergleich mit den verschiedenen existierenden Modellen diskutiert, sowie mögliche Aufladungsprozesse vorgeschlagen.

Das zweite Online-System ist das AP-DIVE-MS kombiniert mit einem Labor-auf-einem-Chip ('lab-on-a-chip', LOC) Interface, auf dem Pikoliter-Lösungen in einem Behälter von 300 nm Tiefe and 100 μm Durchmesser lokalisiert wurden. Die lokalisierte, wässrige Pikoliter-Probe wurde anschließend von der Rückseite her abladiert durch PIRL, der auf das Zentrum des Behälters und die Einlassöffnung des Massenspektrometers justiert wurde. Aufgrund des Gradienten der Oberflächenrauheit und eines instabilen Kontaktwinkels wurde eine 'dynamische Benetzung' auf dem Pikoliter-Chip erreicht, indem ein Tropfen der wässrigen Probe über die Chip-Arrays gezogen wurde. Außerdem wurde der Pikoliter-Chip automatisch ausgerichtet und gescannt unter Verwendung eines Bezugspunkt-Algorithmus, der in unserer Gruppe

entwickelt wurde. Der Verschiebetisch zur Halterung des Chips und die Kontrolleinheit des optischen Shutters von PIRL wurden synchronisiert, um die Empfindlichkeit des Systems zu erhöhen. Ionen-Signale von Einzel-Reihen- sowie Einzel-Behälter-Scans wurden erzielt, und die resultierenden Massenspektren werden präsentiert und diskutiert. Vorläufige Ergebnisse von Peptiden werden ebenfalls präsentiert, um die faszinierenden potentiellen Anwendungen des Chips für biomedizinische Analyse durch Massenspektrometrie aufzuzeigen. Es sei angemerkt, dass die Detektionslimits dieses ersten Injektionssystems unter Umgebungsatmosphäre die Empfindlichkeitslimits in den 10 Attomol-Bereich einstufen. Uns sind Verluste bei der Ionenerfassung bekannt, die durch ein direktes, internes Massenspektrometer-Vakuuminterface komplett vermieden werden können, um die Empfindlichkeitslimits um mehrere Größenordnungen zu verbessern. Diese Arbeit zeigt, dass Detektionslimits im Zeptomol-Bereich bis in den Einzel-Molekül-Bereich möglich sind, wie für die Analyse einzelner Zellen benötigt.

Structure of this thesis

Chapter 1

The working principle of the PIRL ablation operating under DIVE condition will be introduced and its advantages for biomedical sample desorption will be discussed. An overview of different AP-MS ionization techniques will be presented and compared.

Chapter 2

A short overview of the PIRL for biomedical and MS applications will be given. The interface designed to directly couple the PIRL to a Bruker iontrap with continuous flow aqueous sample delivery will be introduced in detail, including the beam delivery and shutter control system, the coupling interface, gas diverting extension and the electronic synchronization unit.

Chapter 3

The characterization of AP-DIVE-MS with continuous flow aqueous sample delivery will be demonstrated. Optimization of the sample flow rate, characterization of the total ion current (TIC), single pulse ablation response, and the sensitivity of the system will be described.

Chapter 4:

Results from the AP-DIVE-MS with continuous flow aqueous sample delivery will be presented. Sample preparation and mass spectra from small molecules, peptides and proteins will be presented. The charging mechanism of AP-DIVE-MS will be discussed and compared with existing models.

Chapter 5:

A new AP-DIVE lab-on-a-chip (LOC) MS interface is designed and will be introduced. Singe-row and single-well sampling of the megapixel arrays are performed. TIC responses and corresponding mass spectra, as well as the sensitivity of the

system will be presented. The preliminary results from small peptide and current challenges will be discussed.

1. Introduction

1.1 Fundamentals of DIVE

In the Chinese classic text Tao Te Ching, Lao Tzu says, 'the highest good is like water. Water gives life to the ten thousand things and does not strive.' Water is the fundamental substance of life. From the biological point of view, water not only accounts for over 70% of the total mass of cells, but also plays an important role on the three-dimensional structures of proteins and nuclear acids, and more crucially on the functionality of those molecules based on their structures and shapes [1]. In the mass spectrometric and analytical chemistry areas, water has also been widely utilized as one of the essential components for various methods. For example, water is used as solvent for liquid chromatography (LC), high performance LC (HPLC) and atmospheric pressure chemical ionization (APCI); water has been the medium in forming charged droplets and eventually highly charged ions in electro- spray ionization (ESI); water can be used as a matrix in both liquid and ice forms for matrix-assisted inlet ionization (MALDI), etc.

In this thesis, a novel picosecond infrared laser developed by our group, termed PIRL, is applied as a sample desorption source. The PIRL ablation plume produced from bulk liquids is directly coupled to an ion trap MS for analysis. No additional matrix or post ionization source is utilized to acquire highly charged ion signals. Additionally, no high voltage is applied directly to the bulk liquid sample. The working principle of PIRL ablation is based on the mechanism of Desorption by Impulsive

Vibrational Excitation and termed DIVE in abbreviation, which was experimentally and theoretically studied and discussed by K. Franjic [2]. The DIVE mechanism and its benefits for biomedical applications will be briefly introduced in this section.

Observing the atomically resolved structural dynamics of impulsive energy deposition induced phase transitions, the melting process of Al has been achieved by femtosecond electron diffraction. One important discovery is that homogeneous nucleation occurs under superheating conditions when an ultrafast femtosecond laser pulse is applied to the sample [3]. This ultrafast laser-driven phase transition mechanism sheds light on applying it to other condensed phase substances. For biomedical research, the phase transition of water is one of the most interesting topics as it is the key components for the composition and functionality of biological entities. Liquid water has a unique three-dimensional network of hydrogen bond structures where the bonds constantly form and break [4, 5]. The depletion of ν_0 state and stimulated emission from ν_1 state of OH stretching oscillator of liquid water has been observed between 3170 and 3400 cm^{-1} (2.92 – 3.15 μm), resulting in the strong absorption of optical energy in this spectral region. It is followed by subsequent vibrational relaxation with energy transferred between the oscillator and hydrogen bond network, which starts at $\sim$ 200 femtoseconds. The complete thermalization process takes place on a picosecond time scale, during which 1 g/cm^3 water density was maintained [6, 7].

Before utilizing PIRL under DIVE mechanism for MS purposes, it should be noted that employing laser pulses centered at 3 μm for desorption or desorption/ionization of tissue or other water–rich samples in both liquid and ice forms have been reported by several MS groups, such as IR-MALDI [8], IR matrix-assisted laser desorption electrospray ionization (IR-MALDESI) [9, 10], laser ablation electrospray ionization (LAESI) [11], etc. In all the current IR-laser methods mentioned above, the pulse duration is usually between few tens to few hundreds of nanoseconds. Laser desorption (vaporization) by nonresonant 800 nm femtosecond pulses with ESI post–ionization has also been studied under AP condition. Both hydrated and dehydrated samples

were vaporized by the ultrashort 70 fs laser pulse with a power intensity of 10^{13} W/cm^2 before thermal equilibrium was established and then post-ionized by ESI nebulizer [12, 13].

For laser desorption in the DIVE regime, two parameters of the laser pulses are crucially important. The first is that the wavelength must be within the 2.92 – 3.15 μm regime, and ideally centered at 2.94 μm. The second is that the pulse duration must be between ten to a few hundreds of picoseconds, which is unique compared to all other IR laser-based MS methods. First and foremost, selecting the wavelength near 2.94 μm guarantees the efficient optical energy pathway to the OH stretch band of liquid water and the subsequent ultrafast energy redistribution in the hydrogen bond network. Laser pulse energy rather than laser peak intensity accounts for the bleaching of transition between ν_0 and ν_1 vibrational levels. At room temperature, the vibrational excitation band centered at 3400 cm $^{-1}$ (2.94 μm) can absorb high laser intensity at the order of 10^{10} Wcm^{-2} with a relaxation time less than 3 ps [7]. Second, as mentioned above, the thermalization of vibrational relaxation of the OH stretch in liquid water is completed within one picosecond. The laser pulse duration for DIVE is designed to be longer than the thermalization of the vibrational excitation of the OH stretch mode. As a consequence, the very high laser fluence centered at 2.94 μm together with the ultrafast thermalization time make it possible to reach the superheating condition of liquid water accompanying intensive phase transitions. Third, the picosecond pulse duration helps to avoid multiphoton ionization or vibrational ladder climbing, which may damage the analyte molecules in water. Note that nonresonant femtosecond vaporization mentioned above reports the intact mass spectra of proteins. Only quasi-native mass spectrum of lysozyme is presented, whereas the rest are protein mixtures such as human blood and egg white, from which single intact protein mass spectra are difficult to differentiate [12]. Additionally, DIVE avoids heat transfer and shock wave generation due to the energy deposition time being shorter than the thermal and acoustic relaxation times of water. For a typical laser ablation event, the thermal relaxation time is usually of the order of several μs, while the acoustic relaxation is around 1 ns. By

confining the pulse duration from 10 to few hundred ps, the optical energy will be most efficiently coupled to the vibrational excitation of OH stretch mode of water. This results in the ultrafast superheating of water without energy leaking out of the excited volume by thermal or acoustic transients. And it is expected that intensive phase explosion will occur with mainly homogeneous nucleation inside the excited volume at the water/air interface.

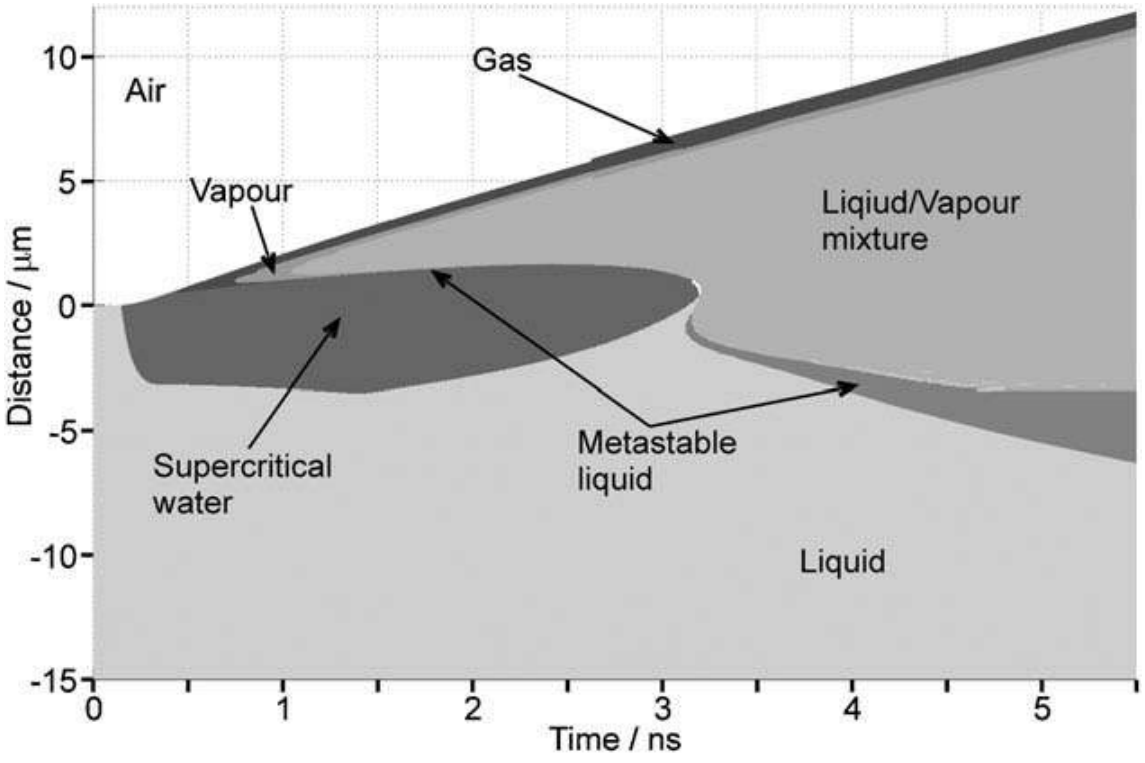

Figure 1.1: Theoretical simulation on temporal evolution of plume dynamics. Figure taken from [2].

Theoretical simulations performed by K. Franjic are demonstrated in Figure 1.1, in which the temporal evolution of plume dynamics of the excited volume is explored. From these one-dimensional simulations one can obtain the phase distributions at different times following PIRL ablation. For example, in the (0 – 1) ns regime,

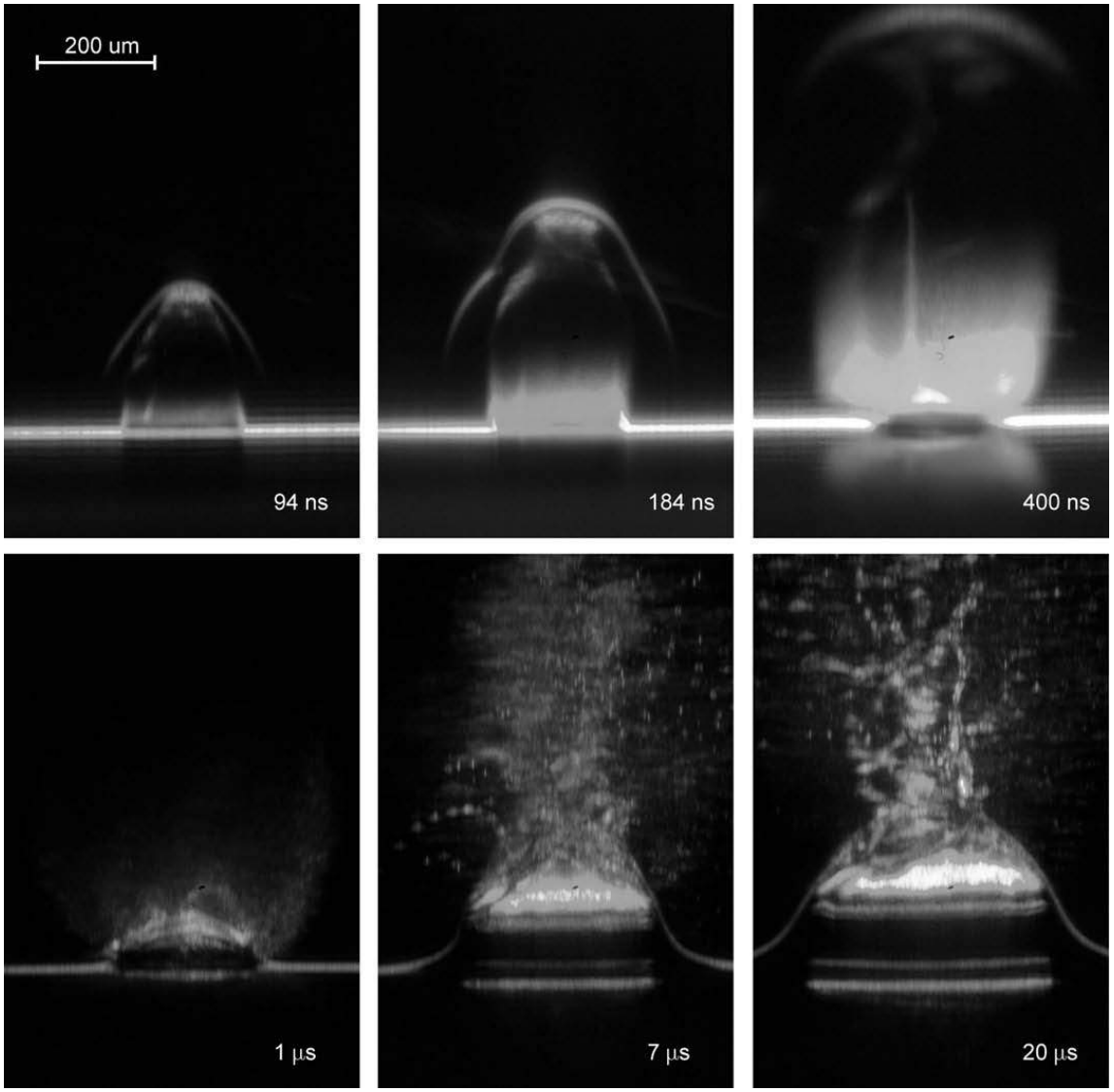

Figure 1.2: Dark field images of PIRL ablation plume from liquid water under AP condition. Figure taken from [2].

supercritical water is the most abundant substance in the excited plume. The front of the excited volume is turned into vapor and gas (depending on whether it is lower or higher than the critical temperature) by fast plume expansion and cooling at the interface. In the (1 – 3) ns regime, continuing expansion of the plume leads to the transfer from the supercritical state to a liquid/vapor mixture and gas at the front with a thin layer of metastable liquid between supercritical water and the mixture. After 3 ns, the expansion of the plume causes the pressure drop inside the volume and therefore a thick layer of metastable liquid is formed. The phase distributions of the plume with gas front followed by vapor layer and a big portion of liquid/vapor underneath remain unchanged during propagation [2].

Dark field images of the plume dynamics for longer time scales (0 – 20 μs) are presented in Figure 1.2. Due to the fast expansion of the plume, a shock wave front at the top can be easily discerned in the image. The plume is elongated in the longitudinal direction (i.e., vertical in Figure 1.2) due to the higher momentum in this direction compared to the transverse one. One interesting observation is the nearly transparent primary plume front within 1 μs, which implies that it is constituted mainly of gas and vapor, and is consistent with the simulation result in Figure 1.1. Another major observation is that a much more intensive secondary plume explosion occurs after 1 μs, which is termed 'recoil' and very common for numerous laser ablation techniques performed on liquids. It can be seen that the total volume of ablated material in the secondary plume is much larger than the primary one. In contrast to the primary plume, where a vast portion of the plume front is vapor and gas, the second plume mainly consists of liquid droplets with diverse diameters. Moreover, the density of the liquid/vapor mixture in the primary plume is much more uniform than in the secondary one, in which the droplet size varies and becomes more coarse with temporal evolution [2]. However, it should be noted that droplet formation can be an essential factor for the highly charged ion generation (similar as ESI) and might account for the charging mechanism of AP-DIVE-MS, which will be discussed in detail in the following chapters.

In summary, the PIRL developed by our group, which works under the principle of DIVE, is ideal for applications related to biomedical analysis. The unique picosecond pulse duration is longer than the thermalization of the vibrational excitation of OH stretch mode of water and shorter than the thermal and acoustic relaxation times of the liquid. In this way, the impulsive heat to drive phase transition under superheating condition occurs without the leaking of optical energy from the excited volume via shock wave generation or heat propagation. Consequently, analytes in the aqueous solution can be preserved intact and turned into gas phase with minimum damage of the structures for further study by MS.

1.2 Overview of AP and Vacuum Based-MS Techniques with Different Ion Sources

ESI and MALDI are two leading 'soft ionization' techniques used for analyzing biological samples with minimal damage and fragmentation of analytes. Based on theses two pioneering techniques, a considerable diversity of methods have been developed utilizing either the highly charged ions from ESI or the laser-based matrix desorption and ionization from MALDI in both AP and vacuum conditions or a combination of both. In addition, an acoustic method is utilized for sample desorption for several AP-MS techniques. Moreover, inlet ionization methods based on thermal desolvation processes play a role in AP MS techniques. In this section, an overview of different AP and vacuum based MS techniques, which produce similar highly-charged ions and/or soft laser desorption as AP-DIVE-MS, are discussed and compared under various categories.

1.2.1 ESI and ESI-based MS Techniques

The working principle of ESI, as illustrated in Figure 1.3, is as follows: a liquid sample is delivered via a fine metal capillary. A high voltage (usually few thousand kV) is applied between the metal capillary and the inlet of MS. Due to the electrical gradient, the conductive fluid at the tip of the capillary forms a Taylor cone,

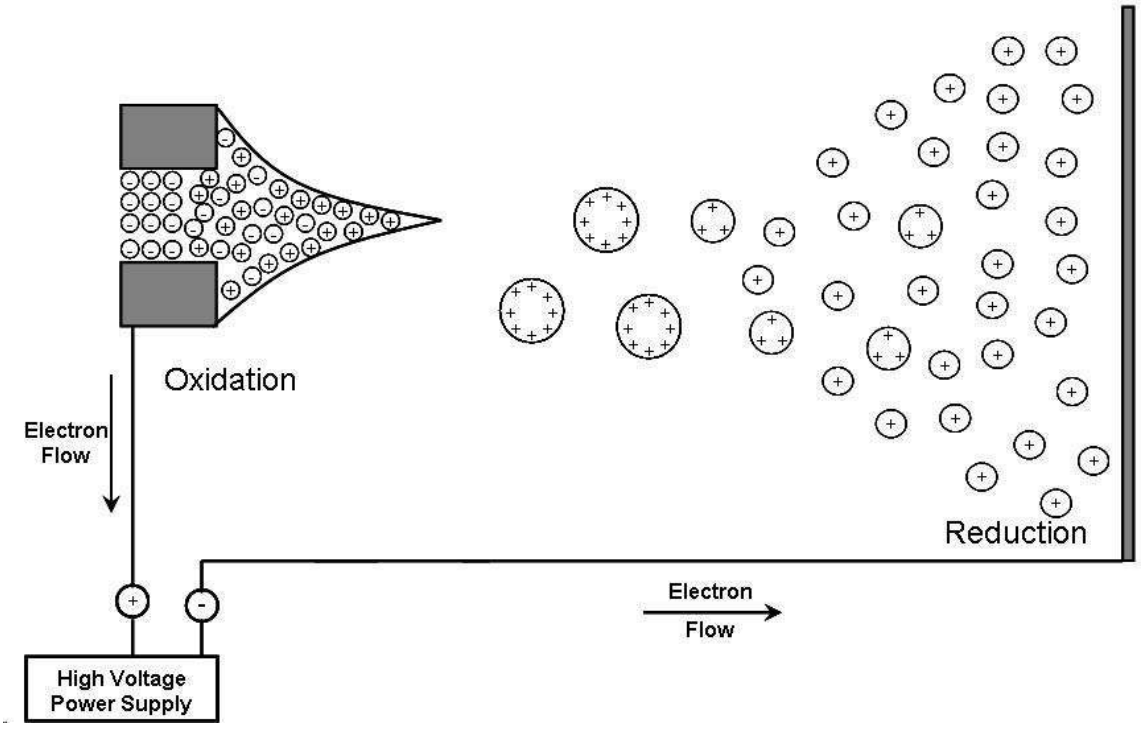

Figure 1.3: Schematic overview on how charged droplets are generated in ESI. Figure taken from [14].

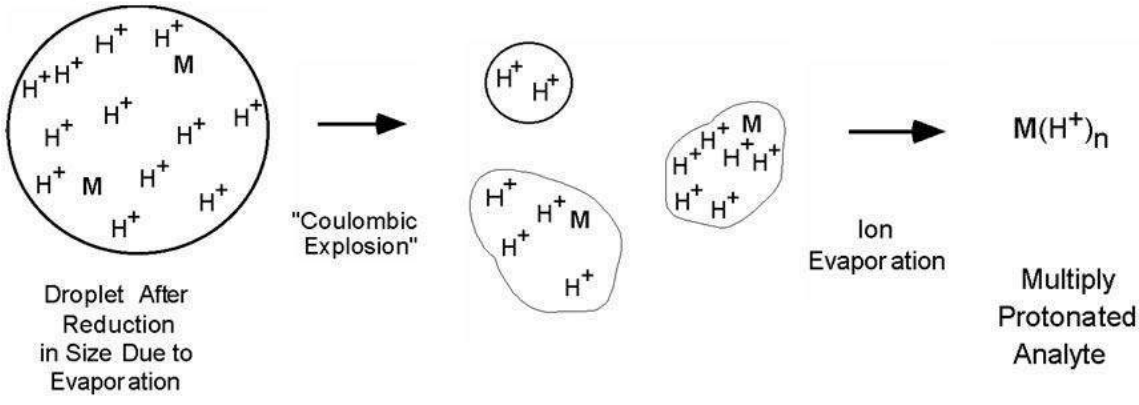

Figure 1.4: Schematic diagram illustrating the desolvation process and the possible ion formation mechanism in ESI. Figure taken from [14].

from which charged droplets are emitted. Subsequently, charged droplets migrate following the electrical gradient to the MS inlet. During the migration from Taylor cone to MS inlet, charged droplets experience an essential Coulomb fission process, in which highly charged gas state ions are eventually generated for further analysis in MS. The desolvation process, during which bigger droplets constantly shrink into smaller ones via Coulomb fission, is illustrated in Figure 1.4.

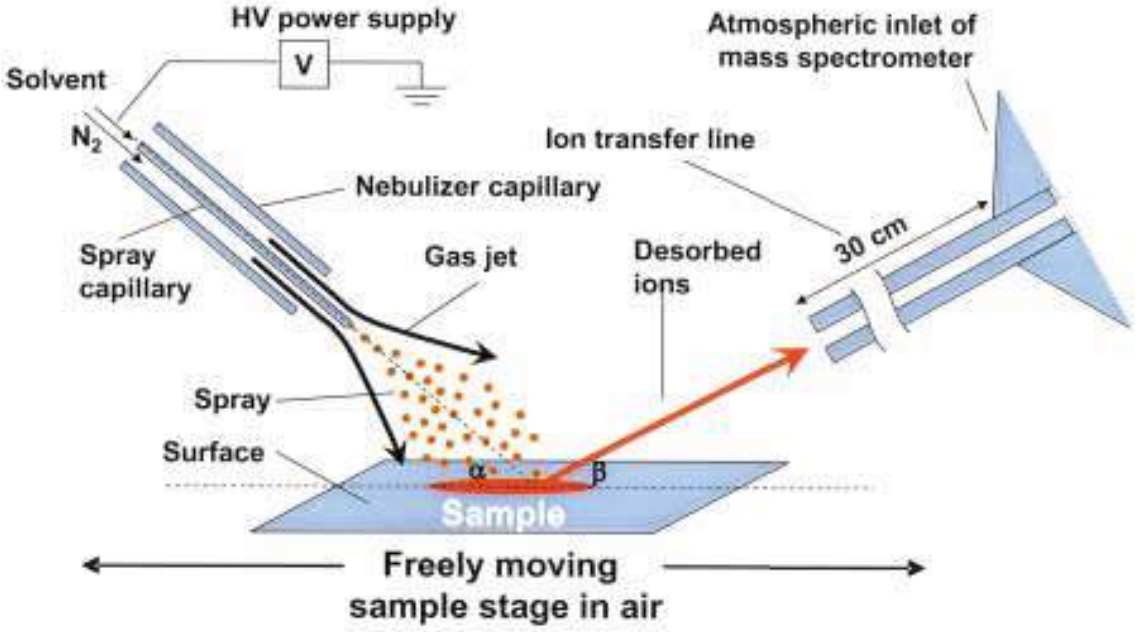

Figure 1.5: Schematic overview of DESI interface. Figure taken from [15]

The mechanism of multiply charged gaseous ion formation is still under discussion. Yet two prevailing models, the charged residue model (CRM) and the ion evaporation model (IEM), are usually regarded as the major models accounting for this phenomenon. In CRM, it is postulated that by fission process eventually some small droplets are formed, which contain only one analyte molecule inside the droplet with ionic charges on the surface. By evaporation of the solvent, the analyte molecule is charged by the ionic charges originally on the surface of the droplet, and thereby gaseous charged ions are generated [16]. In IEM, it is predicted that that when the

droplet size shrinks to a diameter less than 10 nm, ions can directly escape from the droplets [17]. Experimental evidence shows that CRM may account for the gas phase ion formation of small molecules, while IEM seems to be more reasonable for macromolecules such as proteins [18, 19].

Based on the ESI method, where highly charged ions are generated using a nebulizer, one application is to utilize the ESI nebulizer combined with analytes desorbed by other sources, such as a laser pulse or surface acoustic wave, so that each process can be optimized individually. Desorption by electrospray ionization (DESI) is one of such examples that can be widely used for fast, *in vivo* measurements at AP with minimum sample preparation required [15, 20]. Figure 1.5 shows the illustration of the DESI scheme. The ESI nebulizer is oriented under a certain angle directly to the sample surface. The highly charged droplets and ions generated from the nebulizer form a gas jet directly interacting with the sample surface, which is positioned on a free-moving sample stage. The desorbed analyte combined with charged droplets is then impelled into the inlet of MS. It experiences a similar desolvation process as in ESI and the gaseous ions will be generated ultimately with both single and multiply charged states. The DESI method can be applied to a very broad variety of sample types, such as nonpolar small molecules, and polar macromolecules (peptides and proteins). Another feature of DESI is that it can selectively choose the desorption area or compounds that is of interest, which allows the possibility of MS imaging. The limit of detection (LOD) of DESI has been reported to be 4 fmol and the spatial (lateral) resolution for DESI MS imaging is 200 – 400 μm.

Laser ablation electrospray ionization (LAESI) is another important MS analytical and imaging technique [21, 11, 22, 23]. It is the combination of IR laser (2.94 μm, 5 ns) desorption with post–ionization via the highly charged droplets and ions generated from ESI nebulizer in AP. LAESI also covers the analysis of a broad range of sample types, from small molecules, lipids to peptides and proteins. It has 4 orders of magnitude dynamic range (linear range) with LOD of 8 fmol, based on which quantitative MS is plausible. LAESI has been utilized to tissue and even cell

imaging. It achieves a lateral resolution of 100 μm and depth resolution of 40 μm, enabling three-dimensional profiling of tissue or even large cells. In addition, the laser typically involved in the LAESI interface is in the IR region centered at 2.94 μm. Optical energy is directly deposited to vibrational excite the OH stretch mode of water or ice, which is similar as PIRL but with longer pulse duration. Spectra of natively folded proteins have been obtained using LAESI illustrating the method as soft in nature.

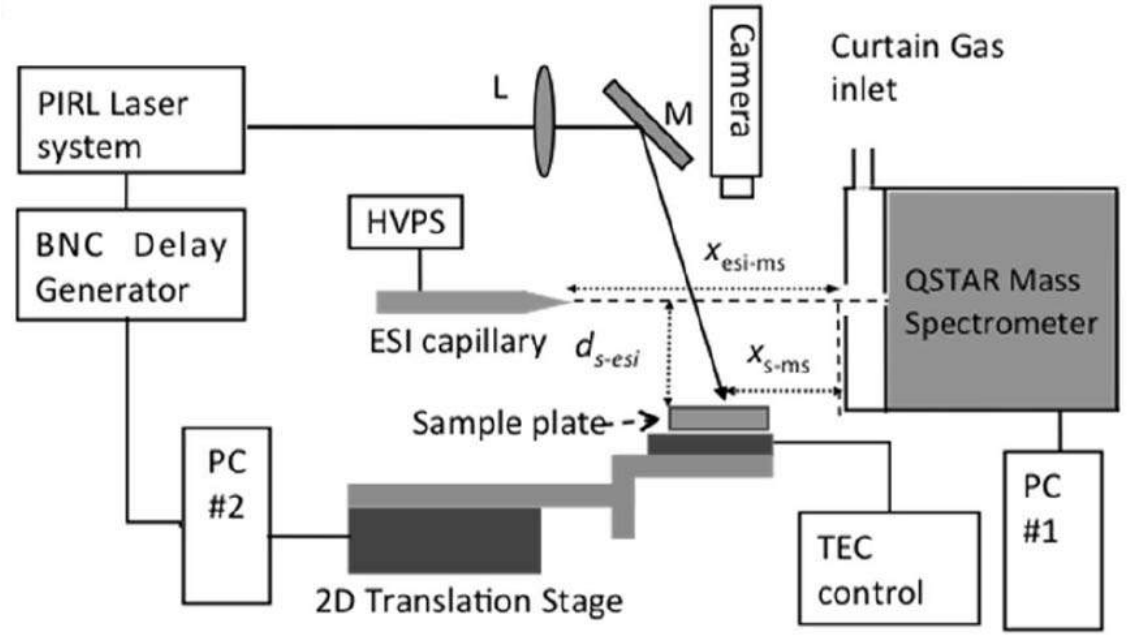

Figure 1.6: Illustration of PIR–LAESI setup. Figure copied from [24].

An almost identical interface based on the LAESI technique has been developed in our group and termed picosecond infrared laser ablation electrospray ionization (PIR-LAESI) [24]. It replaces the nanosecond IR laser with PIRL in the LAESI interface, as shown in Figure 1.6. Biosamples, such as proteins and phospholipids, are measured by the PIR-LAESI interface. It has been reported that the PIR-LAESI exhibited a LOD of 5 nM. In addition, spatial resolutions of 20 – 30 and 100 μm for

vertical and lateral resolutions were demonstrated respectively. Tissue imaging was performed on zebra plant (*Aphelandra squarrosa*) leaves by mapping the distribution of endogenous methoxykaempferol glucoronide as a marker. Furthermore, PIRL-LAESI was utilized to image the distribution of the biomarker gadoteridol, a contrast agent used for tumor cell imaging, in mouse kidney. It was demonstrated that PIRL-LAESI can be applied as a LAESI-based AP ion source for soft MS analysis on molecules and tissues. The technique has the potential to become an online analytical tool supplementing PIRL surgery as part of a molecular feedback system.

1.2.2 MALDI and MALDI-based MS Techniques

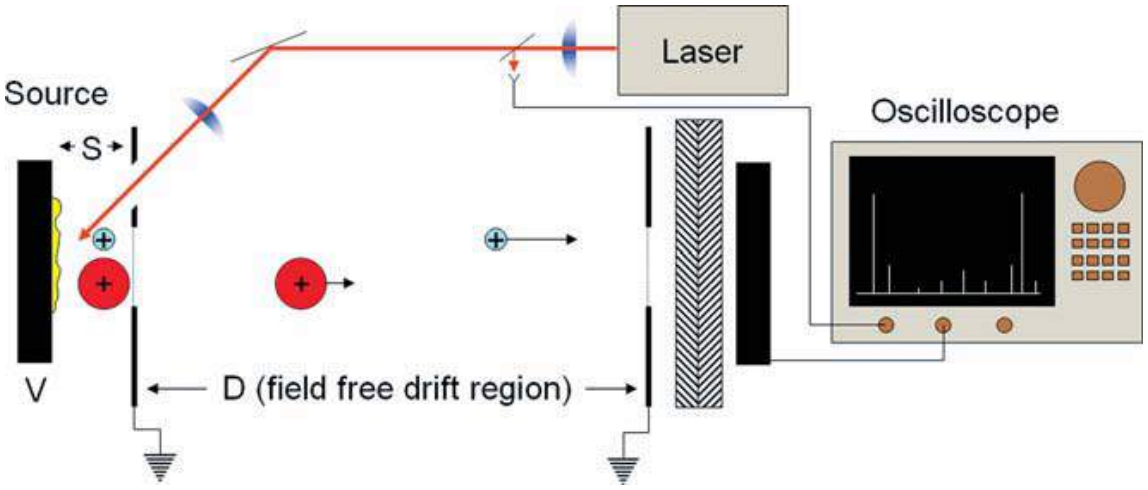

Figure 1.7: Schematic overview of MALDI instrumentation. Figure taken from [25].

MALDI is another highly utilized technique for ion production for MS analysis. As presented in Figure 1.7, a laser (typically UV or IR) pulse is focused onto a sample plate, on which analytes are combined with matrix (solid or liquid) and deposited. By laser desorption onto the matrix mixture containing analytes, the ions are brought into gas phase. During laser ablation and then possibly also inside the ablation plume, ionization of the analytes occurs. The gas phase ions are then

analyzed by the MS. MALDI has been reported to analyze biomolecules (peptides, proteins, DNA, lipid, etc.), polymers, and other macromolecules.

Similar to ESI, MALDI is regarded as a soft ionization technique for MS [26, 27, 28, 29]. The main reason is that the laser used for desorption and ionization does not directly interact with analytes. The matrix performs several functions in MALDI MS: 1. It absorbs laser energy and isolates and protects analytes from fragmentation and bond breaking by laser irradiation. 2. It releases the analyte when the plume enters the inlet of MS analyzer in vacuum. 3. It involves in the ionization of the analyte in the matrix and/or in the laser ablation plume.

One dramatic difference between MALDI and ESI is that the charging states in traditional MALDI are much lower than in ESI even with the same analyte and are matrix–dependent. This indicates that the charging mechanism of MALDI is different from ESI. Although the charging mechanism of MALDI is still under investigation, there is a common consensus that the matrix plays an important role in this process. In the charge transfer model, it is proposed that the matrix is primarily ionized by laser desorption and it then transfers the charge to the analytes [30]. Another model is the lucky survivor model, where the ions are originally from the analytes' intrinsic ion state and incorporated into the matrix. Laser ablation generates charged/uncharged clusters. Those charged clusters, which are not neutralized by their counter ions, are the survivors [31]. Not only the primary laser ablation, but also the secondary ion-molecule reactions possibly account for the ion formation in MALDI. It is postulated that charge and proton transfer reactions occur between ions and molecules in the laser ablation plume in UV MALDI [32].

It should be noted that IR-MALDI using nanosecond 2.94 μm laser pulses with water or ice as matrix has been reported by several groups [33, 34, 35, 36, 37]. For example, numerous proteins, including lysozyme, cytochrome c, and bovine serum albumin combined with ice matrix have been studied in IR-MALDI and the highest charging states of 4+, 1+, 2+ presented in the spectra, accordingly [33]. IR-MALDI using water as matrix has also been reported, where only the singly charged state

of angiotensin I is observed. In addition, water has been used as the natural matrix for IR-MALDI to study plant tissue (strawberry, grape and banana) and several molecules present in the tissue are identified from the mass spectra. Moreover, water has been used as native matrix and marker for the IR-MALDI imaging of strawberry tissue *in vivo* in the native state [37]. In short, consistent with MALDI mass spectra from other types of matrices, IR-MALDI utilizing water and ice matrices also suffers from low charging states. Nevertheless, as biological samples especially tissues and cells are usually water-rich, water can be applied as a native matrix for MS imaging.

1.2.3 Combinations of ESI and MALDI

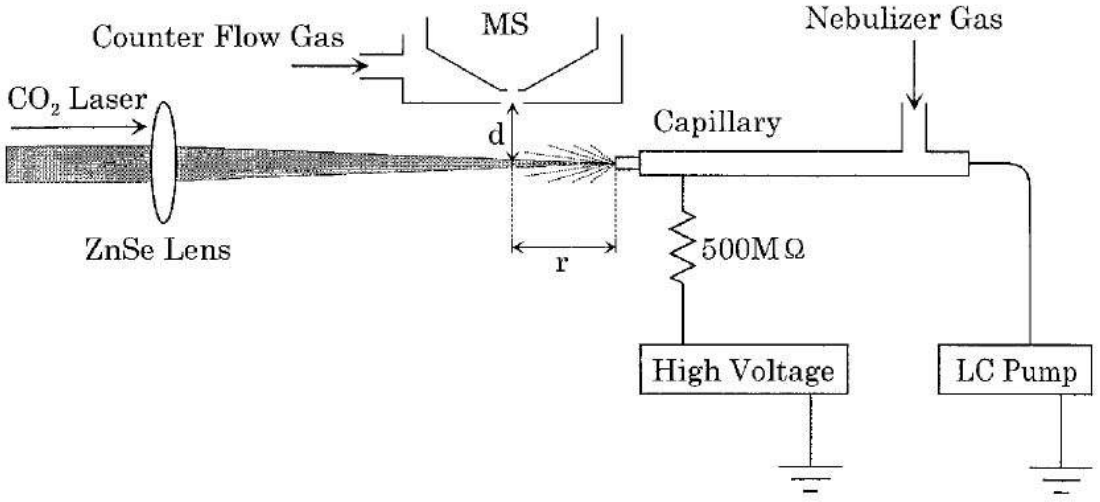

Figure 1.8: Illustrative representation of laser spray apparatus. Figure taken from [38].

Combining the strengths from both ESI (highly charged states) and MALDI (water matrix, laser desorption) has been a trend of AP-MS techniques. One example is the laser spray by K. Hiraoka, specified as an 'electric field-assisted matrix-assisted laser desorption/ionization' method [38, 39, 40, 41, 42]. As illustrated in Figure 1.8, the key component in laser spray is a nebulizer, which is almost identical to ESI nebulizer

yet with slightly bigger inner diameter. A CO_2 laser with 10.6 μm wavelength is focused into the center of a capillary, where aqueous sample is flowing through. In addition, nebulizer gas is used to assist in sample desolvation and a high voltage applied directly onto the sample solution and nebulizer. Due to the high energy density of the CO_2 laser, a high flow rate and therefore high sample consumption are required for laser spray. Depending on the laser power, both highly charged and native protein spectra are obtained. The authors ascribed the charging mechanism of laser spray to the charged residue model and the ion evaporation model, similar as ESI [39]. Laser spray is regarded as a field-induced MALDI technique by the definition given the authors [40].

Unlike laser spray, which is a one-step ionization process, infrared matrix-assisted laser desorption electrospray ionization (IR-MALDESI) utilizes laser desorption on MALDI matrix (usually water or ice) with ESI postionization [9, 10]. IR-MALDESI overcomes the low charging state of MALDI by combing the soft IR absorption plume with the highly charged droplets from ESI. IR-MALDESI using ice as matrix has been applied to MS imaging of tissue sections with thickness of 50 μm. Leaf sample is positioned on a peltier cooling stage with a layer of ice deposited onto the sample surface as matrix. It was shown that comparing to the same tissue without ice as matrix, the ion signal from the one with ice matrix is significantly enhanced [9]. IR-MALDESI can directly analyze an aqueous sample solution by simply positioning a vertical capillary with solution delivery in front of the inlet of MS. The IR ablation plume is post-ionized by charged droplets from nano-ESI nebulizer, which is positioned horizontally centered with the inlet of MS. The combined plume is then desolvated and further analyzed by MS [10]. Note that AP-DIVE-MS with capillary sample delivery, which will be introduced in the following chapters, shares similarities to the interface. The major difference is that AP-DIVE-MS does not require any secondary or post-ionization source. By the intrinsic ion state of molecules in water or in some cases, in acetic solution, PIRL ablation is sufficient to generate ions, either through directed desolvation or by producing charged recoil droplets, which will experience a similar desolvation process as in ESI. Therefore highly charged spectra

from sample solutions can be obtained using AP-DIVE-MS.

1.2.4 Acoustic and Sonic MS techniques

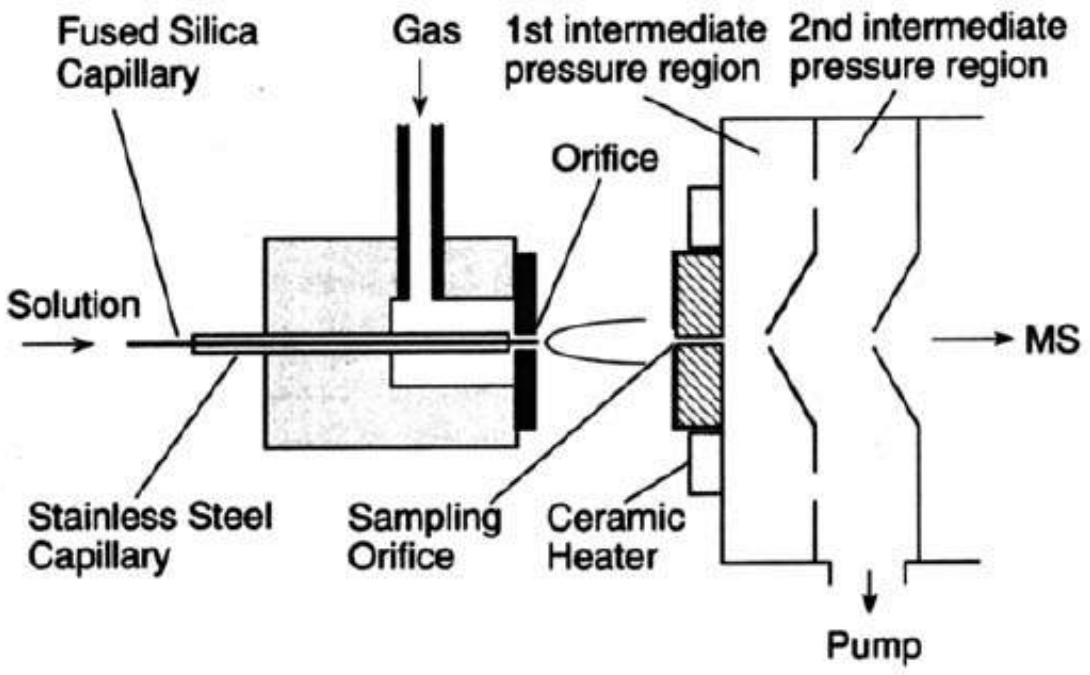

Figure 1.9: Illustration of sonic spray interface. Figure taken from [43].

Acoustic waves have been implemented in order to facilitate the gas phase ion generation from volatile or non-volatile aqueous samples for MS analysis at AP. Surface acoustic wave nebulization (SAWN) is one of such examples, which uses a $LiNbO_3$ interdigitated piezoelectric transducer (IDT) was introduced in [44, 45, 46]. By applying radio frequency oscillations on the IDT, the SAW propagates onto the surface of the sample chip, on which a droplet of sample solution is deposited. Energy from SAW is then transferred to the aqueous droplet and nebulization occurs. The study shows that the internal energy of SAWN is smaller than ESI and therefore it is considered as a 'softer' ionization source. In addition, highly charged ions are generated

in SAWN. Moreover, not only small molecules, peptides and proteins can be analyzed by SAWN, but also lipids, which can easily form aggregates and thereby clog in ESI capillary.

Sonic spray ionization (SSI) is a different MS ionization technique, in which the ion intensity depends on the Mach number of the gas flow rate [47, 43, 48, 49]. Figure 1.9 presents the schematic overview of the SSI setup. A fused silica capillary is inserted into a stainless steel capillary for sample delivery, which is positioned coaxially to the inlet of the MS. A solution containing water and methanol (50:50 v/v) is delivered via the fused silica capillary and sprayed by nitrogen gas flow with different Mach number at AP. Gas phase ions and charged droplets are transferred into the heated inlet of the MS for further analysis. In the first few publications of sonic spray, no high voltage was directly applied to the stainless steel capillary [47, 43]. Later a modification was made so that the solution first passed through a metal tube which connected to the fused silica capillary by a stainless steel joint. A high voltage is applied between the stainless steel joint and the source housing. An enhancement of the ion signal was observed when the voltage was increased up to 1.2 kV [48, 49].

An alternative design to sonic spray was reported from another group [50, 51], which was then modified by applying high voltage (up to 4 kV) directly onto the solution before spraying, and termed electrosonic spray ionization (ESSI) [51]. In this new interface, a Swagelok® T-element was used with two ends coaxially to the MS inlet for sample delivery and one end connected to Nitrogen gas for spraying. In addition, an obstructive SSI interface was designed, in which an obstructive metal tube was positioned between the ESI probe with highest operation sheath gas flow and MS inlet and on the path of spraying. It was demonstrated that the polarity of the obstruction helps to produce more selective or inclusive ions and enhance ion abundance and sensitivity [52]. Furthermore, nano-SSI is implemented using the similar interface as in Figure 1.9 in the modified version with high voltage on the solution. The gas flow rate with highest ion signal is found at Mach 1, which is identical to the observation in SSI. Similar results on the highly charged states and ion intensities of

proteins are obtained in nano-SSI, which are comparable to the ones from nano-ESI [53].

The ion formation and charging mechanism for SSI and subsequent techniques are discussed in several publications [47, 43, 50, 53, 54]. The charging mechanism of SSI needs to be carefully checked, especially considering publications without high voltage directly applied to the sample, as it might possibly account for the one for AP-DIVE-MS. Highly charged states as well as native protein mass spectra are obtained from SSI, which is comparable to ESI or nano-ESI. 'Friction electrification', 'electrical double layer', and 'statistical charging' are the most prevailing charging mechanism of SSI; while models, which usually explain ESI process, such as 'charged residue' and 'ion evaporation', have also been carefully examined for SSI. Although similar as ESI and MALDI that the charging mechanism is still under investigation, it is obvious that charged droplets are formed in SSI which play an important role in the gaseous ion formation. The charging models mentioned above will be discussed in detail in the following chapters.

1.2.5 Thermospray and Inlet Ionization

Thermospray and inlet ionization are two AP-MS ionization techniques that require a heated capillary tube to generate gas phase ions. Thermospray was first reported in the 1980s, in which a thermal vaporizer is implemented to the MS inlet [56, 57]. By monitoring the temperature of a thermalcouple that surrounds the capillary tube (temperature between 100 – 300 °C and flow rate dependent), a superheated mist of fine droplets with supersonic speed is produced from the vaporizer. The vaporizer and the MS inlet are designed to be orthogonal, so that the additional vapor can be pumped out of the system. Meanwhile, ion optics facilitates the gaseous ions to be transferred into the MS inlet. A differential mobility particle size analyzer (DMPS) has been used to study the droplet size distribution between ESI and thermospray. Compared to ESI, which generates nearly uniformly sized charged droplets, ther-

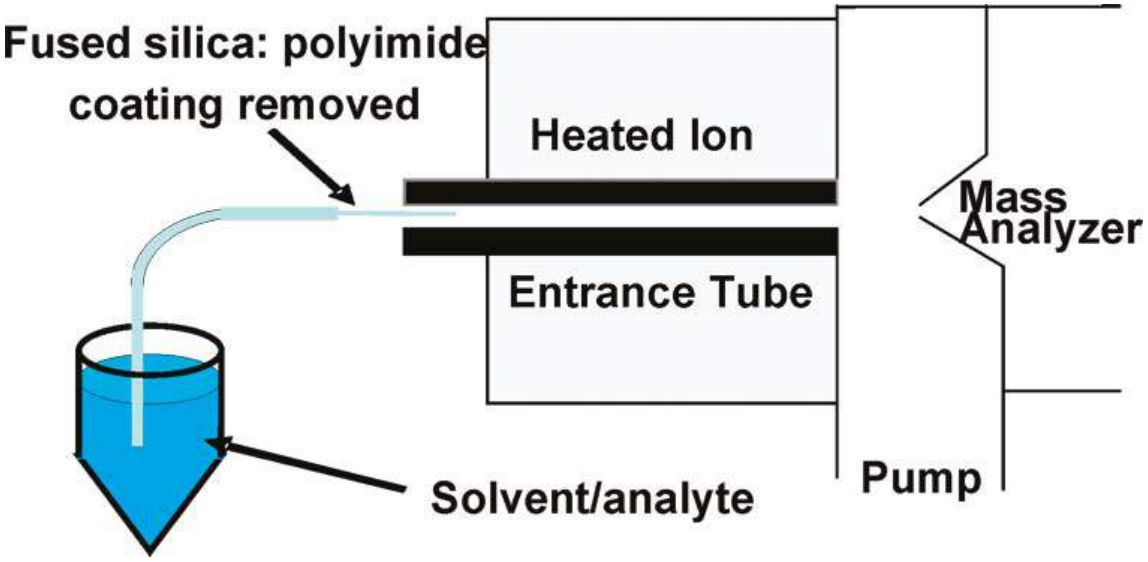

Figure 1.10: Illustrative representation of solvant assisted inlet ionization (SAII) interface. Figure taken from [60].

mospray has a more even distribution of droplet size and in total a much higher number of droplets. The charging mechanism of thermospray was discussed in detail [58, 59], in which statistical charging and ion evaporation models are regarded as the dominating models for thermospray.

Inlet ionization is a MS ionization technique that does not require high voltage, laser irradiance, or a matrix [60, 61, 62]. Figure 1.10 illustrates the interface of solvent assisted inlet ionization (SAII) setup. Sample solutions in water, methanol, or water/organic solvents50 mixture are directly transferred into a heated ion entrance tube via a fused silica capillary. Due to the pressure difference between the entrance tube and mass analyzer, sample solutions are able to be pumped into the MS analyzer. And multiply charged ions are generated in the heated inlet transfer capillary where the AP region and vacuum MS analyzer chamber are separated. As the silica capillary directly facilitated pumping the sample solutions into the vacuum chamber of the MS, there is almost no sample loss in AP, resulting in a high sensitivity of the system in the low amol regime. Samples including small molecules, peptides and proteins are analyzed by SAII. And the ion intensity for different charging states of

peptide and its dependence on temperature (50 – 500 °C) were studied and compared to the ones from ESI, laser spray, and sonic spray. Clear difference in trend lines are demonstrated among these four AP ionization techniques, though the same sample is applied. This indicated different charging mechanism, or the initial variations of charged droplet size and number distributions from different sources.

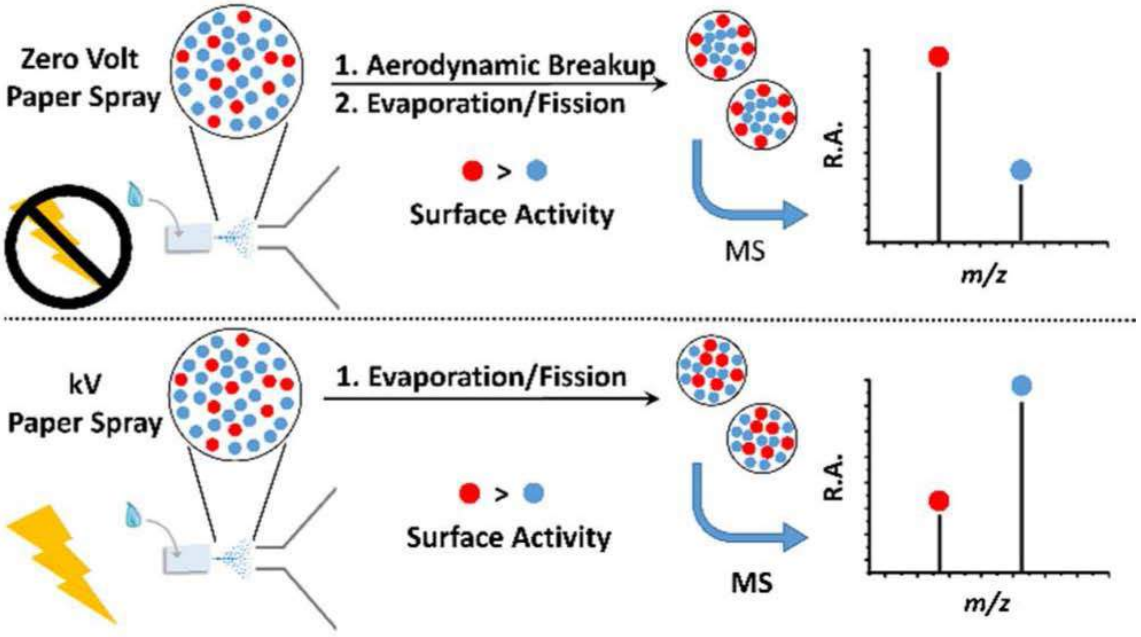

Figure 1.11: Schematic comparison between zero-volt paper spray and normal paper spray. Figure taken from [63].

Another variation of inlet ionization is the zero-volt paper spray (PS), which is shown in Figure 1.11 [63]. A paper substrate is positioned onto a glass capillary and coaxial to the MS inlet with a distance of 0.3-0.5 mm. An aqueous sample is loaded onto the paper and one waits until it is dried. Then the solvent is applied to rehydrate the paper substrate and the paper spray occurs. For zero-volt PS, no high voltage is applied to the paper, which is different from the normal paper spray technique. By comparing the relative intensities among different molecules, which

exhibit various surface activities, in a sample mixture between zero-volt PS and high-voltage PS, a charging scheme for zero-volt PS is developed. In the proposed charging mechanism, the primary droplets with diameter of $\sim$ 2 mm are generated from the paper substrate with the help of mobile phase solvents. Afterward, the primary droplets experience aerodynamic breakup based on statistical charging. The droplets continue shrinking until the diameter reached 1 – 4 μm. During this process, when the charge density at the surface of the droplets satisfies the Rayleigh limit, Coulomb fission occurs to further shrink the size of the charged droplets. Coulomb fission repeats until the droplet diameter $\leq$ 10 nm, when the gaseous ions are generated via direct ion evaporation.

1.3 Summary

To summarize this chapter, the fundamentals of DIVE are briefly introduced and its advantages for biomedical analysis and various other MS applications are discussed. In addition, an overview of a number of relevant AP-MS techniques, which are similar to AP-DIVE-MS in either the interface or the mass spectra generated, are introduced and the possible charging models are reviewed. ESI and ESI-based techniques usually exhibit highly charged states of the molecules, but employing a nebulizer in the interface limits the precision and spatial resolution of the system. MALDI and MALDI-based techniques inherit the precise sample targeting by applying laser desorption/ionization, yet the relatively low charging states of ions generated by these techniques restrict them from studying high molecular weight samples such as proteins or protein complexes. The hybrid techniques, which combine the advantages of highly charged ions from ESI and laser desorption from MALDI, such as laser spray and IR-MALDESI, have already broadened the scope of MS analysis. However, a high sample consumption rate or complexity of the system by adding a post-ionization device are currently major challenges of those techniques. Acoustic and sonic based techniques are alternatives to obtain highly charged ions, some of which are not applying a high voltage directly onto the analytes. This is similar to

thermospray and inlet ionization, where samples are delivered directly into heated MS inlets, due to the pressure drop from entrance to analyzer. For both techniques, highly charged ions are generated mainly from the desolvation of charged droplets. However, the sample phase of these two techniques are limited to aqueous ones, where biological tissues cannot be analyzed directly.

For AP-DIVE-MS, it is a laser-based soft MS technique without sample fragments. It exhibits the same ability to generate highly charged ions as ESI and ESI-based techniques, and it utilizes water/ice as matrices and laser desorption as MALDI and MALDI-based techniques. In addition, it shares similar softness and charging states as hybrid techniques with much lower sample consumption and without post-ionization devices. Moreover, for the simplicity of the system and highly charged mass spectra generation, AP-DIVE-MS is close to acoustic and sonic techniques, as well as thermospray and inlet ionization. Yet high precision of sample selection is achieved in AP-DIVE-MS by laser desorption. In the following chapters, various features of AP-DIVE-MS, including instrumentation, characterization, results, charging mechanism, and lab-on-a-chip (LOC) applications will be demonstrated and discussed in detail.

2. AP-DIVE-MS Interface with Continuous Flow Aqueous Sample Delivery

Contributions from co-workers to Chapter 2: Wesley D. Robertson modified and developed the MS coupling interface with help from Djordje Gitaric. Cornelius Louwrens Pieterse programmed the shutter control interface in Labview. Erik Frieling and Wesley D. Robertson designed the gas diverting inlet extension. Wesley D. Robertson developed and implemented the synchronization circuit.

2.1 Picosecond Infrared Laser (PIRL)

2.1.1 Overview of PIRL Performance for Medical and MS Applications

As introduced in detail in Chapter 1, PIRL has been carefully designed with a pulse duration in the picosecond regime and wavelength centered at 3 μm, which makes it a unique and powerful tool of sample desorption for the following reasons:

1. The wavelength of 3 μm, more precisely 2.94 μm, corresponds to the OH stretch vibration mode of water at 3400 cm^{-1}. It is the optimum wavelength to efficiently drive water-rich samples from the condensed phase into the gas phase without damage or modification of the analytes or surrounding regions. The energy is deposited

into the OH vibrational mode of water and further redistribution in the H-bond network on an ultrafast time scale [6, 64, 65, 66, 67].

2. The pulse duration in the picosecond regime (10 – 100ps) is carefully chosen due to its advantages over femtosecond or nanosecond counterparts for biological applications under the mechanism of DIVE. In the DIVE regime, on the one hand, the pulse duration of the laser is equal to or longer than the thermalization time of individual vibrational excitation, of which typical value at room temperature is within 1 ps. Consequently, creating highly excited molecular states, such as resulting from multiphoton ionization or vibrational ladder climbing, can be highly avoided by keeping the peak power low enough. On the other hand, the pulse duration is shorter than the thermal or accoustic relaxation times of the excited volume, which are usually on the order of μs and ns, respectively. Therefore the laser energy is efficiently confined in the excited volume driving the phase transition without the leakage of energy by thermal or acoustic transients [2].

3. In medical and MS applications, points 1 and 2 above would result in impulsive phase transition of the PIRL ablation site on tissue or cells without damages caused by shock wave generation. Also, since the heat effect is minimized due to the energy pathway of water, burning and scar tissue formation can also be optimally avoided by applying PIRL. Therefore it is expected that PIRL should be a good candidate for sample desorption and to be used as a cold laser scalpel.

Several papers from Prof. R.J. Dwayne Miller's and collaborative groups have been published on the applications of PIRL to medical and MS purposes. Those publications not only demonstrate the performance of PIRL as a new generation of laser scalpel, but also show the considerable potential of using PIRL as a soft laser desorption source for MS applications. In the following, a short review on the current status of PIRL for biomedical applications is presented.

2.1.1.1 Applications for Medical Purposes

Amini-Nik et al. first reported using PIRL as a novel laser scalpel in a study of wound healing of CD1 mice. Quantitative study of wound healing was made by comparing the scar width created by PIRL and conventional surgical laser (Er: YAG) as well as mechanical scalpel 2 weeks after the wounds were created. The study showed that the scar width formed by wounds from PIRL incision is half the size as compared to Er:YAG and scalpel counterparts [68]. Petersen et al. further study wound healing of rat skin from the proliferation phase to the remodelling phase by analyzing the macroscopic and histological process. The results of wound healing after 3 weeks from PIRL was compared to an electrosurgical device as well as a conventional scalpel. PIRL-incision showed much less visible scar formation among these three different methods. The scar areas of electrosurgical device and scalpel were calculated as 3.7 and 1.5 times larger relative to the value of PIRL, respectively [69].

Böttcher et al. applied PIRL for the incision of *ex vivo* soft laryngeal tissue and analysed the cutting edges and damage zones of the vocal fold by PIRL and other conventional surgical lasers. In contrast to the incisions by CO_2 and Nd:YAG lasers, PIRL exhibits increased cutting precision and significantly reduced lateral thermal damage zones [70, 71]. Hess et al. quantitatively compared the damage zones of cadaver human vocal folds after cutting by PIRL to the ones by scalpel or CO_2 laser. They further confirm that the damage zone by PIRL incision is much smaller, and almost free of coagulation, carbonization or other tissue damage around the cutting sites [72].

Jowett et al. studied the heat generation on porcine skin during PIRL ablation and compared it to the results from Er:YAG laser. It has been shown that both mean and maximum peak rise in skin surface temperature for PIRL are around 9 times lower than for Er:YAG laser[73]. They also applied PIRL on cutting hard material such as bone ablation. The results shows that due to the thermal and stress confinement of the DIVE mechanism, peak rise in surface temperature of chicken

humeral cortex is negligible and the cortical microstructure is preserved without the observation of microfractures under environmental scanning electron microscopy and light microscopy [74].

Linke et al. characterized PIRL cutting on porcine corneas by measuring the ablation depth and temperatures under different ablation times. It was the first report demonstrating PIRL as an efficient tool for applanation-free, contact-free deep cutting on healthy postmortem cornea and ideal for water enriched corneal transplant surgery [75].

In addition to the studies on PIRL incision of different biomaterials and tissues, Ren et al. analyzed the biological entities inside a PIRL ablation plume *in vivo*. It was illustrated that nanoscale single protein molecules (ferritin, rGFP), cells (S. cerevisiae) and viruses (Tobacco mosaic virus) in the PIRL ablation plume kept intact both structurally and functionally compared to its corresponding controls. The results demonstrate the potential of PIRL as a soft and powerful tool of sample desorption towards cellular level bioanalysis [76].

2.1.1.2 Applications for MS Analysis

Kwiatkowski et al. first applied PIRL desorption on top-down proteomics MS analysis [77]. It was demonstrated that PIRL exaction resulted in a coverage of broad range of proteins from a few kDa to several MDa. Mass spectra of protein extractions from PIRL were measured offline amd compared with the unablated controls from conventional MALDI-MS and LC-ESI-MS. The results showed that the proteins were intact both chemically (no change of chemical composition) and functionally (maintenance of enzymatic activities). They also used the LC-MS method to study the protein species *in vivo* from homogenization of tissues by PIRL and compared it to the one from conventional mechanical homogenization. A higher number of intact protein species and a higher yield of the amount of proteins were found by PIRL compared to conventional mechanical homogenization method [78].

Zou et al. developed the first interface for direct coupling PIRL to a MS inlet un-

der atmospheric condition and termed the method picosecond infrared laser ablation electrospray ionization (PIR-LAESI). The method used an ESI nebulizer to combine PIRL ablation plume for post-ionization with a home-constructed imaging system with a vertical resolution of 20-30 μm and lateral resolution of around 100 μm. The sensitivity of the system was measured to be 25 fmol of Rhodamine in agar and a limit of detection of $\sim$ 100 nM for reserpine and $\geq$ 5nM for verapamil aqueous solutions [24]. Moreover, they performed molecular dynamics simulations of the PIRL ablation process by using a model peptide (lysozyme)/counterion system in aqueous solution under typical experimental conditions in TOF-MS. The results showed that over 90% of the water molecules were stripped off from lysozyme within 1 ns after PIRL ablation without fragmentation. In addition, the applied field had almost no influence on the laser ablation and desorption process; yet there was sign even at very early time (limits of the MD simulation) that applied fields can be used to separate native charged proteins from their counterions, eliminating any post -ionization requirements and allowing the studying of mixtures without purification. This work demonstrated the potential of PIRL as a desorption source for high sensitivity quantitative MS [79].

2.1.2 Specifications of PIRL for AP-DIVE-MS Experiments

The specifications of the laser which is used for beam delivery to the MS system are shown in Table 2.1.

Table 2.1: Specifications of PIRL for the MS experiment

Producer	Model	Wavelength	Pulse Duration	Repetition Rate
Attodyne Inc., Canada	PIRL-APLQ-3000	3.1 $\pm$ 0.1 μm	7 ps	1 kHz

The beam delivery system for all the experiments involved in this thesis is depicted in

Figure 2.1. It should be noted that the beam delivery system was further simplified without applying the telescope and by placing the shutter shown in Figure 2.1 in the beam path of the pump laser of PIRL for portions of the results of the capillary experiments, which will be specified in the corresponding discussion later. This is after the replacement of new nonlinear crystals and realignment of PIRL (not shown in Figure 2.1). No matter if it was the original or new version of beam delivery used in the experiments, after focusing the PIRL beam by a 25 mm lens to the sample, the transverse beam diameter in the focus was approximately 140 μm measured by a WinCamD-FIR2-16-HRR camera. In the sample plane, the pulse energy was measured to be 40-50 μJ per pulse. The focusing lens was mounted on a translation stage in order to optimize the ion signal intensity and stability.

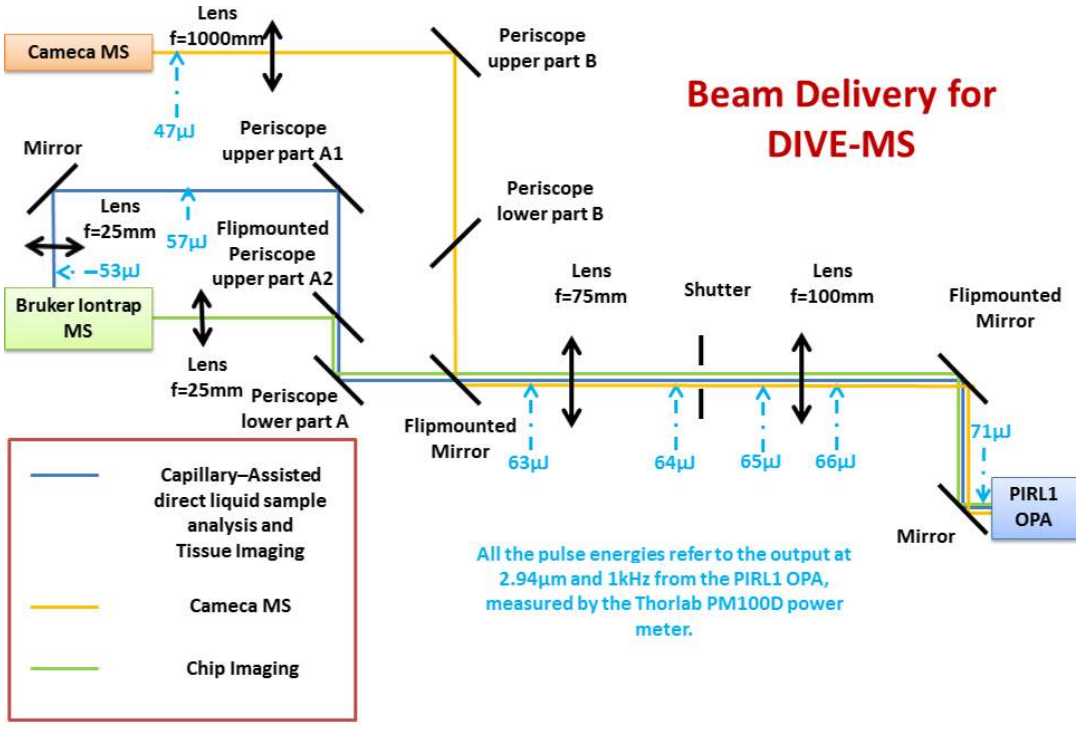

Figure 2.1: Scheme of beam delivery of PIRL to MS experiments.

2.2 Home-designed Interface for a Bruker Ion Trap

The DIVE-MS system was constructed by modifying a commercial Bruker ion trap mass spectrometer (Esquire 3000) with a home designed interface, which was adapted to the PIRL ablation of the sample for optimized ion signal intensity and stability. More specific, it was constructed by removing the spray chamber (including nebulizer assembly), rearranging the interlock circuit, redesigning the end plate to shorten the distance between sample ablation site and inlet of MS, and changing the capillary mounting assembly. The details of each modification are discussed in the following subsections.

2.2.1 Replacement of Spray Chamber to Coupling Interface for PIRL Ablation Plume Collection

The original spray chamber, which consists of nebulizer assembly and end plate is presented in Figure 2.2 (”Before” in the upper left panel). The geometry of the chamber was not yet adapted to the PIRL coupled interface. Therefore a new end plate was designed based on the dimensions of slots, holes and connectors of the original plate with a flat end surface shown in Figure 2.2 (”After” in the upper right panel). After reconnecting all the connectors, electricity, and MS components, the modified interface is illustrated in Figure 2.2 (”Installed” at the bottom). The custom-designed interface facilitates optimization of the ion collection efficiency by optimizing the access of PIRL ablation plume, sample delivery to the inlet of the MS.

2.2.2 Gas Diverting Inlet Extension

One challenge for the new interface was that the original pathway of the heating gas for the glass capillary was conducted out of the MS inlet, which was used to shrink the ESI droplets in order to acquire gas phase molecules. However, this would negatively affect efficient ion collection from PIRL ablation as it prevents the access

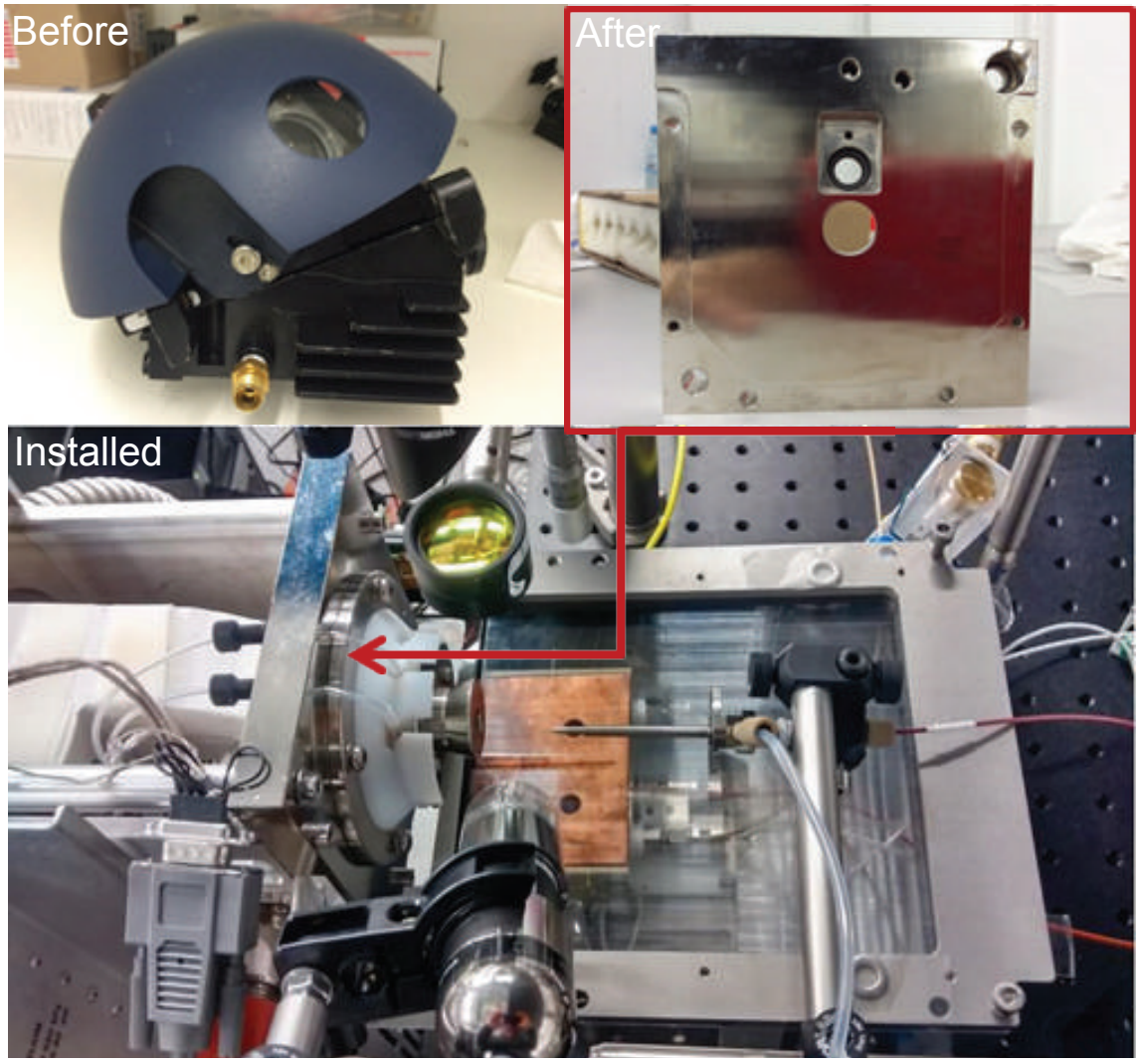

Figure 2.2: Inlet of the Bruker iontrap MS before (upper left), and after (upper right) modification and its finally installed configuration (bottom)

Figure 2.3: (a) cross-section structure and (b) components of gas diverting inlet extension: 1. metal capillary with adapter, 2. tungsten spring, 3. thread adapter, 4. macor spacers, 5. heating sleeve, 6. cap, and 7. macor plug.

of the ablation plume to the MS inlet. In order to increase the ion signal, a gas diverting inlet extension with flow rate of 10 l/min was designed and manufactured in such a way that the heating gas is diverted away before it can interact with the ablation plume. The heating of the transfer capillary is performed by the heated curtain gas in order to adequately control the heat without rapidly evaporating the sample. The design and detailed structure of the gas diverting inlet extension are presented in Figure 2.3. It should be noted that the relatively higher temperature and longer traveling path of the metal capillary could possibly induce the unfolding of proteins in the ablation plume. Therefore the original inlet with minimized gas flow rate of 0.5 l/min was also implemented for some native protein measurements. The temperature of the heating gas for both inlet ranges from 40 to 200 degree depending on sample variation. The temperature of the transfer capillary was measured using a thermocouple and noted in the text.

2.2.3 Geometry of AP-DIVE-MS Interface

A complete schematic representation of the AP-DIVE-MS interface is illustrated in Figure 2.4. The sample solution is injected into a syringe (Hamilton, 25 μl) and delivered by a syringe pump (KD Scientific) to a capillary transfer tubing (pre-cut natural PEEK, 1/16 inch outer diameter, and 0.030 inch inner diameter, TPK130, VICI). The capillary transfer tubing is positioned in front of the capillary extension or spray shield of the MS and mounted onto a two-axis translation stage for optimization of the position of the tubing relative to the inlet of the MS for sample ablation. The exit of the tubing was cleaved with flat end whose center is aligned 22 mm below the focal point of the PIRL. The PIRL is delivered by a 25 mm focal length e-coated Calcium Fluoride focal lens focusing downward toward the tubing. The position of the PIRL focal point could be optimized by adjusting the focal lens which was mounted on a translation stage. The optimum position of the PIRL focal point was located 12 mm away from the end surface of the collection entrance of the MS and 2 mm in the direction below the central axis of MS ion transfer capillary. A long working distance microscope (Dino-lite, AD7013MTL(R4)) was used to image

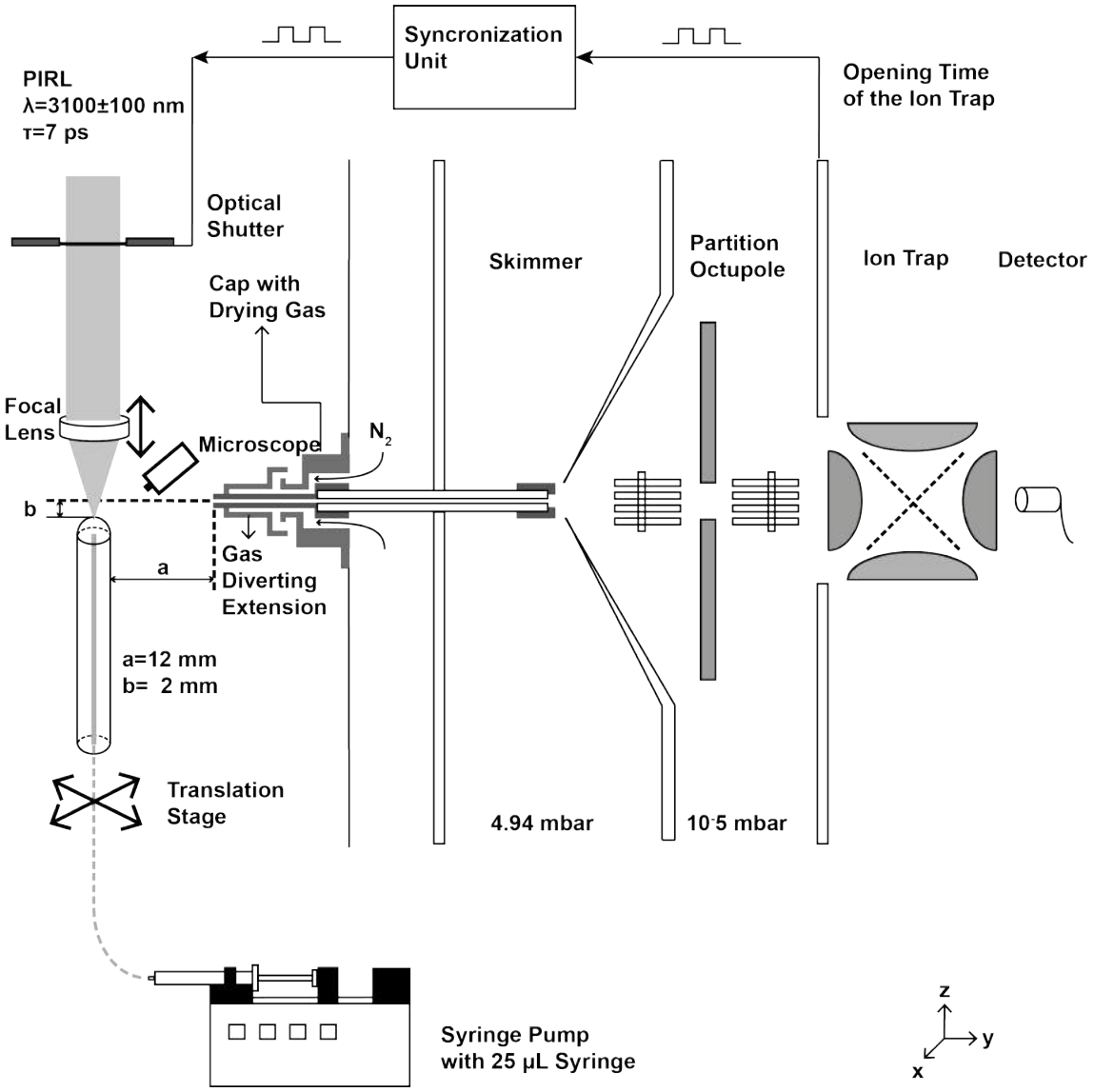

Figure 2.4: Schematic representation of the AP-DIVE-MS system. Analytes delivered via capillary flow are ablated by the PIRL laser operating under DIVE conditions and collected and mass-analyzed by a modified Bruker ion trap mass spectrometer.

the sample bead and control laser ablation process. It provided an image of the bead height and the corresponding ablation plume trajectory, which in turn helped with the system alignment and optimization for signal intensity, sensitivity, and stability.

2.3 Synchronization Electronics for AP-DIVE-MS

In order to increase system sensitivity as well as acquire stable and fully controllable PIRL ablation, a synchronization unit was designed and connected to optical shutter control and the control of the opening of the ion trap. The optical shutter is controlled by a LabVIEW program, which can select PIRL pulses in a single or burst pulse mode. As shown in Figure 2.5, when the synchronization unit receives the clock from the ion trap opening, it triggers the optical shutter to open allowing PIRL ablation and the molecular ions in the ablated plume to enter the trap for ion signal detection and further spectrum acquisition. It should be noted that the accumulation time of the trap opening should be shorter or equal to the shutter period. This allows full analysis of the ion signal from a series of pulses within one train in one shutter period without overlapping the signals originating from the next pulse train.

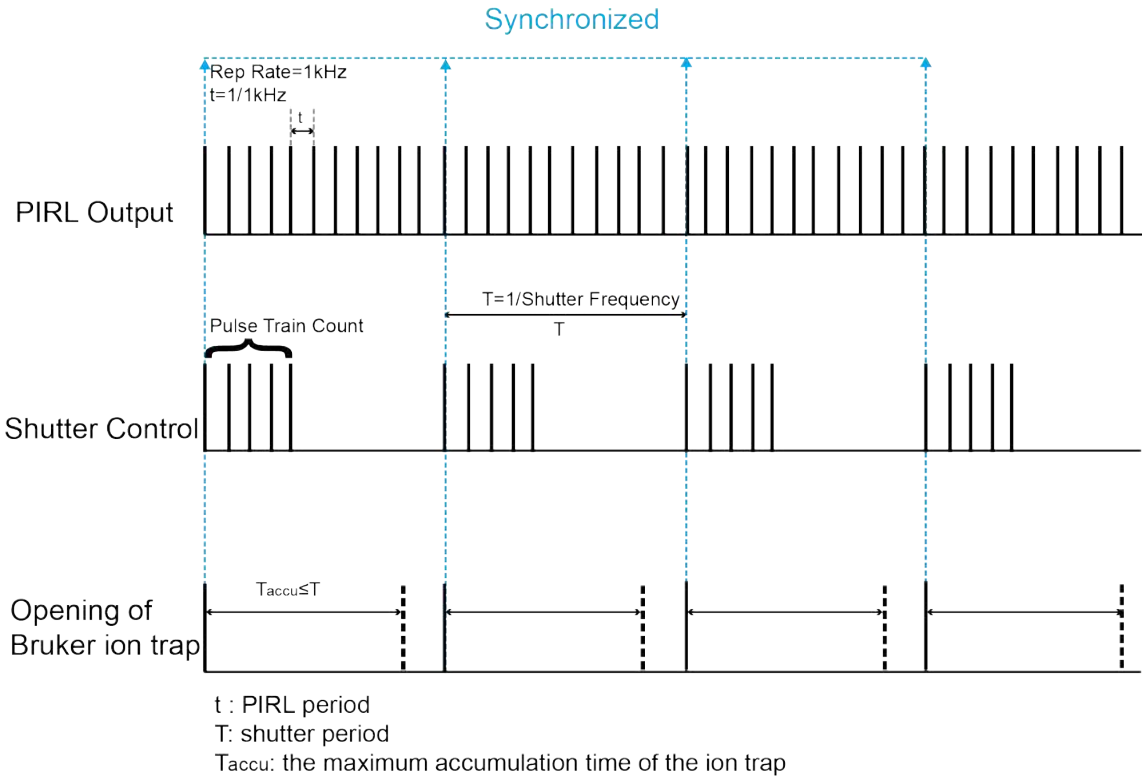

Figure 2.5: Electronic synchronization of the PIRL-MS system.

3. Characterization of AP-DIVE-MS from Continuous-Flow Aqueous Sample Delivery

Contributions from co-workers to Chapter 3: Wesley D. Robertson modified and developed the MS coupling interface with help from Djordje Gitaric. Cornelius Louwrens Pieterse programmed the shutter control interface in Labview. Erik Frieling and Wesley D. Robertson designed the gas diverting inlet extension. Wesley D. Robertson developed and implemented the synchronization circuit.

3.1 Optimizing the Flow Rate and PIRL Ablation Parameters

Optimizing the sample flow rate is the starting point of operating a capillary experiment. Due to the nature of aqueous samples, efforts need to be paid on balancing the evaporation of the liquid sample and sample consumption by laser ablation. Therefore a constant liquid delivery system was designed in order to acquire stable and reproducible signals. Characterization of the sample consumption is crucial in order to determine the sensitivity of the DIVE-MS system and the possibility to use

the same interface for microfluids and miniaturization, which are nowadays revolutionizing biomedical industry [80, 81]. This is the basis for developing the picoliter lab-on-a-chip interface of DIVE-MS, which will be discussed in detail in Chapter 5.

3.1.1 Optical Shutter Control of PIRL Ablation and Total Ion Current Generation

In Figure 2.5, the synchronization unit, which synchronizes the opening of the optical shutter and the gate of the Bruker Iontrap, was introduced in the diagram. Optical shutter control is of great importance for the AP-DIVE-MS for several reasons:

1. By using the shutter to work at very low frequency (∼Hz), the origin of the ion signal can be tested, i.e., whether it is from laser ablation or pure sample evaporation. When the opening and closing times of the optical shutter are much longer than the maximum accumulation time of the ion trap, it is expected that the ion intensity can reflect the response of the MS to the laser pulse trains' interaction with the sample during the corresponding period of time. As shown in Figure 3.1, the ion signal was only generated when the optical shutter was open and it decreased to zero when it was closed (opening time of shutter: 20 s, maximum accumulation time of ion trap: 50 ms). This demonstrates that laser ablation is the main source contributing to the ion signal of MS, while sample evaporation is almost negligible.

2. Optical shutter control considerably decreases sample consumption by preventing more laser pulses from interacting with the sample. And by optimizing the parameters of the shutter in the home-programmed Labview software, such as "shutter frequency" and "pulse train counts", it is possible to stabilize the height of sample bead with minimum flow rate in order to acquire highly stable and reproducible ion signals with good sensitivity.

3. When synchronized with the opening of the ion trap by the control unit, the optical shutter only allows the plume generation when the gate of the ion trap is open. Ions in the plume are directly guided into the ion trap with minimum loss

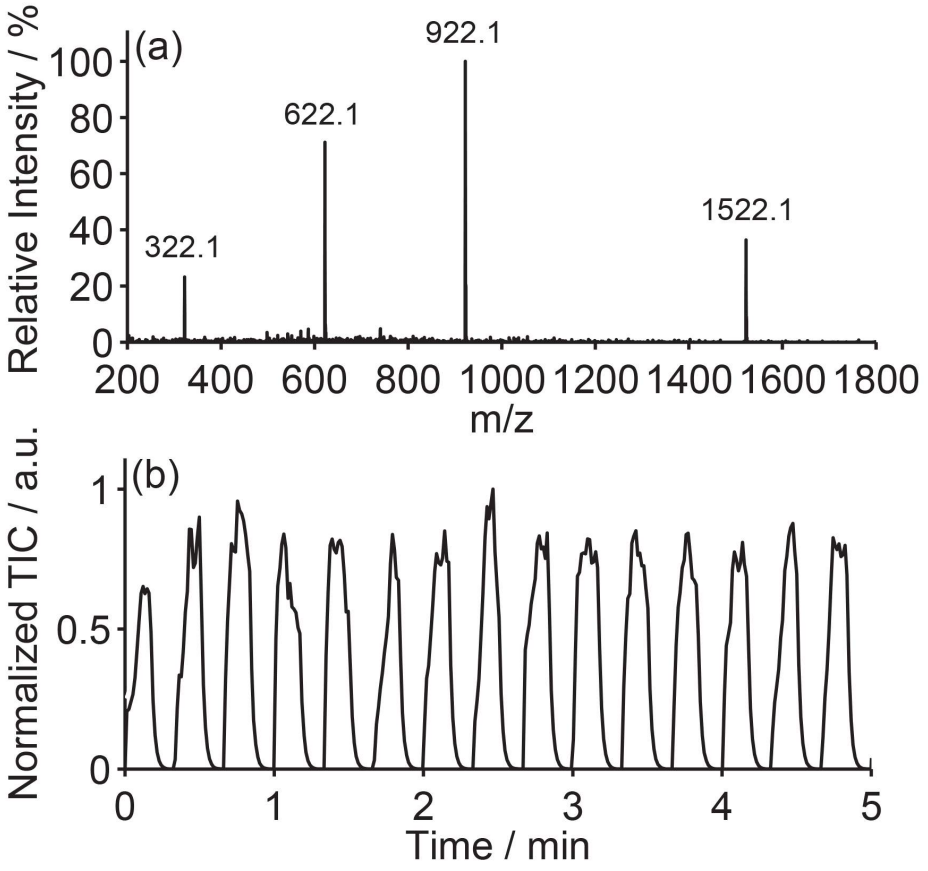

Figure 3.1: (a) DIVE-MS spectra of phosphazene compounds dissolved in water containing trifluoroacetic acid (TFA) ammonium salt (94.9 μM) and 5% acetonitrile. The m/z=322.1 peak shown is the result of the consumption of ~222.9 amol analyte (4 pulse bursts, 6 Hz, 5 seconds average). (b) Total ion current (TIC) for DIVE-MS (500 – 1000 m/z) during shuttering (20 s) of 1 kHz ablation pulse train confirming DIVE ion signal dependence.

caused by ion collisions inside the MS before reaching the trap. Therefore the system sensitivity is expected to be further enhanced. Moreover, it is then easier to analyze and calculate the response of single-pulse PIRL ablation from the sample, which will be introduced in the following sections.

3.1.2 PIRL Ablation Volume Estimation

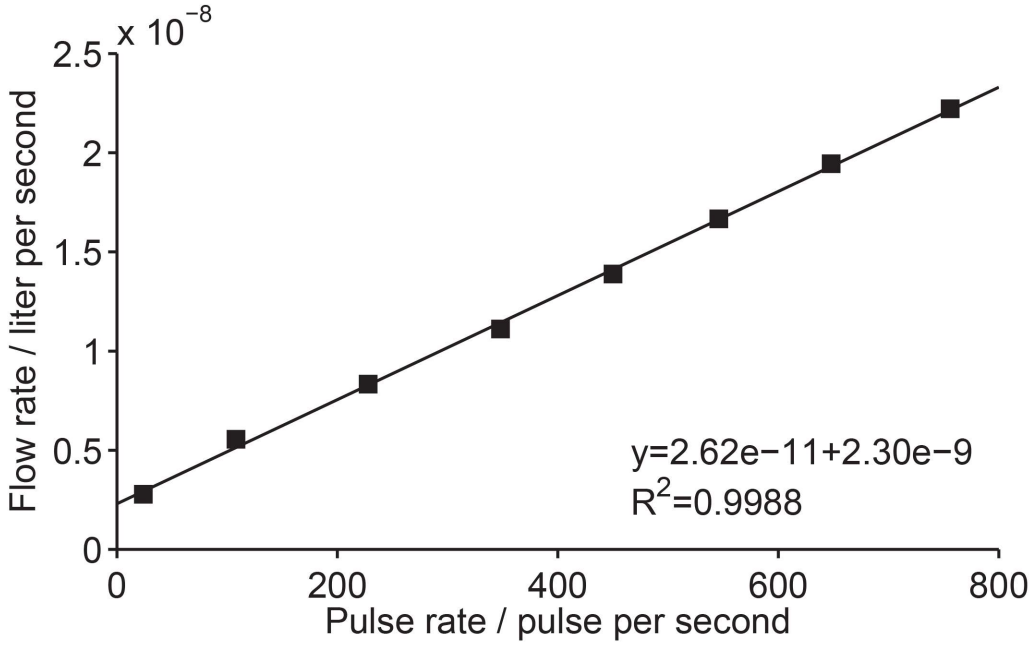

Figure 3.2: Sample flow rate versus pulse rate of DIVE ablation from the sample surface. The bead height of the sample remained constant during each measurement within 50 microns as monitored by a long working distance microscope. The slope of the curve indicates the volume of sample extracted per ablation pulse was 26.2 +/– picoliters. The sample used was tuning mix 2431a:water = 1:20 (v/v).

One key parameter for characterizing the AP-DIVE-MS from an aqueous sample

delivery system is the single-pulse ablation volume. Once the volume from single-pulse consumption is known, the sensitivity of the system can be estimated by using the lowest concentration of solution which is detectable. Figure 3.2 shows the relation between pulse rate (pulses per second) and flow rate (liter per second). For each data point, the sample bead height was stabilized within 50 μm of the surface for over 5 min. The slope of the calibration curve with calibration function $y = 2.62e^{-11} + 2.30e^{-9}$ and $R^2 = 0.9988$ revealed the estimated sample ablation volume per laser shot (liter per pulse), which was 26.2 picoliters for the system.

3.2 Characterization of Total Ion Current (TIC)

3.2.1 Stability of TIC

Stability of the ion current is the basis for acquiring reproducible spectra using the home-designed AP-DIVE-MS system. It is also the essential factor to demonstrate whether the flow rate versus laser shutter settings are optimized. As shown in Figure 3.3, the stability of the system was first characterized by diluted Agilent tuning mix G2431a in water (1:20 v/v) ranging from 200 – 1800 m/z. The total ion signal was stable for over 30 min with an average ion signal of 2×10^5 counts and a coefficient of variation (standard deviation/average) of 23.3%.

The stability of the TIC was also tested on a biological sample, 10 μm angiotensin I in 0.1% formic acid, as shown in Figure 3.4. The TIC signal exhibited stability for 30 min and a coefficient of variation of 18.4% with same shutter parameters and flow rate as the one in Figure 3.3, where singly, doubly, and triply charged states were found in the spectrum with high S/N ratio (not shown in the figure). This demonstrates that the stability of the system is reproducible for different sample types. The long stability of TIC is of great importance, as it is the basis for the linearity of a MS system and sheds light on the possibility of quantitative MS analysis.

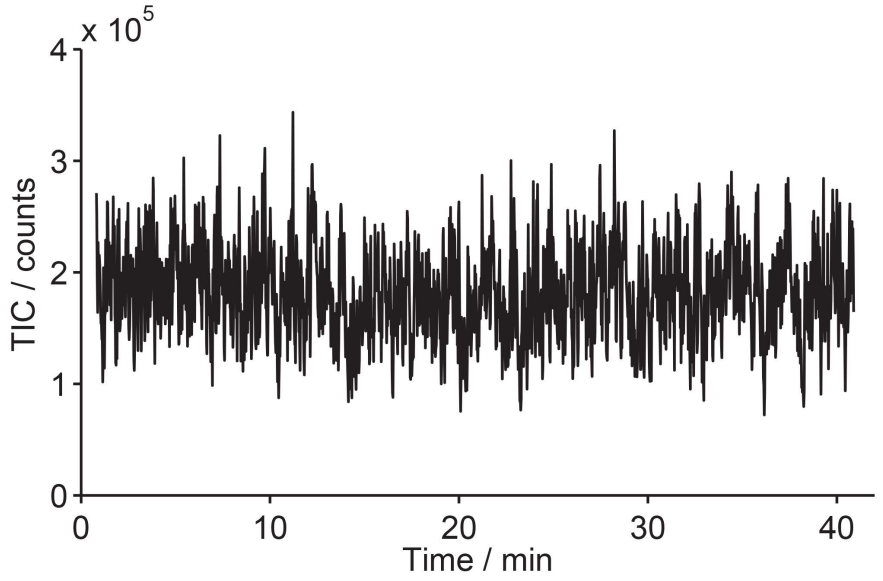

Figure 3.3: DIVE-MS total ion current (TIC) of hexamethoxyphosphazene (74 nM), hexakis(1H, 1H, 3H-tetrafluoropropoxy) phosphazene (986 nM), hexakis(1H, 1H, 5H-octafluoropropoxy) phosphazene (986 nM) and hexakis(2,2-difluoroethoxy) phosphazene (370 nM) from a water sample containing trifluoroacetic acid ammonium salt (TFA) (93.1 μM) and 5% acetonitrile. Mass range selected (200 – 1800 m/z), DIVE ablation shutter frequency 6 Hz, 4 pulse bursts, flow rate 167 nl/min. Figure taken from [82].

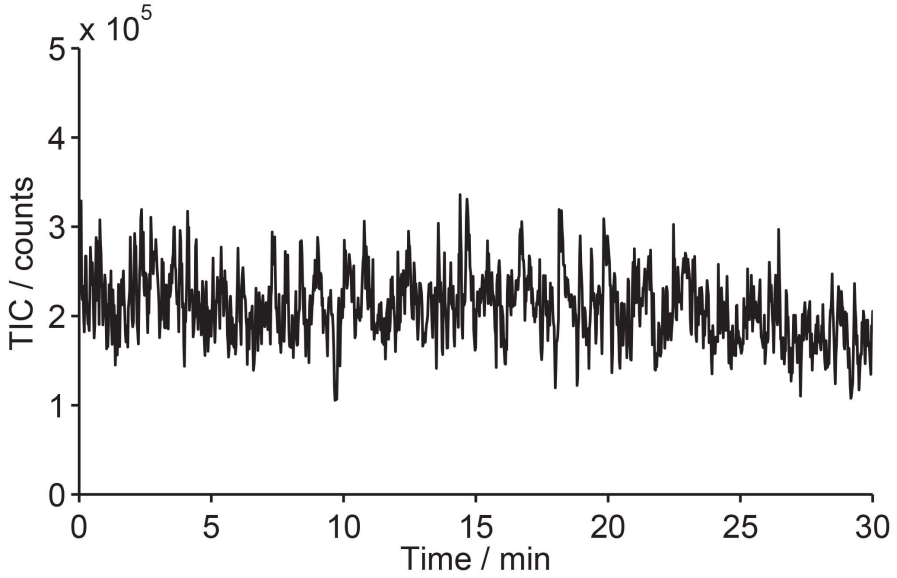

Figure 3.4: DIVE-MS total ion current (TIC) of angiotensin I (10 μM) in water with 0.1% formic acid. DIVE ablation shutter frequency 6 Hz, 4 pulse bursts, flow rate 167 nl/min. Figure taken from [82].

3.2.2 Capillary Voltage Dependence of TIC

The capillary voltage is the voltage applied directly to the inlet transfer glass capillary of the MS. A voltage drop of 500 V is set between the capillary and the end plate, which is a metal plate directly positioned behind the MS inlet shield. It should be noted that the sample delivery tube is a clear-cut PEEK tubing which is mounted by metal mounts onto the breadboard. Therefore no direct high voltage is applied to the tube as well as the sample bead.

As shown in Figure 3.5, the relation between capillary voltage and ion signal intensity was explored. The trend line can be divided into three regimes to be discussed individually:

First, the 500–1500 volt range: in the low voltage range, the ion signal was almost ignorable compared to higher voltage counterparts and can be regarded as the baseline noise of the system. This shows that the interface can not work under a low

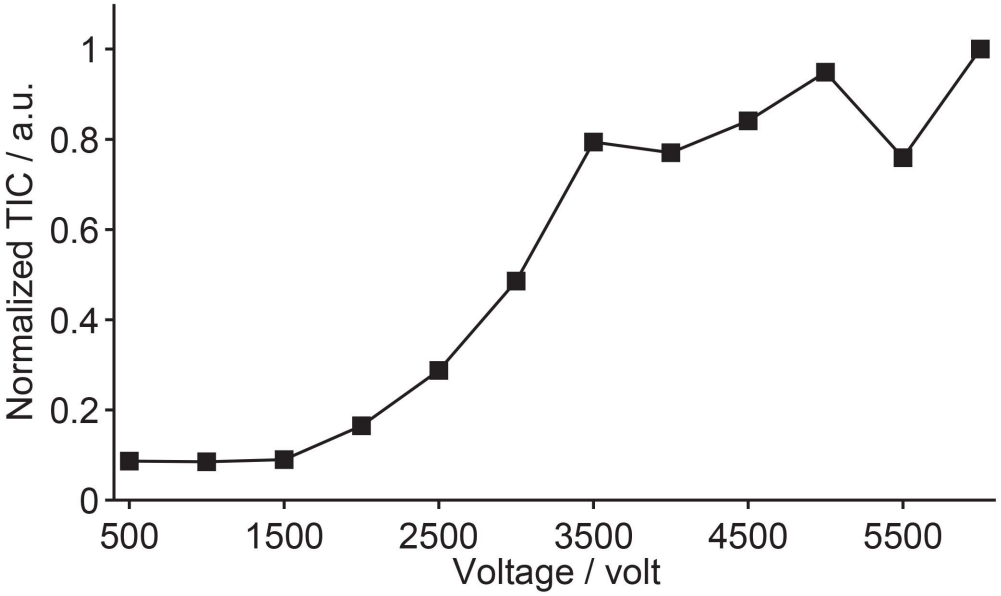

Figure 3.5: Voltage dependence of TIC of cytochrome c versus capillary voltage. The sample and experimental conditions were 10 μM cytochrome c in water with 0.1% formic acid, flow rate 167 nl/min, shutter frequency 6 Hz, 4 pulse bursts, and an averaging time for each data point of 1 min. Figure taken from [82].

capillary voltage condition.

Second, the 1500 – 3500 volt range: in the medium voltage range, the higher the capillary voltage applied, the higher the observed ion signal observed.

Third, the 3500 – 6000 volt range: in the high voltage range, the ion signal slightly increased when higher voltage was applied, yet the rate of increase was much lower than the one in the medium voltage range.

Moreover, as the mount of the sample delivery tube and other components of the interface are made out of metal, the dimensions of the interface are very tight, and the interface is positioned extremely close to the MS inlet, it was risky to apply extremely high voltages. Sparks were observed on the lens mount when the voltage was set as 6000 volt. By trial and error, the optimum voltage for operating all the experiments was determined to be $\mp$4500 volt for positive and negative ion modes, respectively.

As will be discussed in detail in Chapter 4, the tendency of ion intensity dependence on the capillary is one of the key factors that may contribute to the charging mechanism of AP-DIVE-MS. Interestingly, a similar relation was not only shown in our interface, but also for other AP-MS techniques, such as inlet ionization, sonic spray and laser spray.

3.2.3 Inlet Temperature Dependence of TIC

One thing that needs to be emphasized before any temperature discussion starts is that all the temperature values mentioned in this thesis are the one measured by thermalcouple at the inlet of the MS. The real temperature at the MS inlet depends on the temperature settings in the control software as well as the dry gas flow rate. Figure 3.6 and 3.7 present the relations between the temperature settings in the software and the real measured temperatures by the thermalcouple at dry gas flow rate of 10 l/min and 0.5 l/min, respectively.

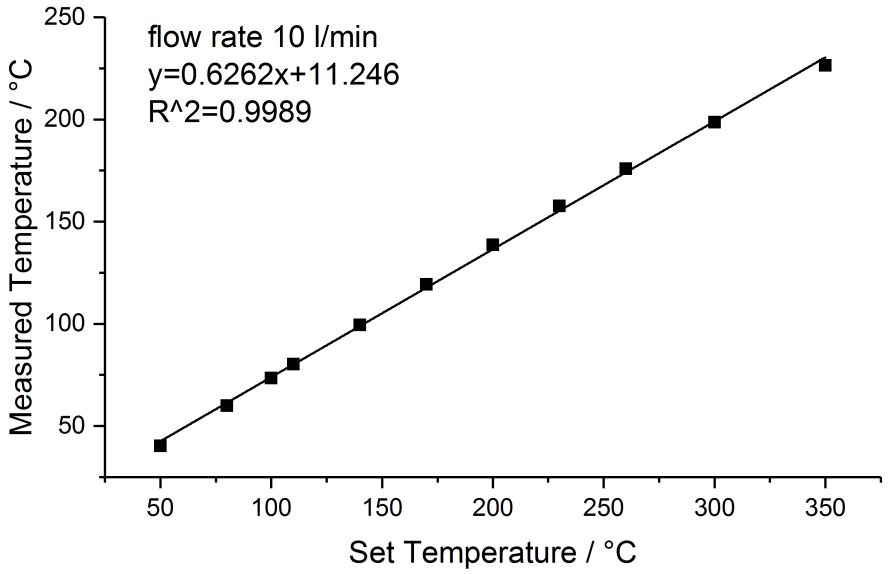

Figure 3.6: The relation between the temperature settings in the control software and the measured one by thermalcouple at dry gas flow rate 10 l/min.

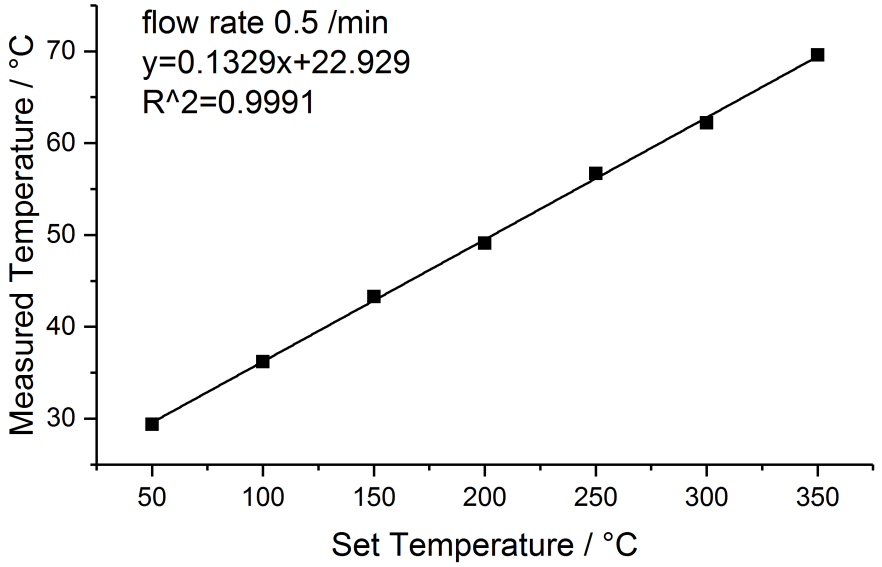

Figure 3.7: The relation between the temperature settings in the control software and the measured one by thermalcouple at dry gas flow rate 0.5 l/min.

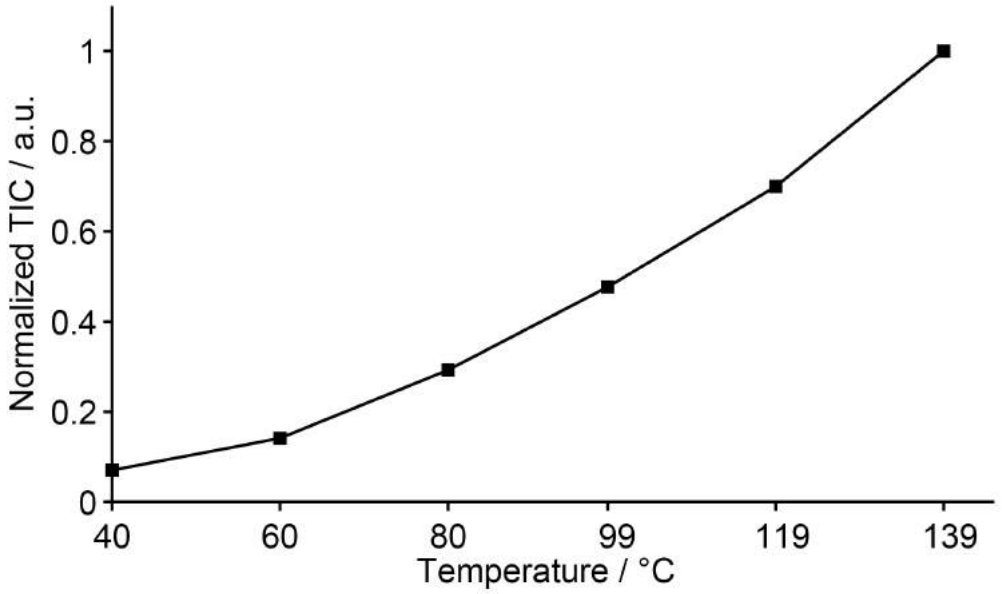

Figure 3.8: Temperature dependence of TIC of cytochrome c. The gas diverting heated capillary extension was used and established thermal equilibrium before data collection. DIVE ablation was performed on 10 μM cytochrome c in pure water without addition of acid, flow rate 167 nl/min, shutter frequency 6 Hz, 4 pulse bursts and an averaging time for each data point of 1 min. Figure taken from [82].

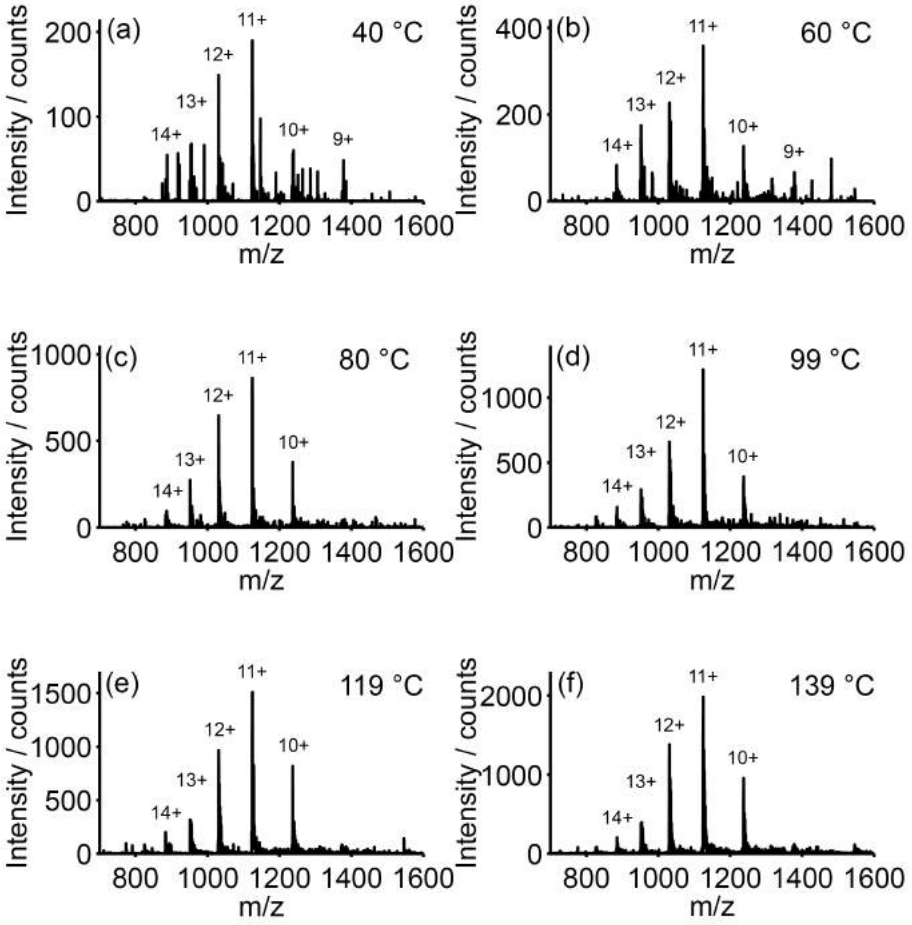

Figure 3.9: DIVE-MS spectra of cytochrome c in pure water without the addition of acid, collected at transfer capillary temperatures ranging from 40 °C to 139 °C. The mass spectra were obtained from the TIC shown in Figure 3.8 at each temperature. DIVE ablation was performed on 10 μM cytochrome c in pure water without addition of acid, flow rate 167 nl/min, shutter frequency 6 Hz, 4 pulse bursts and an averaging time for each spectrum of 1 min. Figure taken from [82].

The same sample, which was used to explore the capillary voltage dependence of TIC, was also applied to study the inlet temperature dependence of the ion signal. The mechanism of inlet temperature control is as follows: the temperature of the heated nitrogen gas was monitored by the heater, the temperature of which was set in the MS software. Meanwhile, the nitrogen gas flow was coming out of the MS inlet and heated up by the heater. For the original Bruker ion trap configuration, the heated nitrogen gas collided with the droplets generated by the nebulizer in the spray chamber to acquire finer desolvated droplets. However, the flow rate of 10 l/min was too high as the laser ablation was blown away from reaching the MS inlet. Therefore in order to obtain both full temperature of the inlet and no interruption to the plume, the gas diverting inlet extension was applied to accomplish the purposes mentioned above.

In addition to the ion signal dependence on capillary voltage, its dependence on inlet temperature was another essential factor in studying the charging mechanism of AP-DIVE-MS, which will be introduced in the following chapter. As shown in Figure 3.8, the ion signal intensity increased by over one order of magnitude when the inlet temperature was raised from 40 to 139 °C. As cytochrome c is a protein with multiply charged states, the ion intensities of each charging state for different temperatures were carefully examined in Figure 3.9, which lead to the following direct observations:

1. In the low temperature regime (40–60 °C), the total ion intensity, as well as the ion intensities of each charging state were lower than higher temperature counterparts. In addition, high background noise also greatly contributed to the total ion intensity and the S/N ratio was very low.

2. In the medium to high temperature regime (80–139 °C), ion intensities for each charging state and total ion intensities increased dramatically when the temperature became higher. Furthermore the S/N ratio was considerably improved in this temperature regime while the relative relations among different charging states for the same temperature remained unaltered.

3. It should be noted that the ion intensity distribution, which centered at +11 charging states, did not change over the measurement. And this charging state with wide charge distribution indicated that the cytochrome c protein was already denatured. This was probably due to applying the gas diverting extension. Efficient heat transfer in the extension made it so hot that the protein would unfold. Another possibility is that dissolving cytochrome c in pure water solution may cause of the instability of the structure of the protein.

3.3 Single-Pulse Response

The single-pulse response is one of the essential features to characterize the sensitivity of the PIRL-DIVE-MS system. As the ultimate goal of PIRL-DIVE-MS is to operate MS imaging on the cellular level, single-shot response can greatly minimize the potential damage on the cell caused by multiple laser shots. This also enables the possibility to detect low quantity molecules directly from the sample. In Figure 2.1, calculation of the laser ablation volume was performed for AP-DIVE-MS from the calibration curve, in which the single PIRL ablation volume at the focal plane was estimated to be 26.2 picoliters. As a result, the spectrum resulting from single-pulse response in our setup corresponds to the averaged spectrum of 26.2 pl sample consumption.

Figure 3.10 shows the spectrum of 10 μM angiotensin I in pure water from single PIRL ablation, in which all the typical charging states (+1, +2, +3) of angiotensin I are presented. Although there is observable background noise between the second and first charging states, the S/N is sufficient to discern the characteristic spectrum of the sample. Moreover, compared to the spectrum of PIRL ablation from the same sample under multiple laser shots shown in Figure 4.11(a), the charging distribution, which is centered at +2 did not alter, while +1 and +3 were more evident in the single-pulse response. This can be explained by the fact that the spectrum in Figure 4.11(a) was an average for longer time period (1 min) and both +1 and +3 were averaged out as they were not as stable as +2. For the single-pulse spectrum, it

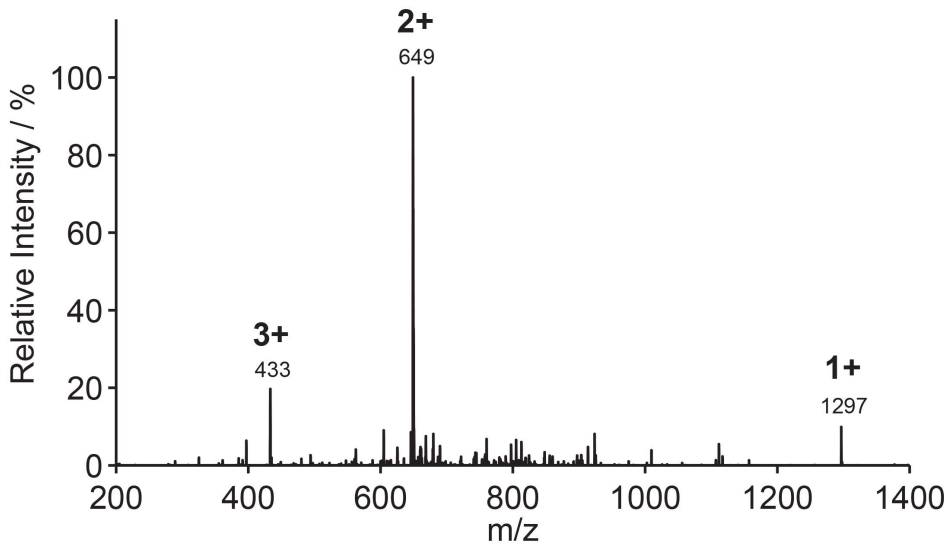

Figure 3.10: DIVE-MS spectra of angiotensin I (10 μM) in pure water from a single PIRL laser pulse (26.2 pL volume extraction). Figure taken from [82].

was close to the impulse response, which was an average within one pulse ablation and was very short. Therefore the spectrum may differ from Figure 3.10 due to the averaging over much longer time and more pulses in this earlier discussed work.

The total ion signal of angiotension I for single-pulse response is displayed in Figure 3.11, where the TIC remained stable for 10 min. Compared to Figure 3.4, the TIC in Figure 3.11 was less stable and fluctuated much more. This is due to the single shot of laser ablation with only 26.2 pl sample volume consumption. In addition, for single pulse ablation, it was more delicate to control the sample bead in the focal plane. However, it was clearly demonstrated by the data shown in Figure 3.9 that the TIC was kept at a baseline of 2×10^5, which is comparable to the one in Figure 3.4 for the same concentration of angiotensin I.

In short, as the single-pulse mass spectrum is easily discernible and relatively re-

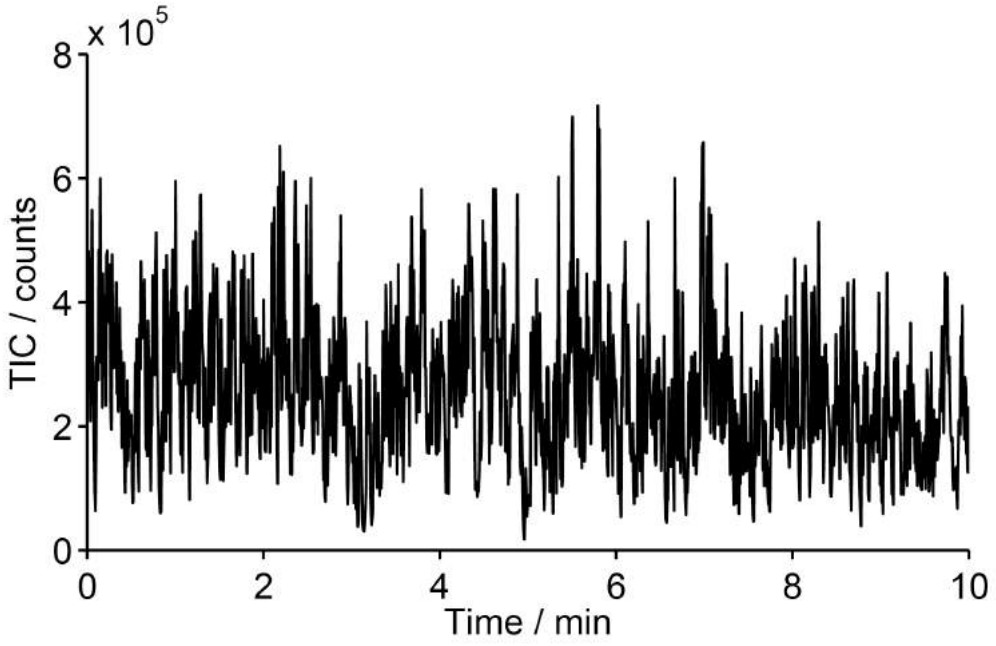

Figure 3.11: DIVE-MS total ion current (TIC) MS spectrum of angiotensin I (10 μM) in pure water for single PIRL laser pulse extraction. DIVE ablation shutter frequency 1 Hz, 1 pulse burst, flow rate 167 nl/min, and capillary temperature 300 °C. Figure taken from [82].

producible, the AP-DIVE-MS interface has the potential to measure low abundance molecules in tissue or low concentration aqueous samples. In addition, it sheds light on the prospects of applying the AP-DIVE-MS for fast examination of bio-samples for medical purposes.

3.4 Sensitivity of the System

Different from the single-pulse response, where the minimum number of laser pulses was explored in order to obtain typical MS spectrum from a sample, sensitivity is another key parameter to demonstrate. Sensitivity quantifies the minimum amount of sample that needs to be provided such that the AP-DIVE-MS system is capable of detecting the characteristic output spectrum of that sample. Meanwhile, as it is sometimes difficult for aqueous samples to estimate volume or quantity, the limit of detection (LOD) quantity is more widely used and defined as the lowest concentration of sample that can be reliably detected. It should be emphasized that within this thesis, "detectable" means that the S/N ratio is larger or equal to 3.

In order to explore the LOD of the AP-DIVE-MS system, which is usually sample dependent, small molecules and peptides (including angiotensin I and II, and acetaminophen) were used for testing. As shown in Figure 3.12(a) and (b), 10 nM of angiotensin I and II in water with 0.1% formic acid were ablated, where the spectra of the second charging state for angiotensin I (m/z=649) and angiotensin II (m/z=524) were measured and averaged for 6 s from total ion intensities, which corresponds to 39 amol sample consumption. In Figure 3.12(c), the same concentration of acetaminophen dissolved in pure water was also tested and averaged for 6 s. For all three spectra in Figure 3.12, the S/N was larger than 3 and hence detectable, though the absolute ion intensity was very low.

Furthermore, the sensitivity or LOD was also examined by using a sample mixture. As illustrated in Figure 3.13, diluted Agilent G2431a tuning mix (tuning mix:water=0.5:10, v/v) which contained hexamethoxyphosphazene, hexakis(1H, 1H,

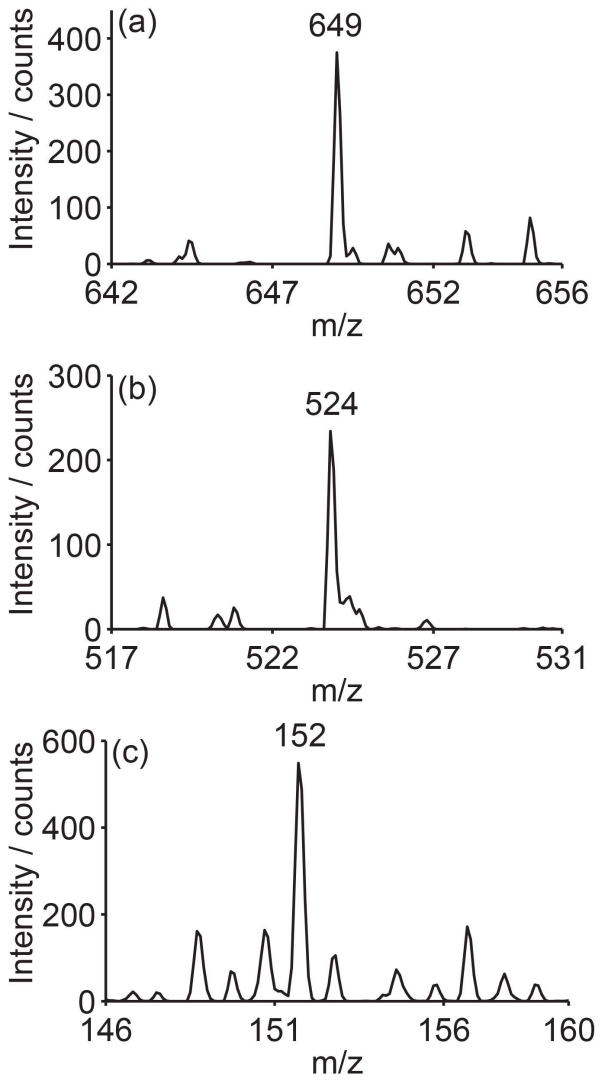

Figure 3.12: DIVE-MS limit of detection (LOD) spectra. (a) DIVE-MS spectrum, $[M+2H]^{2+}$, corresponding to 39 amol angiotensin I dissolved in water containing 0.1% formic acid. (b) DIVE-MS spectrum, $[M+2H]^{2+}$, corresponding to 39 amol angiotensin I dissolved in water containing 0.1% formic acid. (c) DIVE-MS spectrum, $[M+H]^{+}$, corresponding to 39 amol acetaminophen in pure water. These mass spectra are the average of 6 s of data collection, shutter frequency 6 Hz, 4 pulse bursts, flow rate 167 nl/min. Figure taken from [82].

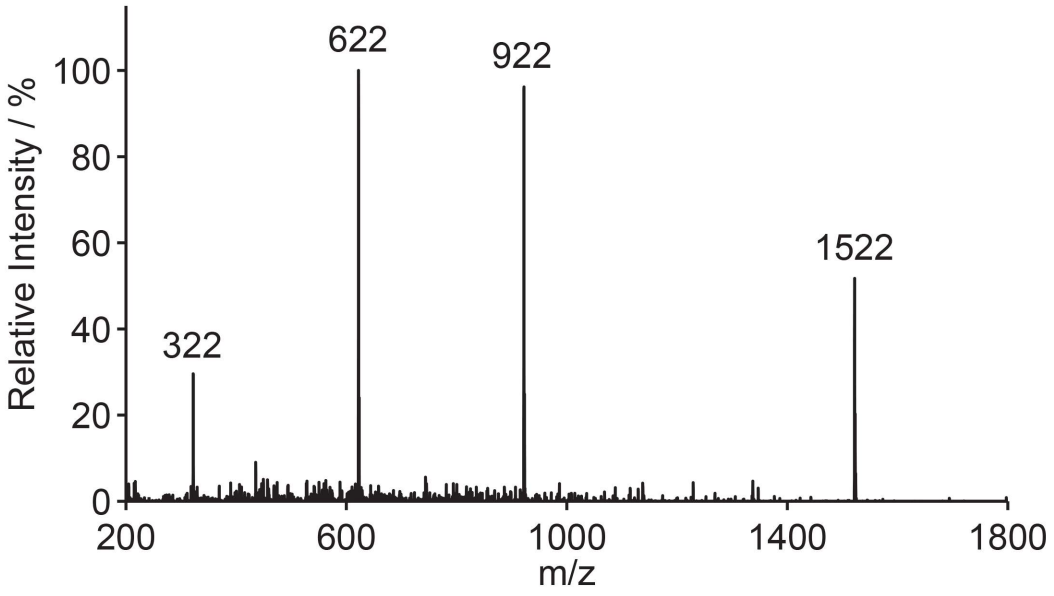

Figure 3.13: The DIVE-MS spectra of phosphazene compounds averaged for 1 second from water containing trifluoroacetic acid ammonium salt (TFA) (93.1 μM) and 5% acetonitrile. Total consumption of analyte corresponds to: hexamethoxyphosphazene (48 amol), hexakis(1H, 1H, 3H-tetrafluoropropoxy phosphazene (639 amol), hexakis(1H, 1H, 5H-octafluoropropoxy) phosphazene (639 amol) and hexakis(2,2-difluoroethoxy) phosphazene (240 amol). DIVE ablation shutter frequency 6 Hz, 4 pulse bursts, flow rate 167 nl/min. Figure taken from [82].

3H-tetrafluoropropoxy) phosphazene, hexakis(1H, 1H, 5H-octafluoropropoxy) phosphazene, and hexakis(2,2-difluoroethoxy) phosphazene. By averaging 1 s of TIC, all the analytes with spectra shown in Figure 3.13 correspond to a sample consumption in the amol range. The lowest sample consumption was from hexamethoxyphosphazene with 48 amol.

3.5 Summary

To summarize this chapter, characterization of the AP-DIVE-MS was performed by optimizing the sample flow rate, establishing long-term TIC stability and the relation between TIC and capillary voltage or inlet temperature, and exploring the single-pulse response and sensitivity of the system. Flow rate was optimized by studying the relation between optical shutter control and sample consumption under certain sample flow rate in order to obtain stable ion signals. A flow rate of 167 nL/min was applied with shutter frequency 6 Hz and 4 pulse burst for most of the experimental results presented in this thesis, which is comparable to NanoESI. Long-term TIC stability of ESI tuning mix and peptides were demonstrated longer or equal to 30 min. TIC was observed to primarily increase and then saturate when capillary voltage was scaled from 500 to 6000 volts. The temperature of inlet capillary also has influenced the TIC, a monotonic increase of TIC was observed when inlet temperature was increased from 40 to 139 °C. Mass spectrum of cytochrome c was already discernible at low temperature of 50 °C by applying gas diverting inlet extension. Mass spectrum by single pulse ablation was established with relatively stable TIC. System sensitivity was demonstrated as LOD of 10 nM, which corresponds to 39 amol sample consumption. And mass spectrum of an average of 1s sample consumption of ESI tuning mix was made with sample consumption ranging from 48 to 639 amol.

4. Generation of Singly and Multiply Charged Small Molecule, Peptide and Protein Ions by AP-DIVE-MS from Continuous-Flow Aqueous Sample Delivery

Contributions from co-workers to Chapter 4: Wesley D. Robertson modified and developed the MS coupling interface with assistance from Djordje Gitaric. Cornelius Louwrens Pieterse programmed the shutter control interface in Labview. Erik Frieling and Wesley D. Robertson designed the gas diverting inlet extension. Wesley D. Robertson designed and built the synchronization circuit and control. Jean-Michel Boudreau prepared the native protein samples.

4.1 Sample Preparation

Table 4.1 summarizes analytes and stock solutions, which were used for obtaining the mass spectra presented in this thesis. All the analytes, including small molecules, peptides and proteins, were used without further purification. Sam-

Table 4.1: Samples used in PIRL-DIVE-MS experiments.

Sample type	Sample name	Grade	Part No.	Manufacturer
Small molecules	Caffeine	$\geq$ 99% HPLC	C0750	Sigma-Aldrich Chemie GmbH
Small molecules	Acetaminophen	$\geq$ 99% BioXtra	A7085	Sigma-Aldrich Chemie GmbH
Peptide	Angiotensin I acetate salt hydrate	$\geq$ 90% HPLC	A9650	Sigma-Aldrich Chemie GmbH
Peptide	Angiotensin II human	$\geq$ 93% HPLC	A9525	Sigma-Aldrich Chemie GmbH
Peptide	Bombesin	$\geq$ 97% HPLC	B4272	Sigma-Aldrich Chemie GmbH
Protein	Cytochrome c from equine heart	$\geq$ 95% SDS-PAGE	C2506	Sigma-Aldrich Chemie GmbH
Protein	Lysozyme from chicken egg white	$\geq$ 90%	L7651	Sigma-Aldrich Chemie GmbH
Protein	Bovine serum albumin	$\geq$ 98%	A7906	Sigma-Aldrich Chemie GmbH
Protein	Myoglobin from horse skeletal muscle	95-100%	M0630	Sigma-Aldrich Chemie GmbH
Acid	Acetic acid	$\geq$ 99.99%	338826	Sigma-Aldrich Chemie GmbH
Acid	Formic acid	LC-MS Ultra	14265	Fluka
Buffer	Ammonium acetate	$\geq$ 99%	73594	Sigma-Aldrich Chemie GmbH
Buffer	Ammonium bicarbonate	$\geq$ 99.5% BioUltra	9830	Sigma-Aldrich Chemie GmbH
Tuning mix	Agilent G2431a	mixture	A935023	Agilent
Water	Deionized distilled water	>18.5 MΩ cm	PURELAB Classics	Elga Veolia

ple solutions for AP-DIVE-MS and ESI were prepared in deionized distilled water with/without acid (0.1-1% formic or acetic acid). Native protein solutions were prepared in 10 mM ammonium acetate buffer on ice with pH 7.0, which followed the same procedure as discussed in Zenobi's work [83]. Agilent G2431a ESI tuning mix was combined with water in a ratio of 1:20 (v/v), resulting in a final solution of hexamethoxyphosphazene (71 nM), hexakis(1H, 1H, 3H-tetrafluoropropoxy) phosphazene (986 nM), hexakis(1H, 1H, 5H-octafluoropropoxy) phosphazene (949 nM) and hexakis(2,2-difluoroethoxy) phosphazene (357 nM) with trifluoroacetic acid ammonium salt (TFA) (93 μM) and 5% acetonitrile. Additional mobile phase solvents, such as acetone or methanol, may be added to ESI sample solutions and will be explicitly mentioned in the sample conditions in the experiments presented later..

4.2 Results and Discussions

In this section, major results from small molecules, peptides and proteins, which cover nearly the entire detection range of the Bruker ion trap for AP-DIVE-MS, will be presented and discussed. These results will be compared to ESI results using the same sample conditions. Moreover, in order to explore the possible charging mechanism of AP-DIVE-MS, results on analytes in pure water solution will be presented and differentiated from other AP-MS techniques.

4.2.1 Small Molecules

AP-DIVE-MS spectra of small molecules, including caffeine and acetaminophen, are reported in Figure 4.1(a) and (c). Direct comparisons with their ESI counterparts under the same sample conditions are presented in Figure 4.1(b) and (d). It should be noted that the ESI spectra were obtained from a home-built interface in AP condition without the original spray chamber.

For mass spectra of 100 μM caffeine in water containing 0.1 % acetic acid (v/v), singly charged spectra (m/z=195) are observed for both DIVE and ESI with the

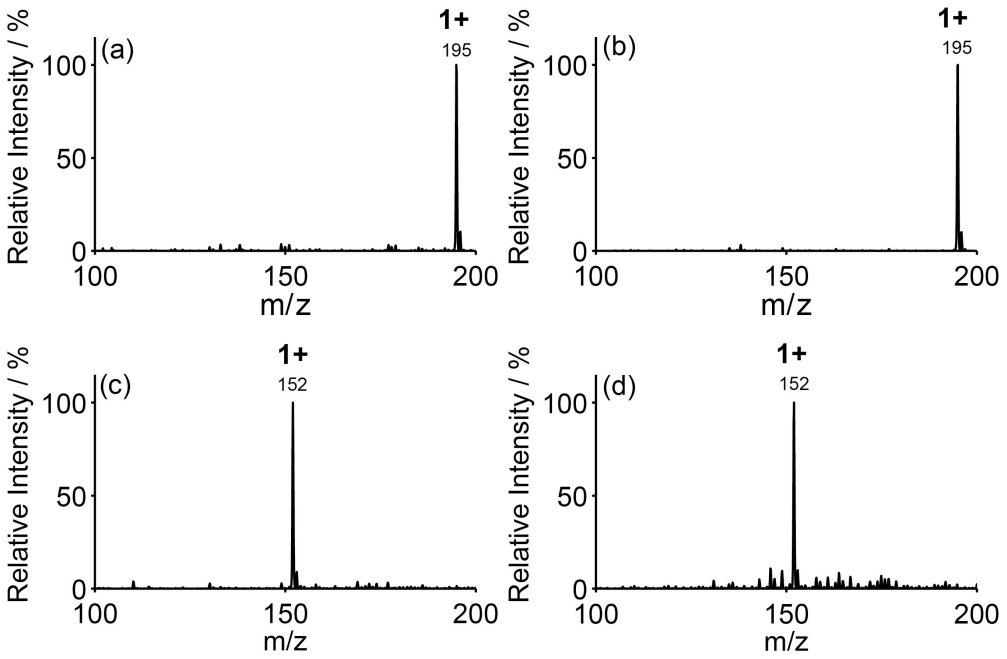

Figure 4.1: Mass spectra of caffeine (100 μM) in water containing 0.1% acetic acid (v/v) (a) DIVE-MS (flow rate 835 nl/min, shutter frequency 2 Hz, 100 pulse bursts, without gas diverting heated transfer extension) and (b) ESI (flow rate 3 μl/min). Mass spectra of acetaminophen (10 μM) in water containing 0.5% formic acid (v/v) for (c) DIVE-MS (flow rate 417 nl/min, shutter frequency 5 Hz, 150 pulse burst, without without gas diverting heated transfer extension) and (d) ESI (flow rate 3 μl/min). The spectra shown are the average for 1 minute. Transfer capillary temperature was 36 °C. Figure taken from [82].

major fragment (m/z=138) almost negligible [84]. As caffeine can easily decompose, mainly by breaking the aromatic ring, under atmospheric condition, the lack of fragments in AP-DIVE-MS indicates the soft nature of this method, which is comparable to ESI.

For the mass spectra of 10 μM acetaminophen in water containing 0.5 % formic acid (v/v), the singly charged state (m/z=152) was demonstrated for both DIVE and ESI. The major fragment (m/z=110) did not appear in both spectra, which was mainly caused by thermal or hydrolytic degradation, though the S/N in ESI was worse than in AP-DIVE-MS [85]. This again confirmed that both AP-DIVE-MS and ESI are soft MS techniques that reduce the fragmentation during MS analysis.

4.2.2 Peptides

Various peptides, including angiotensin I and bombesin, were used to demonstrate the functionality of AP-DIVE-MS. MS/MS of angiotensin I was compared with that obtained by ESI. In addition, by comparing the mass spectra of bombesin obtained by AP-DIVE-MS and ESI, differences in adduct formation will be demonstrated and discussed in detail.

Figure 4.2(a) reports the AP-DIVE-MS of angiotensin I. Singly (m/z=1297), doubly (m/z=649) and triply (m/z=433) charged states of the analyte are present with the highest intensity of the second charging state, where collision induced dissociation spectrum (CID-MS/MS) was generated and the corresponding mass spectrum is presented in Figure 4.2(b). The major fragment ions are in accordance with Roepstorf and Fohlman nomenclature [86]. The precursor ion mass isolation window was set to 4 mass units (m/z of the precursor ion $\pm$2) with the fragmentation time of 40 ms. The collision gas was helium and the fragmentation amplitude was varied to achieve the required degree of fragmentation.

The same sample, from which the spectra in Figure 4.2 were obtained, was used for the ESI spectra shown in Figure 4.3 for comparison. For the mass spectrum of

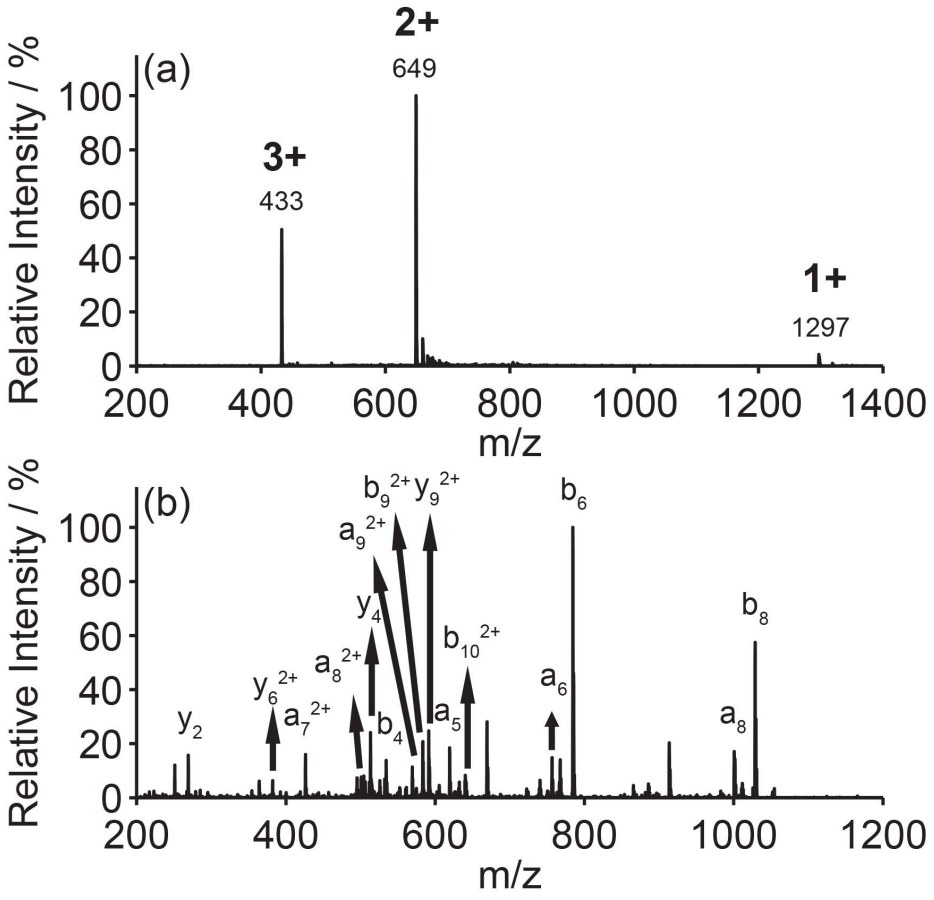

Figure 4.2: (a) DIVE-MS mass spectrum of the peptide angiotensin I (10 μM) in water containing 0.1% formic acid (v/v). (b) Collisionally induced dissociation spectrum of the doubly charged species of angiotensin I, $[M+H]^{2+}$, produced by DIVE-MS. Spectra correspond to $\sim$ 377.3 fmol of analyte consumed. Transfer capillary temperature was 199 °C. Figure taken from [82].

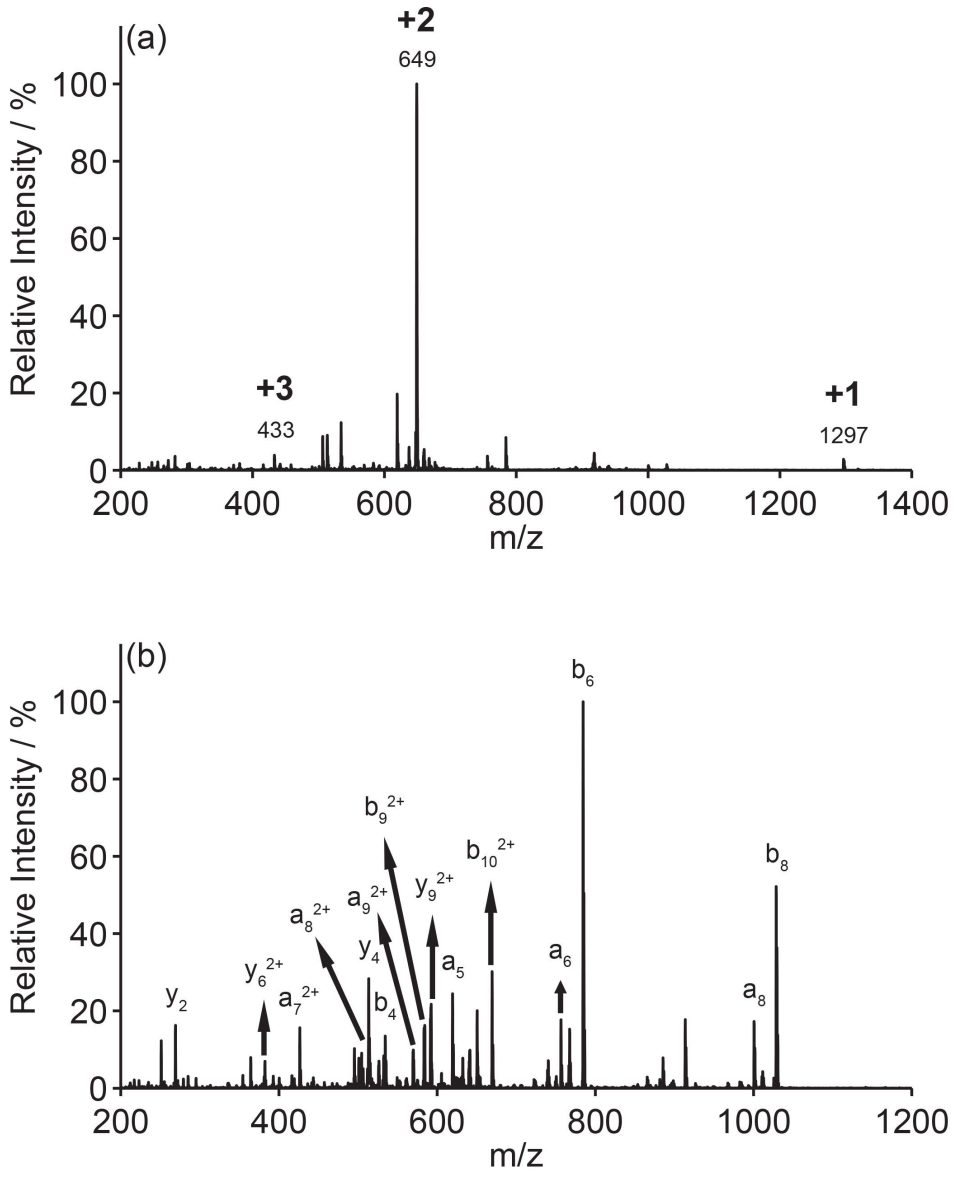

Figure 4.3: (a) ESI mass spectrum of the peptide angiotensin I (10μM) in water containing 0.1% formic acid (v/v). (b) Collision induced dissociation spectrum of the doubly charged species of angiotensin I, $[M+H]^{2+}$, produced by ESI-MS. ESI flow rate 3 μL/min. No gas diverting heated transfer extension was applied. Transfer capillary temperature was 199 °C. Figure taken from [82].

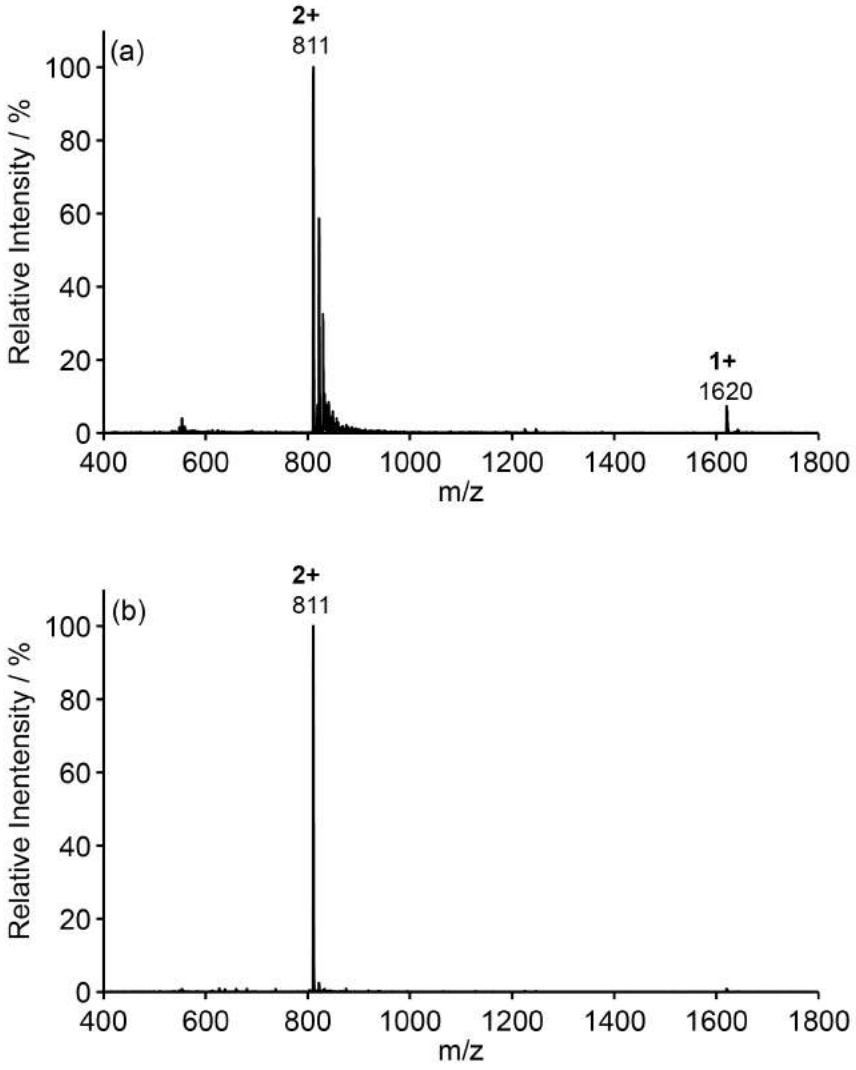

Figure 4.4: (a) DIVE-MS mass spectrum of the peptide bombesin (10μM) in water containing 0.5% acetic acid (v/v). (b) ESI-MS mass spectrum of the peptide bombesin (10μM) in water containing 0.5% acetic acid (v/v).

angiotensin I in Figure 4.3(a), the S/N was much worse for the triply and doubly charged states in ESI compared to AP-DIVE-MS. In addition, the triply charged states of angiotensin I in ESI were hidden inside the background noise and exhibited much lower relative intensity. Furthermore, relatively small fractions ($< 10\%$) of adduct ions were observed for the doubly charged state and no additional fragmentation peaks were noted. However, for the singly charged state, both AP-DIVE-MS and ESI spectra exhibited very low relative intensities. This indicates that AP-DIVE-MS might share a similar charging process as conventional ESI, where highly charged ions are formed by the desolvation process of charged droplets.

For the CID-MS/MS of angiotensin I displayed in Figure 4.3(b), nearly identical mass spectra were obtained from both AP-DIVE-MS and ESI, though some small differences in relative intensity for certain fragments, such as a_8^{2+} and a_5, were observable in the spectra. This again indicates that AP-DIVE-MS can develop stable highly charged ions for tandem MS, as is typically utilized by standard nebulization based methods for fragmentation based proteomic identification. Similar CID-MS/MS of angiotensin I were reported using other AP-MS techniques, such as surface acoustic nebulization MS [44], where the major fragments are the same as in AP-DIVE-MS.

Figure 4.4 presents the mass spectrum of 10 μM bombesin in water containing 0.5 % acetic acid (v/v) by AP-DIVE-MS and conventional ESI. There are two major differences between these two spectra: first, singly charged states of bombesin were only observed in AP-DIVE-MS. This indicates that the charging efficiency of AP-DIVE-MS for bombesin was not as high as ESI. Second, the salt adducts at the side of doubly charged states of bombesin were only present in AP-DIVE-MS. The adduct ion signal in AP-DIVE-MS was carefully examined, and types of adduct salts included the doubly charged state of bombesin bound with sodium, potassium and the doubly charged bombesin state bound with these two salt adducts. The difference between the two mass spectra implies that there is a different underlying charging mechanism between AP-DIVE-MS and ESI, where the ion suppression was much less in the former than the latter.

4.2.3 Proteins

Protein mass spectra play an important role in system characterization and are widely used to test the softness and charging ability of MS interfaces. In this section, mass spectra of different proteins, such as cytochrome c and lysozyme, under diverse sample conditions and MS settings were demonstrated. In addition, the softness of AP-DIVE-MS was explored by obtaining the native protein spectrum. And highly charged spectra from different protein species were also studied.

Cytochrome c is a commonly used and thoroughly studied protein species, which is utilized in this thesis as a 'test sample' to optimize PIRL and compare AP-DIVE-MS to other AP-MS interfaces [87, 88, 87, 89, 90, 91, 10]. As shown in Figure 4.5, 10 μM cytochrome c in distilled water with 0.5% acetic acid (v/v) was used for AP-DIVE-MS without applying the gas diverting extension. Both positive and negative ion modes were tested by simply switching the capillary voltage from negative to positive. Highly charged ions up to 12+ were detected in the positive ion mode as reported in Figure 4.5(a), and up to 11– in the negative ion mode shown in Figure 4.5(b). The wide charge distributions (positive ion mode: 7+ to 12+; negative ion mode: 7– to 11–) of cytochrome c indicate that cytochrome c was partially unfolded in this experiment. Yet there was a portion of cytochrome c still remaining intact, as the 7th and 8th charging state is the mark of an intact protein under this sample pH condition.

The gas diverting inlet extension was applied and its influence on protein spectra is shown in Figure 4.6. 10 μM cytochrome c in water with 0.1% formic acid (Figure 4.6(a)) or in pure water (Figure 4.6(b)) were ablated, and the plume was transferred into the gas diverting inlet extension. The wide charging distributions in the mass spectra of 10+ to 15+ for cytochrome c in 0.1 % formic acid solution and 10+ to 14+ in pure water indicate that cytochrome c was unfolded when the gas diverting inlet extension was applied in this experiment. In addition, the small shift of charging state centered from 12+ in water containing 0.1% formic acid to 11+ in pure water suggests that the unfolding might have already occurred before entering the MS.

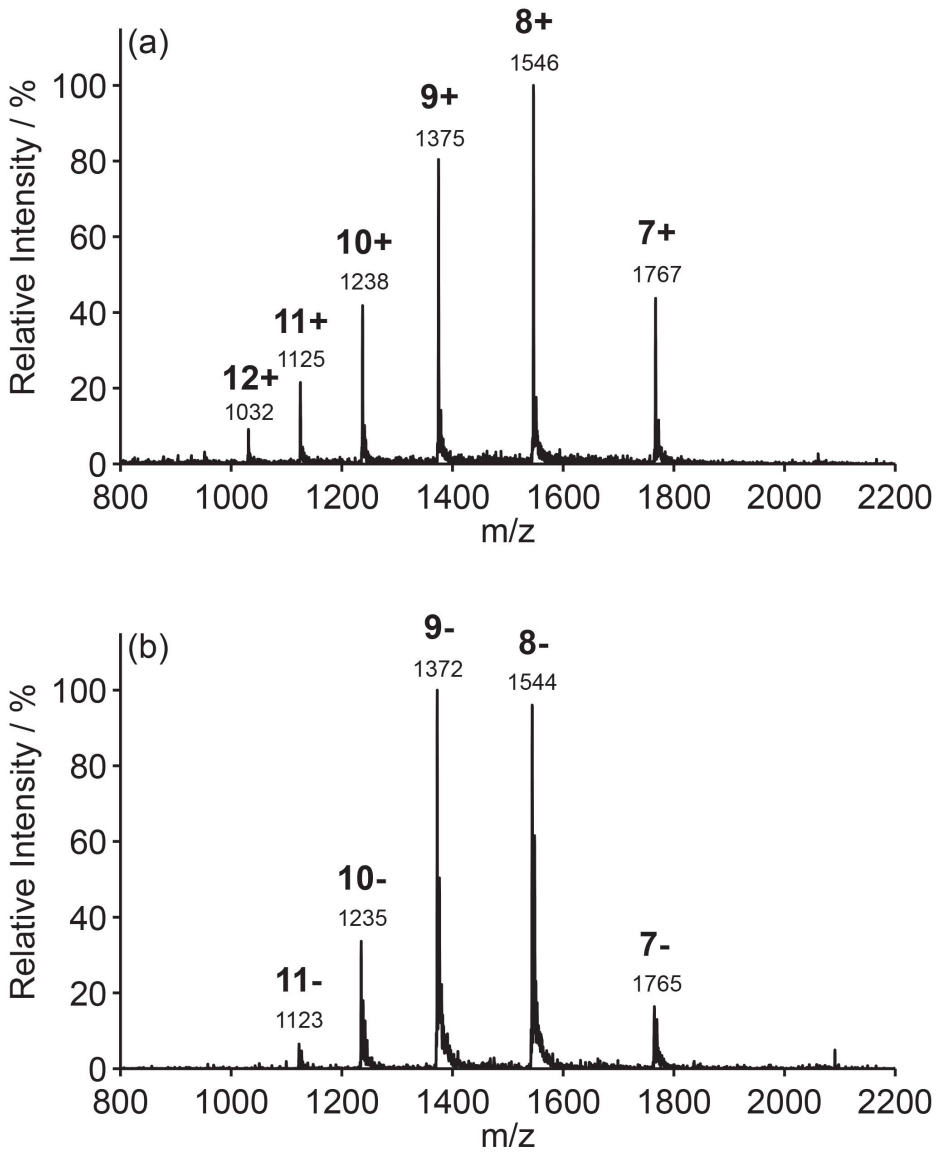

Figure 4.5: DIVE-MS spectra of cytochrome c (10 μM) for (a) positive and (b) negative ion mode. Cytochrome c was prepared in distilled water with 0.5% acetic acid (v/v). DIVE ablation shutter frequency 2 Hz, 100 pulse burst, flow rate 833 nl/min. The spectra shown are the average of 1 min of data collection without background correction. No gas diverting heated transfer extension was applied, and capillary transfer temperature was 36 °C. Figure taken from [82].

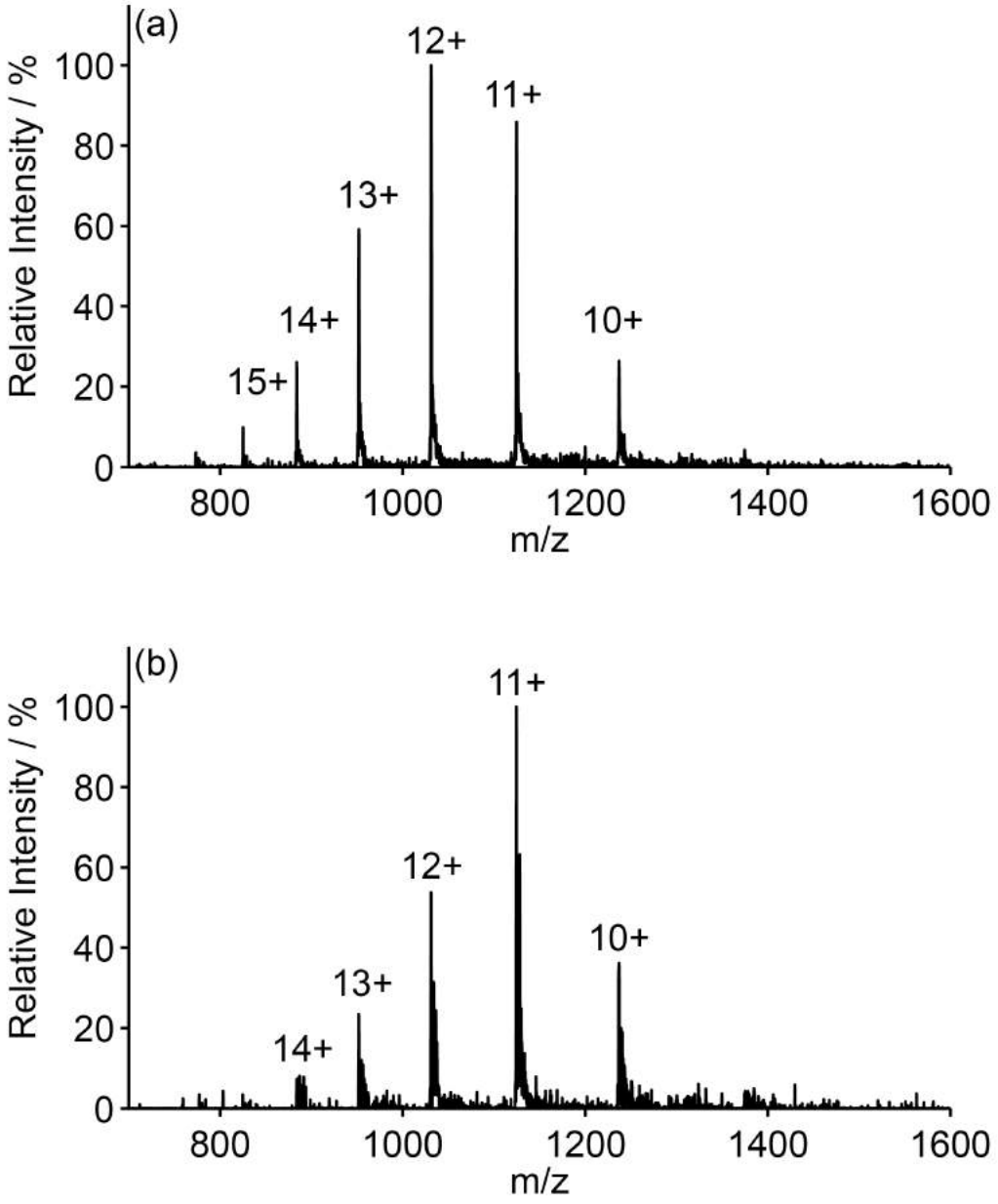

Figure 4.6: DIVE-MS spectrum of cytochrome c (10 μM) (a) in water containing 0.1 % formic acid, (b) in acid-free pure water. Transfer capillary temperature was 74 °C. Figure taken from [82].

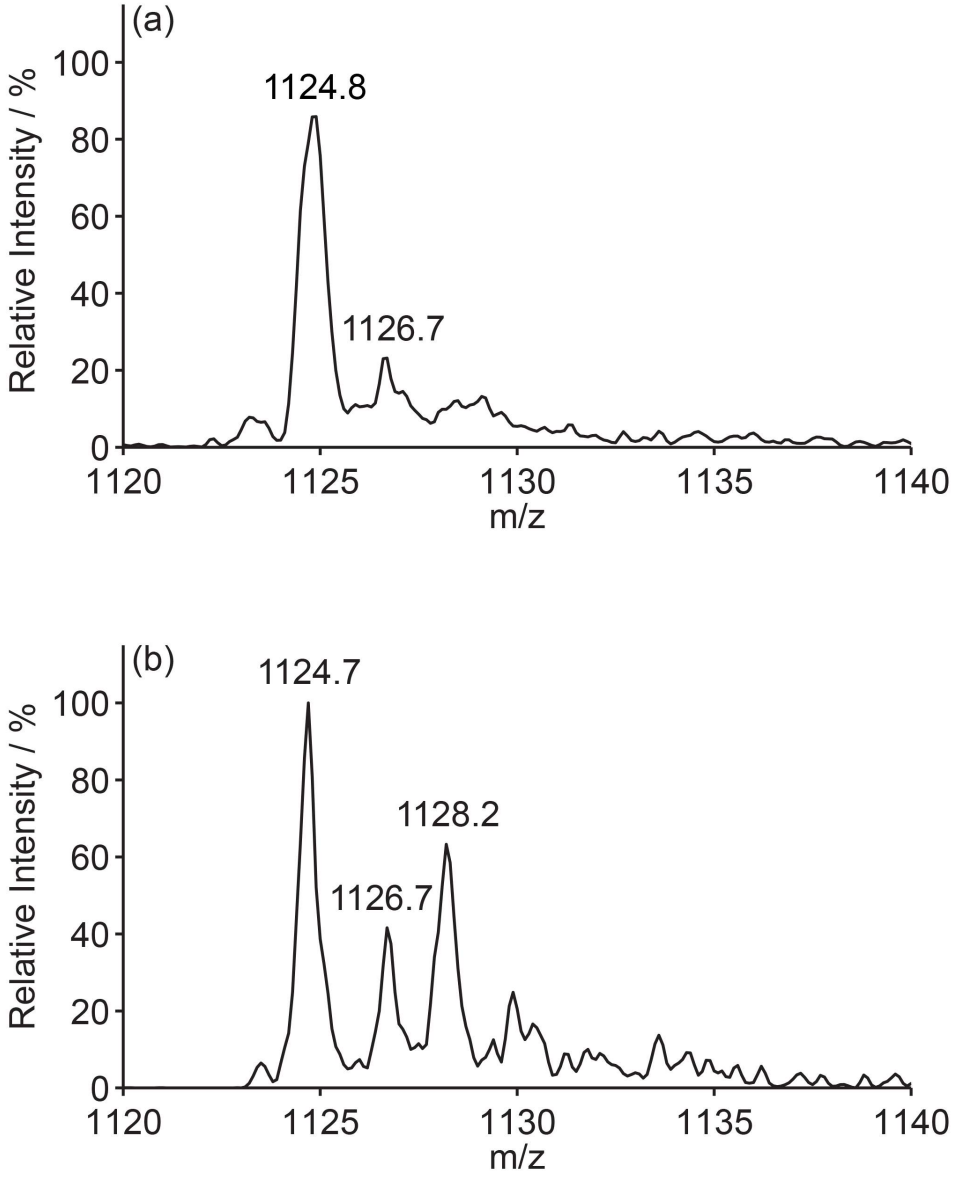

Figure 4.7: Comparison of DIVE-MS of adducts for the +11 charge states of cytochrome c between (a) water solution with 0.1% formic acid and (b) pure water. The 1126.7 and 1128.2 m/z peaks correspond to sodium and potassium adducts, respectively. DIVE ablation was performed at a flow rate of 167 nl/min, shutter frequency 6 Hz, 4 pulse bursts, averaging time for each spectrum was 1 min, transfer capillary temperature was 74 °C. Figure taken from [82].

Another indication is that in Figure 4.5, when no extension was utilized, the charging state is centered at 8+ indicating a more native state of the protein. Therefore, it is likely that, on the one hand, the gas diverting extension helps to increase the total ion signal by a more efficient heat conduction. On the other hand, the extension's high temperature and long tube might have caused protein unfolding by heating and collisions on the inner wall of the tube.

Although the charge distributions were similar between cytochrome c in water with 0.1% formic acid and in pure water, the absolute ion intensity in pure water solution was 50% lower than the acetic counterpart (not shown in Figure 4.6). In addition, the adduct distributions under these two sample conditions also exhibited differences, as demonstrated in Figure 4.7. The adducts for the 11+ charge state of cytochrome c are compared between (a) in water with 0.1% formic acid and (b) in pure water. The main peak with m/z of 1124.8 in (a) and 1124.7 in (b) corresponds to the 11+ of cytochrome c. Comparing both spectra reveals that sodium adduct with m/z of 1126.7 was present in the spectra under both sample conditions, while potassium adduct with m/z of 1128.2 was only observed in the pure water spectrum. Moreover, the relative intensity of adducts to the 11+ peak of cytochrome c was much higher in pure water compared to the one in acetic water solution, possibly due to the different pH of the solutions.

For the AP-DIVE-MS interface, not only the highly charged states of protein analytes were explored, but also the native state of the protein species. As presented in Figure 4.8, 10 mM ammonium acetate buffer solution with pH 7.0 was used to dissolve 10 μM cytochrome c analyte. Only two charge states, 7+ and 8+, were observed in the MS spectrum, which indicates the folded structure of the analyte after PIRL ablation and afterwards for further MS analysis. It should be noted that for all the cytochrome c measurements, the settings and parameters in the MS control software remained constant. In addition, no gas diverting extension was applied during native MS study, to avoid potential overheating and inner tube wall collisions of proteins. The result shows the softness of AP-DIVE-MS. It also reveals that

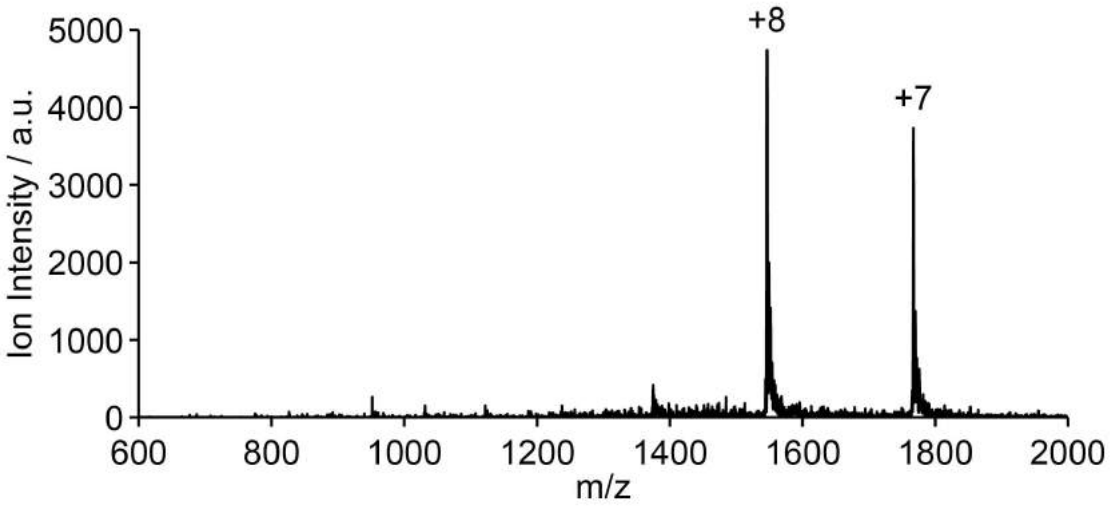

Figure 4.8: Native DIVE-MS spectrum of cytochrome c (10 μM) in 10 mM ammonium acetate buffer. No gas diverting heated transfer extension was applied, and the transfer capillary temperature was set to be 62 °C. Figure taken from [82].

the highly charged MS spectra of cytochrome c might be ascribed to the unstable solution condition, such as sample pH, when the protein was dissolved. Another possible explanation of partially unfolded protein MS spectra might be attributed to the atmospheric environment condition, where PIRL ablation collided with air when transferring into the MS inlet with ultrasonic speed. These collisions could possibly cause the unfolding of proteins in the plume.

While ammonium acetate buffer helps to obtain the nearly native MS spectrum of cytochrome c, another widely used buffer, ammonium bicarbonate, was applied for lysozyme sample preparation. As shown in Figure 4.9, 10 μM lysozyme was added to 10 mM ammonium bicarbonate buffer solution. Charge states from 8+ to 16+ are present in the measured MS spectrum. The highly charged states up to 16+ and the wide charge state distribution demonstrate the unfolded state of lysozyme when it was detected by MS. The reason for the unfolding of lysozyme in buffer solution is still unclear. Yet by performing experiments on protein samples under

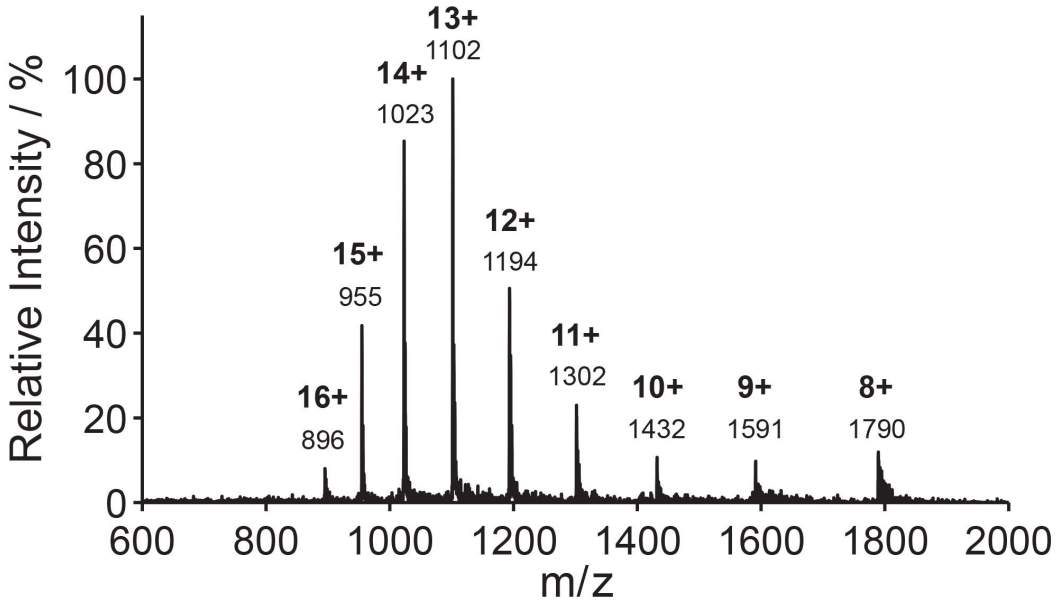

Figure 4.9: DIVE-MS spectrum of 10 μM chicken white lysozyme in 10 mM ammonium bicarbonate buffer. DIVE ablation shutter frequency 6 Hz, 4 pulse burst, flow rate 167 nl/min. The spectrum shown is the average of 1 min of data collection without the use of the additional gas diverting heated transfer extension and transfer capillary temperature of 36 °C.

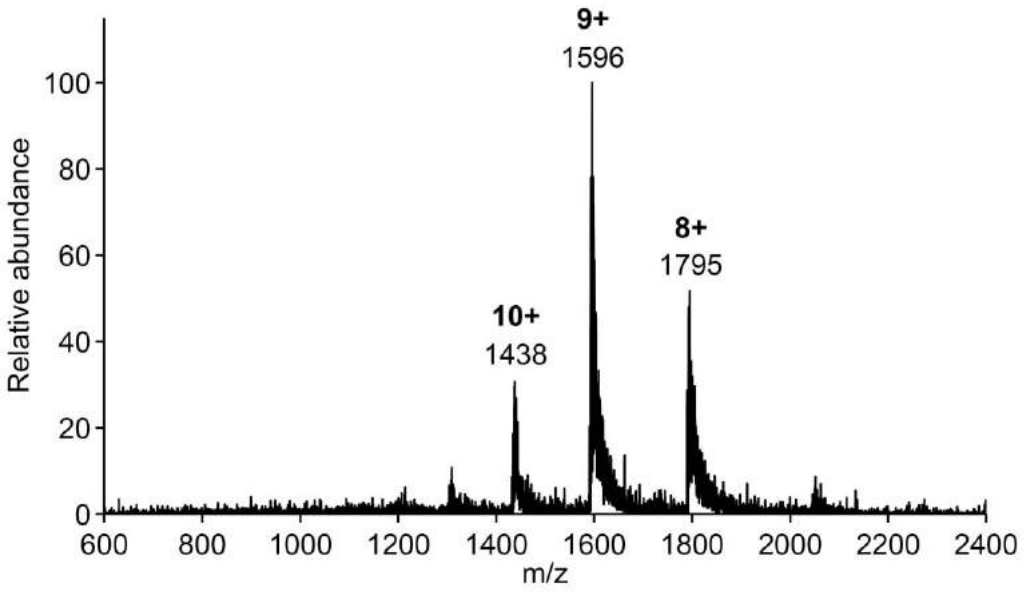

Figure 4.10: DIVE-MS spectrum of 10 μM chicken white lysozyme in 50 mM ammonium bicarbonate buffer. DIVE ablation shutter frequency 6 Hz, 4 pulse burst, flow rate 167 nL/min. The spectra shown was the average of 1 min of data collection without the use of the additional gas diverting heated transfer extension and transfer capillary temperature of 36 °C. Figure taken from [82].

different conditions, it was found that for AP-DIVE-MS, the final spectrum was the result of collective factors, such as inlet temperature, MS inlet gas flow rate, ion-trap settings, and accumulation time etc. For example, mass spectrum for the same concentration of lysozyme, which was desolved in higher concentration (50 mM) of ammonium bicarbonate buffer, is presented in Figure 4.10. The much narrower charge distribution (10+, 9+, 8+) centered at 9+ implies a nearly folded structure of lysozyme detected by MS. In this case, it seems that the buffer concentration helps to stabilize the structure of proteins.

In summary, the AP-DIVE-MS interface allows one to perform aqueous protein sample measurements with highly charged MS spectra. By optimizing the MS parameters as well as sample conditions of protein solutions, AP-DIVE-MS has the potential to obtain the native spectrum of the analyte, which is highly sensitive to sample and MS conditions.

4.2.4 Molecules in Water

For most of the AP-DIVE-MS spectra presented in this thesis, the analytes were usually dissolved in acetic (pH 2-3) or buffer (pH 7-8) solutions. Yet one question was addressed whether this is necessary, or simple water solution would be sufficient. As the isoelectrical point (pI) for most of the analytes is not 7.0, it can be expected that there could be net charges on the molecules when it was dissolved in pure water solution. Moreover, net charges might also exist in the PIRL ablation plume, which consists of thousands of droplets that contain analytes.

Figure 4.11 displays the mass spectra of 10 μM angiotensin I (a), angiotensin I (b) and acetaminophen (c) in pure water solution. The pI of angiotensin I, angiotensin II and acetaminophen are 6.92, 6.74, 9.38, accordingly. For angiotensin I, the second charged state (m/z=649) exhibited much higher intensity than the first (m/z=1297) and third (m/z=433) charged states, both of which were almost negligible relative to the second charged state. For angiotensin II, a similar intensity relation was found, where the intensity of the second charged state (m/z=524) was

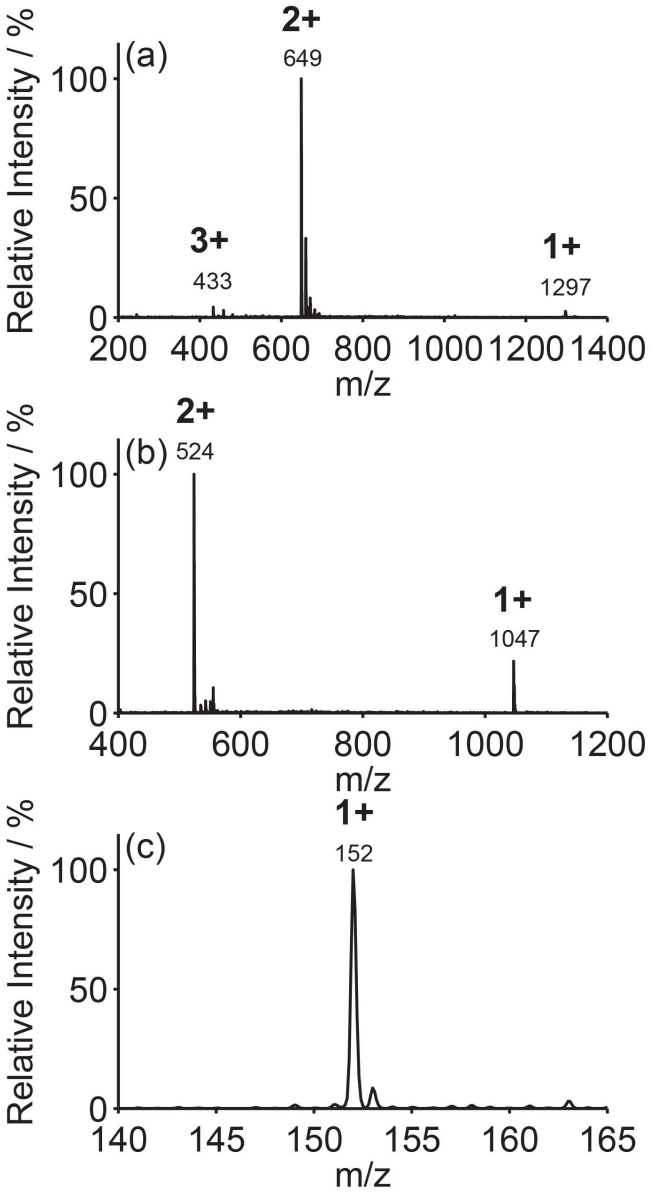

Figure 4.11: DIVE-MS spectra in pure water without the addition of an acid. (a) DIVE-MS spectrum, $[M+H]^{1+}$, $[M+2H]^{2+}$ and $[M+3H]^{3+}$, of 10 μM angiotensin I dissolved in water. (b) DIVE-MS spectrum, $[M+H]^{1+}$ and $[M+2H]^{2+}$, of 10 μM angiotensin II dissolved in water. (c) DIVE-MS spectrum, $[M+H]^{+}$, of 10 μM acetaminophen dissolved in water. DIVE ablation shutter frequency 6 Hz, 4 pulse bursts, flow rate 167 nl/min. The mass spectra are the average of 1 min of data collection. Transfer capillary temperature was 139 °C. Figure taken from [82].

almost 4 times higher than the first charged state (m/z=1047). For the small drug molecule acetaminophen, only the singly charged state (m/z=152) was present in the spectrum.

4.3 Charging Mechanisms

Both the theoretical simulations and experimental results on plume dynamics of PIRL introduced in Chapter 1 shows that PIRL ablation plume consists of gas phase front followed by superheated droplets inside the plume. After 1 μs, the secondary recoil droplets are generated, which contain a considerable portion of the material of the ablated volume. Jing Zou's simulations show that over 90% of the water molecules are stripped off from lysozyme within 1 ns after PIRL ablation without fragmentation [79]. This can be regarded as the possible ionization model for the direct gaseous ions generation, which has great potential for in vacuum sample delivery and very think samples. As droplets from recoil make up a large portion of the PIRL ablation plume, the potential charging process for droplets will be discussed in this section.

4.3.1 Overview on Current Models

The charging mechanism of AP-DIVE is still not completely understood. Yet by comparing the results with other ionization techniques in AP, such as sonic spray [47], thermospray [56], solvent-assisted inlet ionization [60] and zero-volt paper spray [92], we have been able to develop a rough picture of the ionization process by deeply looking into several existing models, including electrical double layer [93], statistical charging [94], Coulomb fission [95], bag mechanism [96], ion evaporation [17], and charged residue model [16].

The charging mechanisms mentioned above can be divided into three categories according to their contributions to different phases of the gas-phase ion generation. The first phase is the initial formation of droplets, which are generated by directly

separating droplets from the bulk liquid sample. The initial droplets can be obtained from different sources, such as laser desorption, all kinds of nebulization techniques, heating, etc. The potential charging mechanisms that mainly contribute to these processes include models of statistical charging and electrical double layer. The second phase is the desolvation of initial droplets and secondary droplets formation, in which the droplet size eventually reaches $\sim$ 10 nm range or small enough, so that only one sample molecule is inside the droplet. Coulomb fission and bag mechanism models are regarded as the best candidates accounting for these processes. The third phase is the gaseous ions formation. Ion evaporation and charged residue models are the most prevailing models that can be responsible for these processes, depending on the molecule size.

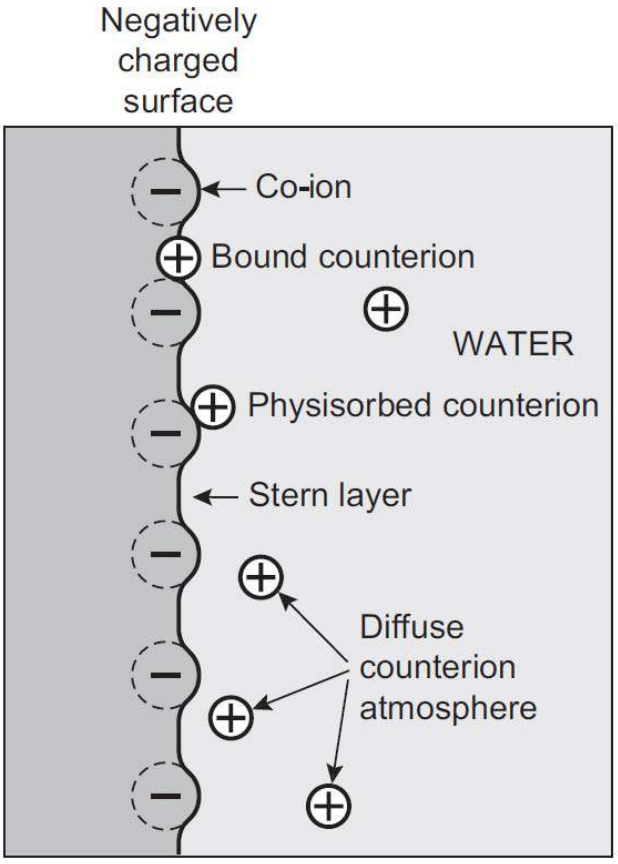

Figure 4.12: Schematic overview of electric double-layer model for a liquid. Figure copied from reference [93]

It should be pointed out that this categorization is not an absolute division of all the charging models. It only indicates the major ion formation mechanisms in each phase. It does not exclude the possibilities that certain charging mechanisms, such as statistical charging and Coulomb fission, can play important roles during the whole ion formation process. In this section, an overview is present on current models of charging mechanisms on different AP-MS techniques, which tentatively could be attributed to AP-DIVE-MS.

Electrical double-layer model [93]

At the surface of the bulk liquid, a layer of negatively charged ions is formed with positively charged ions underneath the water-air boundary. The thickness of this double layer is usually on the order of 10 nm. Figure 4.12 demonstrates the negative and positive ion distributions at the surface of water in the electric double-layer model and the different origins of positively charged counterions.

Statistical charging model [94]

The charge probability of a droplet is a net neutral Gaussian distribution, and the average absolute charge is given by:

$$\langle |q| \rangle = \left(\frac{4VN}{\pi}\right)^{\frac{1}{2}}$$

where V is the volume of the droplet and N is the concentration of dissociated molecules in solution. Therefore the average absolute charge in the droplet is proportional to the square root of ion concentration of the solution.

Coulomb fission model [95]

The primary highly charged droplets become unstable when the maximum amount of charge in the droplets reach the Rayleigh limit (electrostatic forces in the droplets exceed the surface tension). Then the primary droplets undergo breakup and a jet of fine secondary droplets are generated. After successive breakups, the solvent eventually evaporates and the analyte with residual charges remain.

Bag mechanism [96]

Figure 4.13 illustrates the aerodynamic breakup of a droplet in the bag mechanism. At low Weber numbers, the levitated droplets encounter the following process: (a) droplets flattening, (b) dimple forming, (c) bag forming, (d) annulus forming and bag enlarging, (e) bag breakup and a jet of fine droplets forming, (e) annulus breakup and large droplets forming. One potential possibility of bag breakup is also illustrated in the figure, where different charges carry different sizes of fragments. This also explains that in this model, there are <1% negatively charged droplets detected.

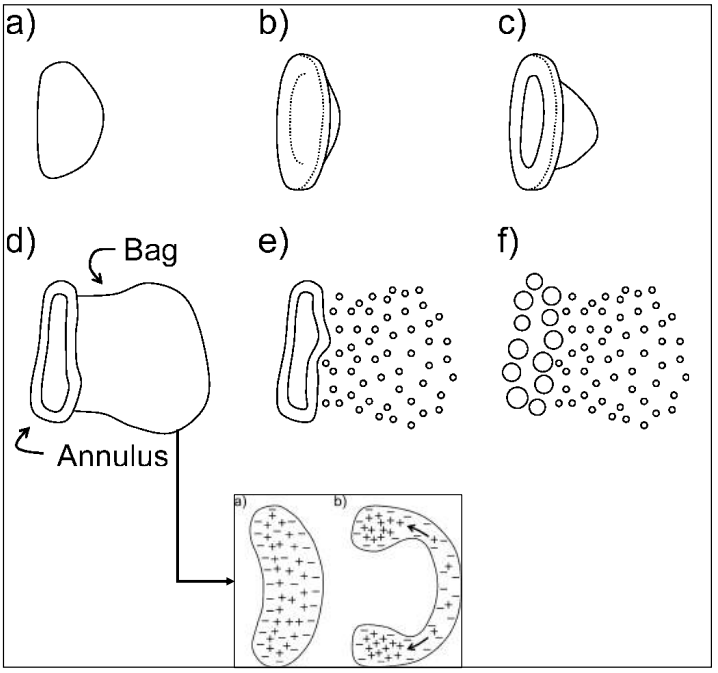

Figure 4.13: Aerodynamic process of the bag mechanism with its possible bag breakup principle. Figure copied and modified from [96].

Ion evaporation model [17]

Ions in an aqueous solution can escape from the surface when a strong electric field (10^5 V/m) is applied onto the surface of the liquid. Under the strong field, charged

droplets (10 to few tens of elementary charges) with radii of nanometers (<10 nm) evaporate from the liquid surface.

Charged residue model [16]

During desolvation process, droplets will repeatedly break up until there is only one macromolecule inside the droplets. Then further evaporation of the solvent from those droplets lead to the combination of charges originally from the surface to the macromolecule and thereby gas phase ion formation occurs.

4.3.2 Possible Charging Process for AP-DIVE-MS

For ionization of nonvolatile molecules, Vestal established a unified model which is consistent with the results and observations of AP-DIVE ionization [59]. In this model, the ion formation of aqueous samples can be generalized as a four-step process, which consists of the following steps: 1. energy deposition, 2. nucleation, 3. formation of droplets, and 4. production of molecular ions from droplets [59]. Based on this unified model, a possible charging process of PIRL will be discussed in this section.

As introduced in the previous chapters, laser desorption by PIRL works under the DIVE mechanism, in which impulsive optical energy deposition selectively excites the vibrational motions of the OH stretch, afterwards the energy is redistributed in the hydrogen bond network on an ultrashort time scale. The impulsive optical energy is most efficiently coupled to the phase transition of liquid water under superheating conditions, where homogeneous nucleation occurs, resulting in an intensive phase transition of water. Almost no energy can leak out of the excited volume as the pulse duration is shorter than the thermal and acoustic relaxation times of water. In addition, as the pulse duration is longer than the thermalization of individual OH stretch mode, multiphoton ionization and vibrational ladder climbing can be highly avoided by deliberately going to ps pulses to keep the peak power low enough to avoid multiphoton ionization. The dark field imaging shown in Figure 1.2 had

already demonstrated the temporal evolution and phases (gas, vapor/liquid, liquid) distribution of the PIRL ablation plume on different time scales. Compared to the primary plume, which consists of a considerable portion of gas and vapor, the secondary plume was attributed to the large ejection of sample material by large droplets formation, which are called 'recoil droplets'. The recoil droplets can be regarded as the initial droplets for the desolvation process and therefore contribute to the eventual gaseous ion formation.

In short, the role of PIRL on the gas-phase ion formation is as follows: 1. By impulsive energy deposition in liquid water, PIRL is coupled to the vibrational motion of OH stretch mode as energy pathway. 2. Homogeneous nucleation occurs via the impulsive heat by PIRL under superheating condition, resulting in an intensive phase transition and superheated droplets formation. 3. Droplets are formed by the secondary plume from PIRL ablation, which are regarded as the initial droplets and the start of the desolvation process. The gas-phase ions can be obtained from 'direct' and 'indirect' sources by PIRL. For the 'direct' source, gaseous ions are formed directly from the primary plume by PIRL desorption, which possibly represent the intrinsic ion states of molecular ions in aqueous solution. For the 'indirect' source, gaseous ions are formed via a desolvation process from the initial droplets in the secondary plume. As large amount of sample are ejected by the secondary plume and recoil droplets are formed, the 'indirect' source is postulated as the major source for the gas-phase ion formation. Its potential ionization method will be analyzed by comparing the experimental results based on the existing models mentioned above.

For PIRL ablation under the DIVE mechanism, it is a pure desorption process for water-rich samples. In addition, AP-DIVE-MS does not require applying any high voltage to the solution, or post-ionization. Then the question arises: what is the origin of ions for AP-DIVE-MS? As shown in Figure 4.14, the orientation of the PIRL ablation plume was bent when the capillary voltage (4500 V) was applied. Due to the polar nature of the water molecule, this observation itself is not sufficient to demonstrate that charged droplets have already formed at the PIRL ablation

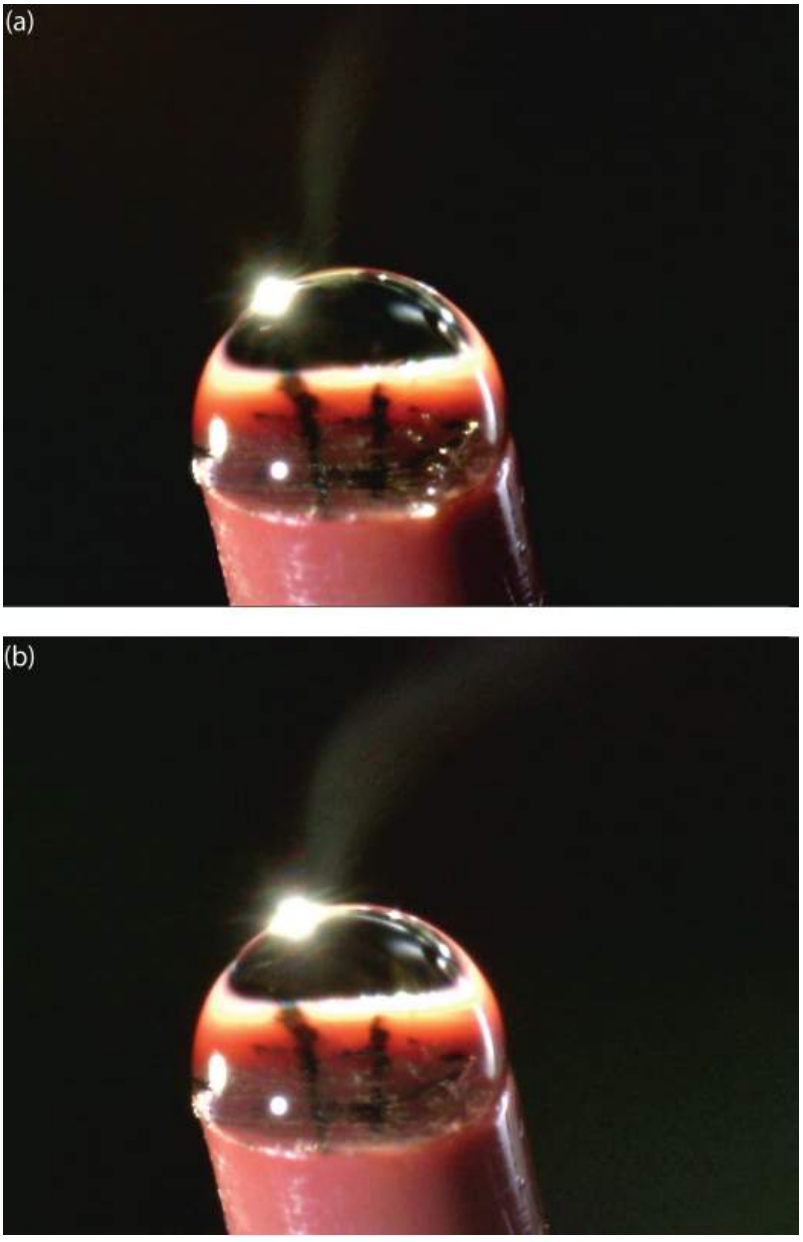

Figure 4.14: Plume orientation when high inlet capillary voltage (-4500 V) was off (a) and on (b).

site. A more careful examination of the difference between the two plumes in Figure 4.14 reveals that the cross section of the plume bound was expanded when the high voltage was on. A similar observation was reported in laser spray, where a high voltage applied to the sample led to an enlargement of the plume and finer charged droplets [40]. Although there is no direct high voltage applied in AP-DIVE-MS, the expansion of the plume, when the MS capillary voltage was on, indicates that charged droplets existed at the PIRL ablation site. And the expansion of the plume is due to the repulsion of charged droplets which carry the same type of net charges.

In other AP-MS techniques, such as the early versions of SSI, thermospray and SAII, similar interfaces without high-voltage or post-ionization were reported. 'Electrical double layer' and 'statistical charging' are often regarded as the candidates for the origin of charged droplet formation in these techniques. For the electrical double layer model, a layer of negative charged ions with positive ones underneath is formed at the water-air boundary. When a disruption happens at the interface, as the one in sonic spray, charged droplets are produced out of the bulk liquid. For statistical charging, as discussed earlier, the charge probability of droplets is a net neutral Gaussian distribution, and the average absolute charge is proportional to the ion concentration in the solution. The major difference between these two models is the droplet size. Due to the thickness of the electrical double layer ($\sim$10 nm), the diameter of droplets is usually on a nanometer scale. Micrometer-scale ($\sim \mu$m) charged droplets can not be produced in this model, since both positive and negative ions will be in the droplet and neutralize each other. In contrast, the diameter of charged droplets in statistical charging is usually in the micrometer range. From the dark field imaging of the DIVE ablation, a huge amount of microscopic recoil droplets in the secondary plume is produced, which, according to the scale bar indicated in Figure 4.14, are in the micrometer range [2]. Therefore the statistical charging model is more compatible with the experimental observation of DIVE ionization for the generation of initial charged droplets in the secondary plume.

After the primary droplet formation, a desolvation process is usually involved to

generate gaseous ions. 'Coulomb fission' is regarded as the major process for the breakup of droplets into finer ones for ESI. Meanwhile, another charge separation scheme called 'bag mechanism' was proposed to account for the desolvation of ESI and sonic spray. Furthermore, statistical charging is frequently discussed as a potential candidate for the charging mechanism for sonic spray. Among these three models, statistical charging tends to be a 'phenomenon', rather than a 'mechanism' for the charged droplets separation. It is the consequence resulting from droplets separating, not the reason why charged droplets can be separated. In addition, 'statistical charging' postulates that the charges, that can be produced by water droplets, are less than 5 charges/micrometer diameter, while the 'bag mechanism' can generate up to 100,000 charges/micrometer diameter [97]. Thus the latter is more suitable to explain the highly charged ions from clusters and proteins than the former. In short, 'Coumlomb fission' and 'bag mechanism' are the more reasonable candidates for the aerodynamics of droplets fission process in AP, as both try to explain the reasons and give scenarios on how the droplets are broken up. 'Statistical charging' is more attributed to the initial charged droplets formation.

As shown in Figure 4.15, an enhancement of the ion intensity by less than three orders of magnitude was observed for 10 μM myoglobin centered at +15 charging state, when the concentration of the ammonium acetate buffer was increased from 10 nM to 1 mM. A similar tendency was reported for sonic spray, where an ion intensity difference of three orders of magnitude was demonstrated when 0.01 M L-Serine was desolved in NaCl buffer with concentrations ranging from 100 nM to 1 mM [50]. The buffer dependence experiment in Figure 4.15 was carefully designed, as the isoelectric point of myoglobin is extremely close to 7 and the pH of ammonium acetate buffer is also supposed to be stabilized at 7. Consequently it was expected that there was no net charges on myoglobin in the solution. Highly charged ions of myoglobin, however, were observed with better S/N ratio and higher ion intensity when the buffer concentration was increased. This indicates that the myoglobin ion signal may come from different sources, such as superheated droplets, secondary recoil droplets, or condensed droplets that follow the plume front. Alternatively, it

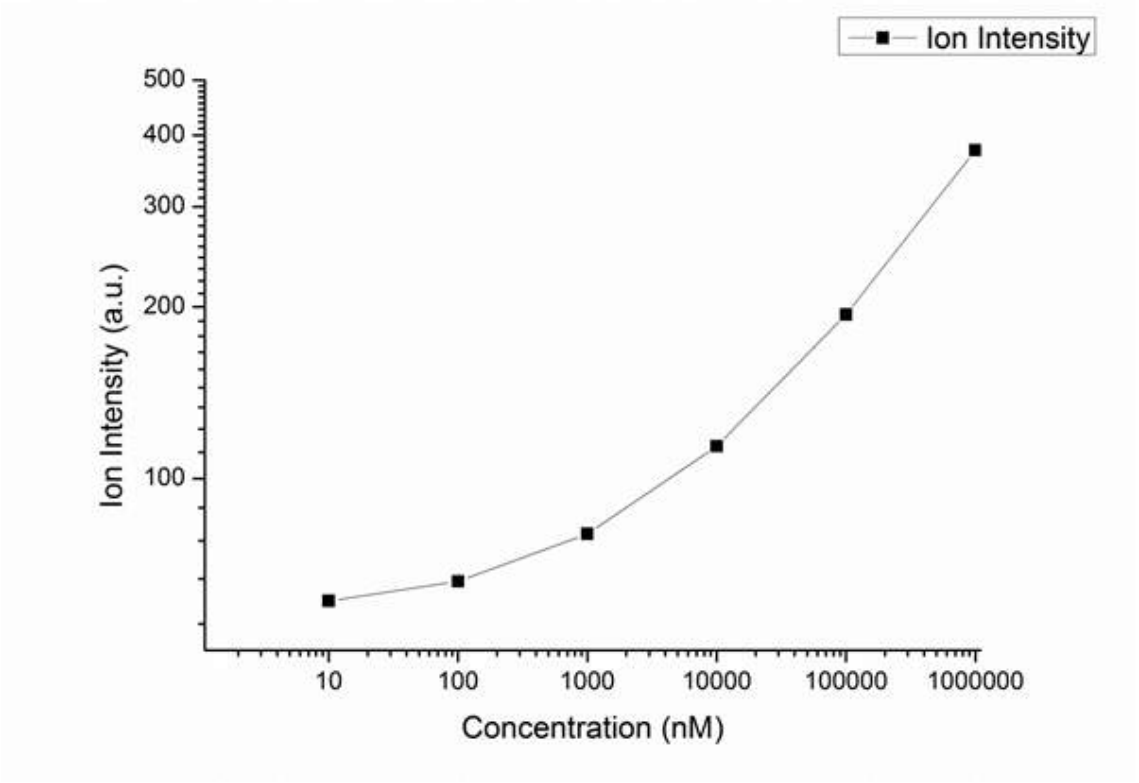

Figure 4.15: Ion intensity of +15 charged state of myoglobin versus ammonium acetate buffer concentration ranging from 10 nM to 1 mM. The gas diverting heated capillary extension was used. DIVE ablation was performed on 10 μM myoglobin in ammonium acetate buffer with flow rate 167 nl/min, shutter frequency 6 Hz, 4 pulse bursts, and an averaging time for each data point of 3 min.

may also originated from gas front of the PIRL ablation plume, where the counterions were separated from the bound ions of the native ion state of molecules in solution due to excessive engergy for dissociation [79].

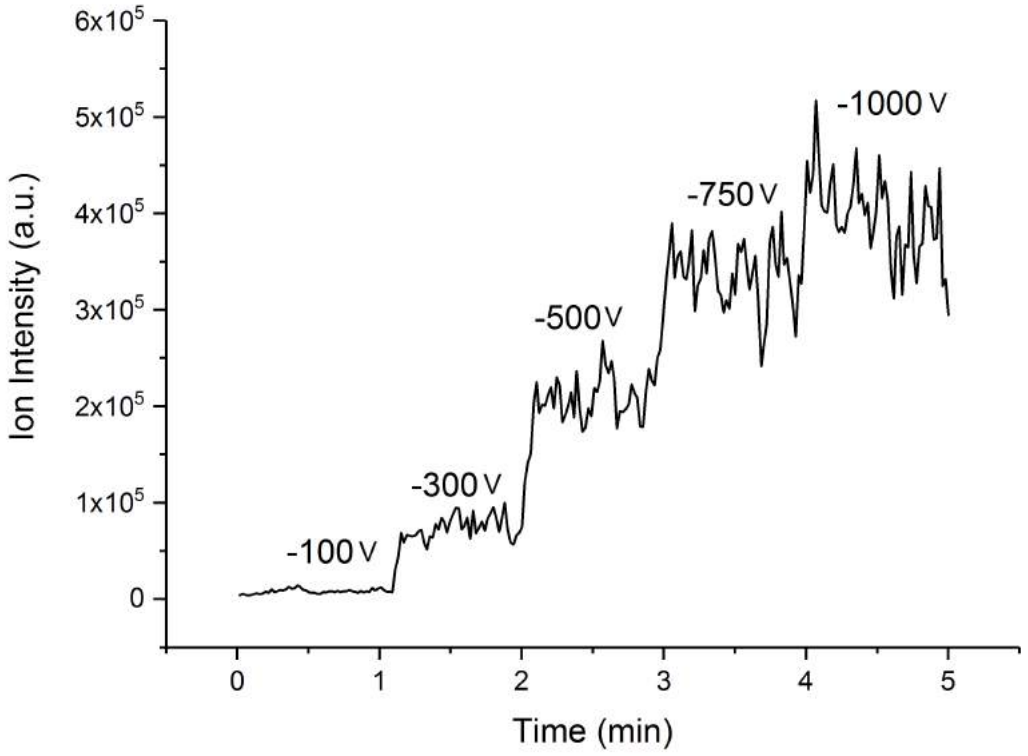

Figure 4.16: Temporal evolution of ion intensity with a step increase voltage applied on a metal mesh between the PIRL ablation site and the inlet of the MS. For each external voltage (as indicated), ion intensity over one minute was recorded and plotted. Sample: 10 μM angiotensin I in pure water. Figure taken from [82].

The other questions that are essential for the discussion of charging mechanism of AP-DIVE-MS are: Where are the ions formed? Are they formed in AP or in the MS inlet? In order to answer those questions, a metal mesh was implemented between the PIRL ablation site and the MS inlet. A voltage ranging from -100 to -1000 V was

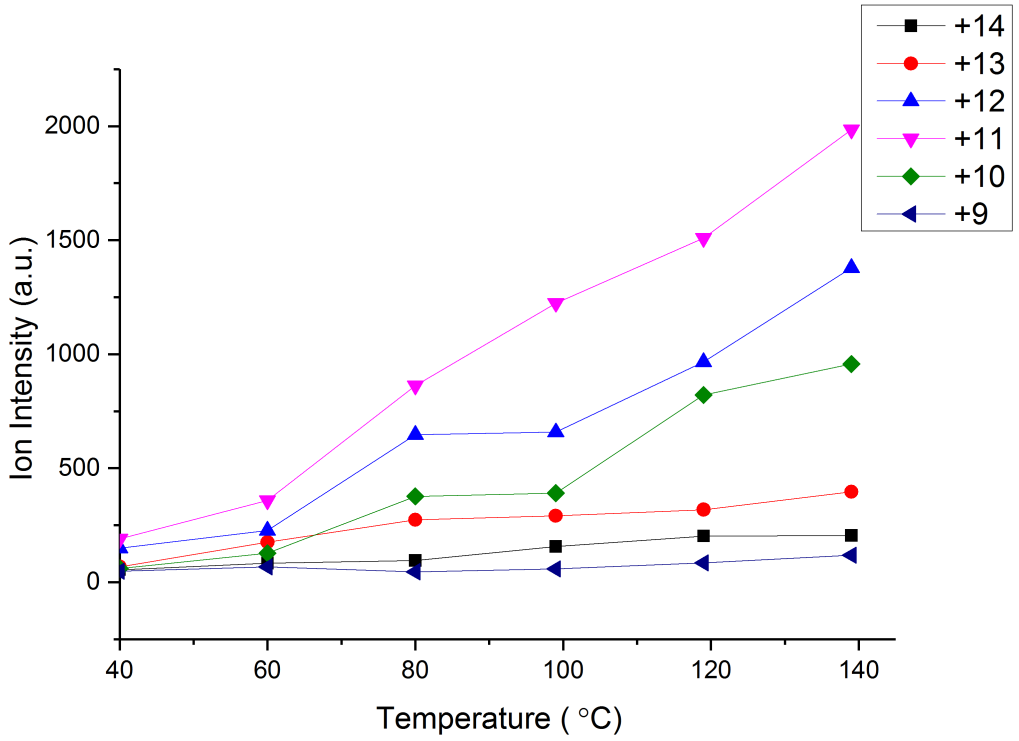

Figure 4.17: Ion intensities of multiply charged states (+9 to +14) of cytochrome c versus temperature (40 – 139 °C). The gas diverting heated capillary extension was used and allowed to establish thermal equilibrium before data collection. DIVE ablation was performed on 10 μM cytochrome c in pure water with flow rate 167 nl/min, shutter frequency 6 Hz, 4 pulse bursts, and an averaging time for each data point of 1 min.

applied to the metal mesh. When the external voltage was applied to the mesh, the inlet capillary voltage remained constant at -4500 V. As illustrated in Figure 4.16, the relationship between total ion intensity of 10 μM angiotensin I in pure water and the external voltage applied to the mesh was explored. The step rise tendency in Figure 4.16 shows that an increase of mesh voltage enhanced the total ion signal. In sonic spray, it was also reported that an obstruction helps to have more inclusive and selective ion signal, which was considerably improved by the obstruction [52]. This observation implied that the strengthened field in the path to the inlet of the MS helps to further extract and separate charged droplets from a bulk aqueous bead. And ion generation in AP-DIVE-MS is at least partially field induced. In addition, when a low voltage such as 100 V in Figure 4.16 was applied, an ion signal close to zero was observed, although the inlet capillary temperature remained constant during the experiment. This shows that an electric field plays an important role in AP-MS techniques: 1. It forms the field gradient to guide the charged droplets and ions into the MS inlet. 2. It facilitates charged droplet separation and ion evaporation. 3. It indicates that the charged droplets formation and even gas-phase ion generation in AP-DIVE-MS occur largely in AP before reaching the inlet of the MS. Moreover, it excludes the possiblity that inlet ionization alone plays a major role in DIVE-MS, as charged droplets most likely form in AP before entering the heated MS inlet and many results shown in thesis are performed under low heat transfer capillary temperatures (36–74 $^{\circ}$C).

As discussed above, it seems that the ion formation mainly occurs in AP. Yet we cannot exclude the possibility that the high temperature of the inlet capillary contributes to the final ion signal, such as in SAII and thermospray, which are usually regarded as inlet ionization techniques. Figure 4.17 demonstrates the ion intensity dependence on inlet temperature for all the charging states present in the mass spectra of 10 μM cytochrome c in pure water. An enhancement of the ion intensity for all charging states is observed, although the amplitudes of increase are different. Charged states, which are centered in the mass spectra of cytochrome c, such as 11+ and 12+, exhibit a more dramatic increase compared to other states. In ad-

dition, even at very low temperatures, such as 40-60 °C, the ion signal was already discernible in the mass spectra although the signal level was very low. Figure 4.17 demonstrates that the inlet capillary temperature does facilitate the enhancement of the ion signal. However, it is not the only factor that contributes to the ion signal formation in AP-DIVE-MS. 'Ion evaporation' and 'charged residue model' may also account for the gaseous ion generation, as the mass spectra from AP-DIVE-MS share a lot of similarities with ESI for the same sample.

In summary, it is clear that ion signal is enhanced by field-induced ion separation at the water/air surface, where PIRL ablation occurs. Yet for the final gaseous ion generation for AP-DIVE-MS, it seems that it is a collective process that at each phase a certain ion generation method is more dominant than the others. At the early stage, when the primary charged droplets are formed, statistical charging and field induced ion separation might be prevailing; during the desolvation in AP, bag mechanism and Coulomb fission are more convincing; and for the final gas-phase ion formation, ion evaporation and charged residue model tend to agree better with experimental results. In addition, gaseous ions can be possibly generated directly from counterion separation due to excessive energy for dissociation, according to Jing Zou's simulation [79]. Further experiments are required to provide more substantial experimental results studying the charging mechanism.

5. Matrix-Free PIRL Coupling of Lab-on-a-Chip Devices to AP-DIVE-MS

Contributions from co-workers to Chapter 5: Cornelius Louwrens Pieterse programmed the shutter control interface in LabVIEW. Wesley D. Robertson developed the image processing based fiducial algorithm. Candice Ip and Wesley D. Robertson developed the first version of the chip wetting and MS analytical setup. Dennis Eggert performed the confocal microscope imaging for the well wetting characterization.

5.1 Overview of Microfluidics and Lab-on-a-chip (LOC) Technique and its Applications

Microfluidics, by definition, are microsystems (usually tens to few hundreds of micrometers in dimension) that operate and manipulate a small volume (micro- to atto-liter) of liquids [98]. Targeted toward processing microfluids, the LOC is a revolutionary device in analytical chemistry and mass spectrometric analysis, as it minimizes the sample consumption, allows a better control of liquid concentrations and interactions, and shortens the time required for analyzing samples [99]. LOC-coupled MS has both unique advantages as well as challenges to the current MS techniques. One of the distinct advantages of LOC-coupled MS is that it is able to

operate and separate molecules in extremely low quantity or concentrations, which sheds light on the quantitative analysis towards single cell level [100]. And one of the biggest challenges is also caused by the low sample quantities, as it requires high sensitivity of the MS system and almost no sample loss between LOC and MS inlet.

Figure 5.1 illustrates two major types of LOC interfaces coupled to a MS inlet based on micro-scale ESI (upper block) or MALDI (lower block). According to the states of the microfluids, the LOC interfaces in Figure 5.1 can be further divided into analog microfluids (continuous flow), discrete microfluids (discrete droplets) and digital microfluids (the discrete droplets' wettability is manipulated by applying insulated electrode arrays) [101]. Compared to the conventional ESI or MALDI MS systems, the LOC-coupled MS interfaces dramatically downsizes the scale of sample consumption volume, shortens the complete analytical time, reduces the system complexities while maintaining or even increasing sensitivity, and have much more precise control of individual droplet size in digital microfluids [101, 102]. For example, a droplet-based LOC coupled ESI interface was reported for the nanoliter-scale organic synthesis (aminocatalyzed domino reaction) with catalyst in low picomole quantity [103]. An automated droplet microfluidic interface, which is then coupled to MALDI has shown a 30-fold enhancement of ion intensity due to an increase of homogeneity of a dried sample deposited on a MALDI plate and an improvement of sensitivity down to few tens of attomoles [104].

Due to the extremely small scale of sample consumption and short analytical time, as well as the precise control of sample volume in LOC systems, there are numerous promising applications for biomedical purposes [105]. A scenario of a complete microsystem for cell studies, which includes tissue organization, cell selection and cell imaging has been constructed, which might revolutionize biological studies on a cellular level [106]. The ultimate goal of DIVE-MS is to explore the constitution and chemical reaction inside cells. Therefore a novel self-localized megapixel picoliter chip has been developed in our group. A first attempt to construct an interface to directly couple the sample loaded onto the chip to the MS inlet has been made,

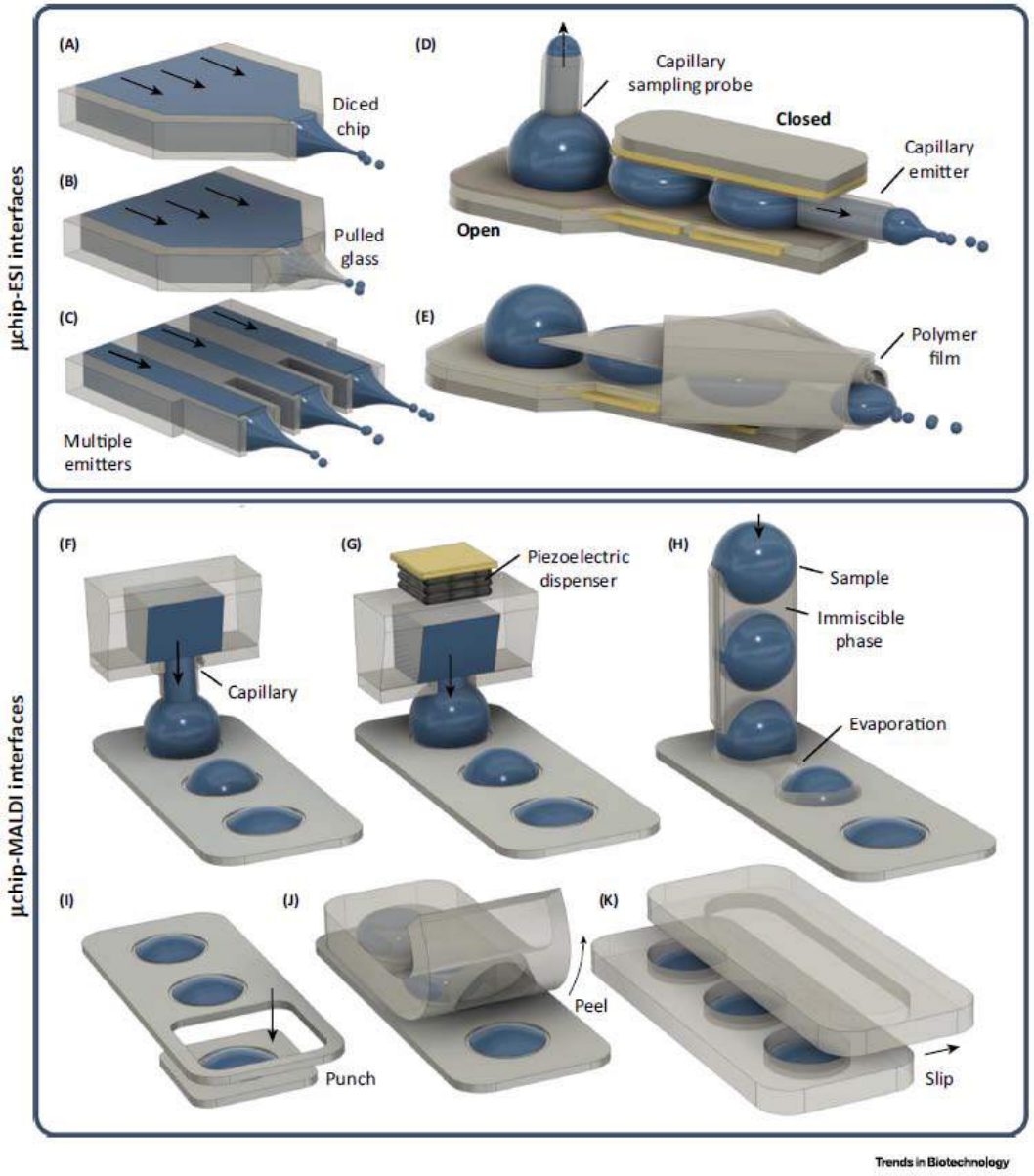

Figure 5.1: LOC interfaces coupled to MS. The upper block presents ESI-based interfaces, the schemes in the lower block are based on the MALDI technique. Figure taken from [101].

and the preliminary results will be presented and discussed in this chapter.

5.2 Instrumentation

5.2.1 Wetting Method for Megapixel Picoliter Chip

The design of the self-localizing picoliter arrays on the optical transparent silicon chip was originally designed and fabricated by Arash Zarrine-Afsar from our group [107]. The chip was fabricated by using a double-side polished fused silica wafer (500 μm thick) with a layer of silicon nitride (300 nm thick) coating deposited on one side of the wafer by plasma-enhanced chemical vapor deposition (PECVD). The megapixel arrays were first patterned on a mask and then transferred onto the silicon nitride side of the wafer by standard UV lithography. Reactive ion etching with SF_6 and O_2 was used to etch the surface of the chip until the silicon nitride coating was completely removed inside each picoliter well. Therefore each picoliter well in the array consists of a well wall of silicon nitride and a well bottom of silicon. A diamond dicer was used to cut each chip into a 15 $\times$ 15 mm^2 square. The basic parameters of the megapixel picoliter chip for the experiment are listed in Table 5.1.

The wetting of the wells was characterized by confocal laser scanning microscopy, and the profile is illustrated in Figure 5.2. The wetting protocol was developed based on Arash Zarrine Afsar's original design of a saturated microenvironment in an enclosed chamber, and the detailed procedure is as follows: the picoliter chip is first cooled down to 4 °C and then wetted with aqueous solution containing 0.02 % (w/v) FITC-Dextran (Sigma-Adrich Chemie GmbH). Directly after wetting, the chip is transferred to an enclosed chamber (glass bottom culture dish, P35G-1.5-10-C, MatTek Corporation), in which the water vapor is saturated. Due to the saturation microenvironment in the chamber, the chip is able to remain wetted for over 30 minutes, which allows the imaging by confocal microscopy for characterization [107]. A confocal laser scanning microscope (C2+, Nikon GmbH) equipped with a 20× objective (CFI Plan Appo Lambda 20× /0.75, Nikon GmbH) was used

Table 5.1: Basic parameters of the picoliter chip used for experiment.

Chip dimension	Chip transmission	Well distance	Well diameter	Well depth
15 × 15 mm^2	around 80 % to PIRL	300 μm	100 μm	300 nm

for 3D imaging with a 488 nm diode-pumped solid-state laser (Melles Griot GmbH) for exciting FITC-Dextran. The excitation light was filtered from the emission light by applying a 405/488/543/640 beam splitter (Nikon GmbH) with a 515/30 band-pass emission filter (Nikon GmbH). Fluorescent-labeled latex beads (0.1 and 1.0 μm FluoSpheres Carboxylate-modified microspheres, yellow-green fluorescent 505/515, Thermo Fisher Scientific Inc.) were used to correct spherical aberrations by being imaged under the same conditions.

In order to estimate the liquid volume loaded into each well, water volume in 25 wells were measured using the 'surface' function of the Bitplane Imaris software (v.8.2.1, Bitplane AG). As demonstrated in Figure 5.2, the liquid profile was obtained by confocal microscopy in an enclosed saturated chamber at 4 °C, which could avoid evaporation of the liquid from the well. In Arash Zarrine-Afsar 's paper, it was demonstrated that a highly convex meniscus liquid in the well can be obtained with an aspect ratio (well diameter/well height) larger than 100. The aspect ratio of 333 for the wells in Figure 5.2 results in a localized volume of water with central thicknesss of 2.1 μm and 0.35 μm at the edge. The total localized volume was measured and averaged as 9.5 pl per well.

The wetting of the well is automated by wiping a drop of liquid over the chip surface, and the liquid is self-localized into each well. During the wetting process, surface roughness, or more precisely, the surface roughness gradient plays an important role. The surface roughness of the chip is illustrated in Figure 5.3B, the top surface and the bottom surface of the well share similar roughness, as they are exposed to the same ion etching process. Since the side wall of the well exhibits much smoother surface roughness, a surface roughness gradient is formed in the following sequence: rough well top surface – smooth side wall surface – rough well bottom surface. In

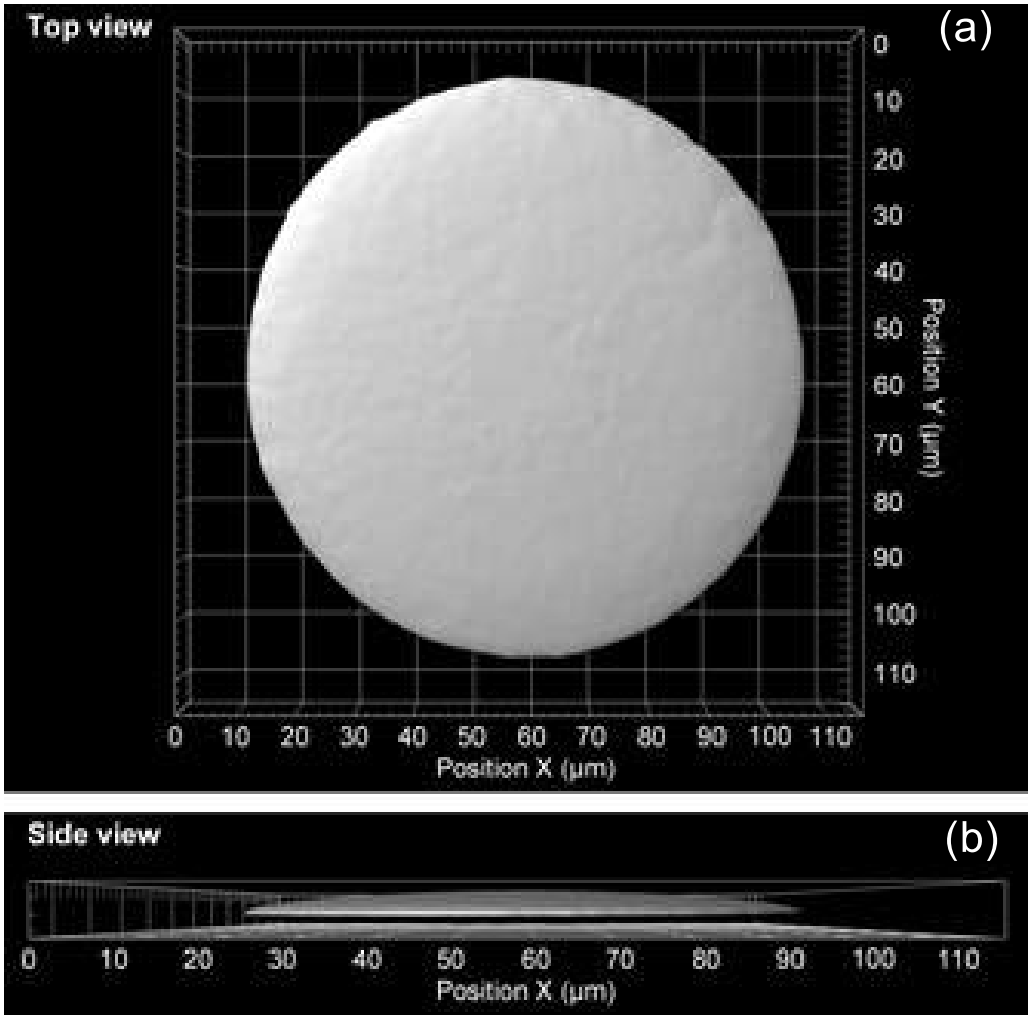

Figure 5.2: Liquid profile obtained by confocal microscopy of an individual microwell. The image was collected following well loading with aqueous solution inside a humidified and temperature-controlled ($\sim$ 4 °C) chamber.

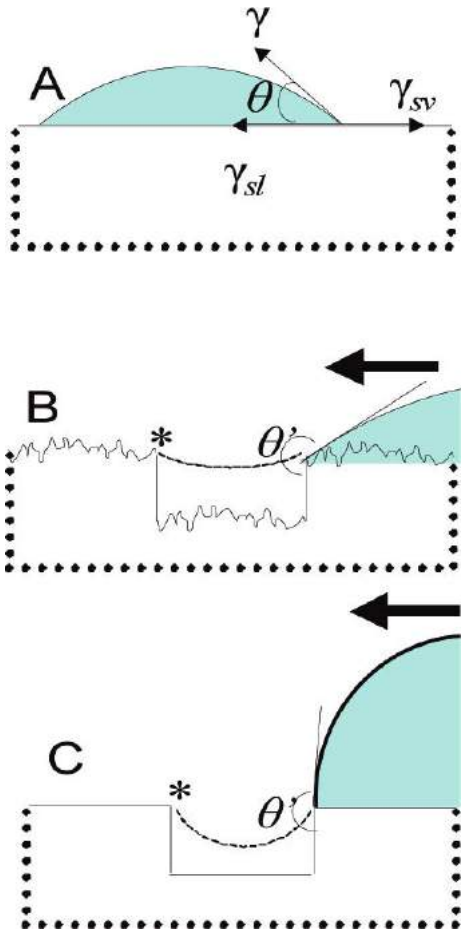

Figure 5.3: Liquid contact angle θ to the surface (A) and its dependence on different surface roughnesses (B) and (C). Figure copied from [107].

Figure 5.3B and C, the movement of the liquid bead makes the contact line (γ in Figure 5.3A) instable, which results in the 'dynamic wetting' of liquid into the well. Compared to the smooth surface in Figure 5.3C, the surface potential energy in 5.3B is much more reduced due to the bigger change in contact line, which facilitates the film capture into the well. Moreover, the rough bottom of the surface in 5.3B helps further pinning liquid into the well.

5.2.2 Experimental Setup

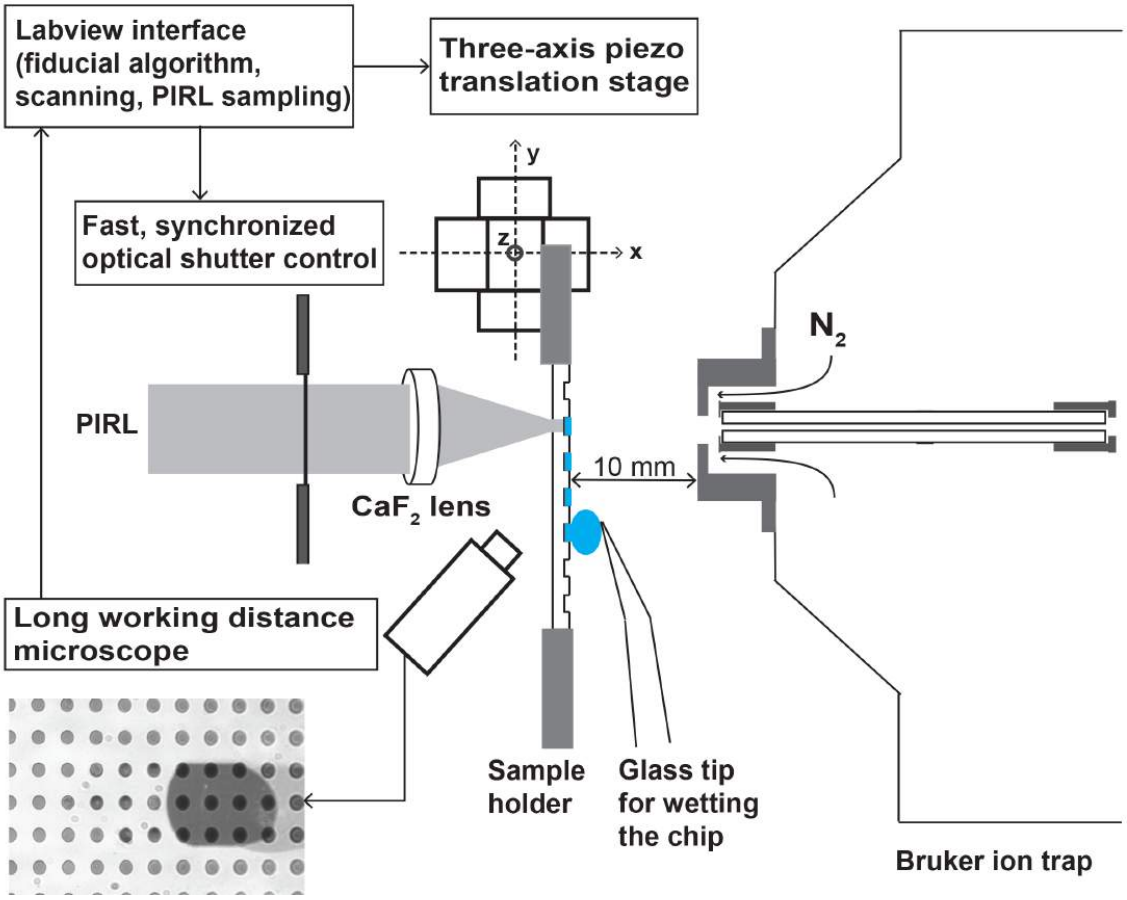

Figure 5.4: Schematic representation of AP-DIVE coupled LOC system.

The AP-DIVE coupled LOC system is illustrated in Figure 5.4, which mainly consists

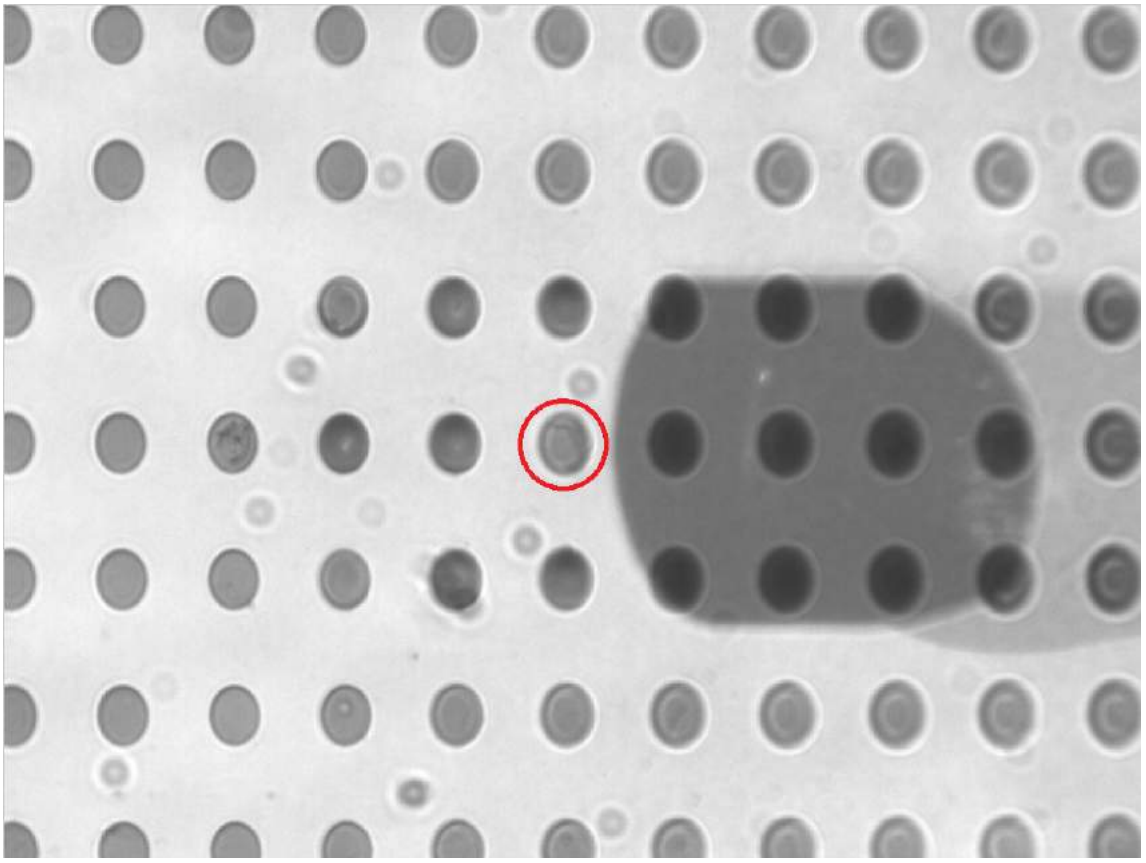

Figure 5.5: Image of the chip wetting in the experiment. The well marked with red circle in the figure is the site where PIRL ablation occurred.

of a chip mounting, imaging (using a long working distance microscope, QI-OPTIQ) and loading interface, a mechanical slip-stick translation stage (SLC-2445, SmarAct) with a closed-loop positioning sensor (±1 nm precision), a focused PIRL, a synchronization unit controlled by a home-programmed LabVIEW interface, and a Bruker ion trap MS. The working procedure of AP-DIVE coupled LOC-MS is as follows: the chip is mounted onto the chip mount, which is fixed to the three-axis piezo translation stage. Based on the contrast formed by the different reflectivity between well bottom and top surface, an image of the chip can be obtained by using a long working distance microscope, as presented in Figure 5.5. The image of the chip is analyzed and processed by the fiducial auto-alignment algorithm developed by Wesley D. Robertson et al. [108]. Under this algorithm, in total three wells are selected, in which two are in the same row and two are in the same column, and the whole scanning area is thereby defined. After well selection, the algorithm processes and calculates the coordinates for the center of each well in the scanning region and gives the feedback to the LabVIEW interface. The LabVIEW interface, which synchronizes the optical shutter of PIRL and the translation stage for the chip, is then used to control the translation stage to the first aligned well. A glass tip with loaded sample bead is positioned and loosely attached to the first well, which is monitored under another microscope (not shown in Figure 5.4). After finishing the sample loading, the LabVIEW interface controls the translation stage to operate a chip scan along the path formed by the fiducial algorithm. Meanwhile, the synchronized shutter follows the commands from the LabVIEW interface to either open allowing the whole row scan or only a certain well for single well analysis. No matter in which mode, the sample loaded in the well is ablated by PIRL focused to the back side of the chip when the well is exposed during an opened shutter and at the position coaxial to the MS inlet. Figure 5.5 presents a chip image under microscope, the large shadow in the image is the sample bead loaded on the glass tip, which remains stationary when the chip moves via the translation stage. The bead is therefore transferred into wells by this relative movement. When the well arrives at the position axial to the MS inlet, the LabVIEW synchronization unit sends the

shutter a command for opening, which allows PIRL ablation to the well. Comparing the grey scale to the surrounding wetted wells, the center well in Figure 5.5 was just ablated completely by PIRL.

5.3 Results and Discussions

5.3.1 Single Row Scan

In order to demonstrate the functionality of the AP-DIVE coupled LOC MS, a single row scan was performed to optimize the system using diluted Agilent G2431a Tuning mix (G2431a:water= 1:20, v/v). The results of a single row scan is displayed in Figure 5.6 with ion intensity response in (a) and the mass spectrum averaged within the full scanning time in (b). A relatively narrow m/z range between 500 – 700 was set to include only the hexakis(2,2-Difluoroethoxy) phosphazene, so that ion competition can be greatly avoided. And the mass spectrum of the protonated species (m/z=622) is presented by averaging over the entire scanning time. It should be noted that for the total ion intensity response shown in (a), the zero ion intensity regime between two non-zero ones are due to the z-shape scan path of the chip, and only the odd lines can generate ion signals. The ion signal variation among different rows are possibly caused by several factors: 1. As the contact line angle changes when the size of the sample bead shrinks during the wetting process, it is likely that the wetting conditions are not optimal when the beads become smaller. 2. Misalignment of the ablation plume to the MS inlet may exist, as the movement of the chip adds instability to the dynamics of the plume during a chip scan. In addition, for the ion signal within one row, there is always a major peak which includes several minor peaks, which is most probably from the incompletely resolved ion signal of each well in the row due to the difference between the accumulation time of the ion trap and the high speed of the translation stage.

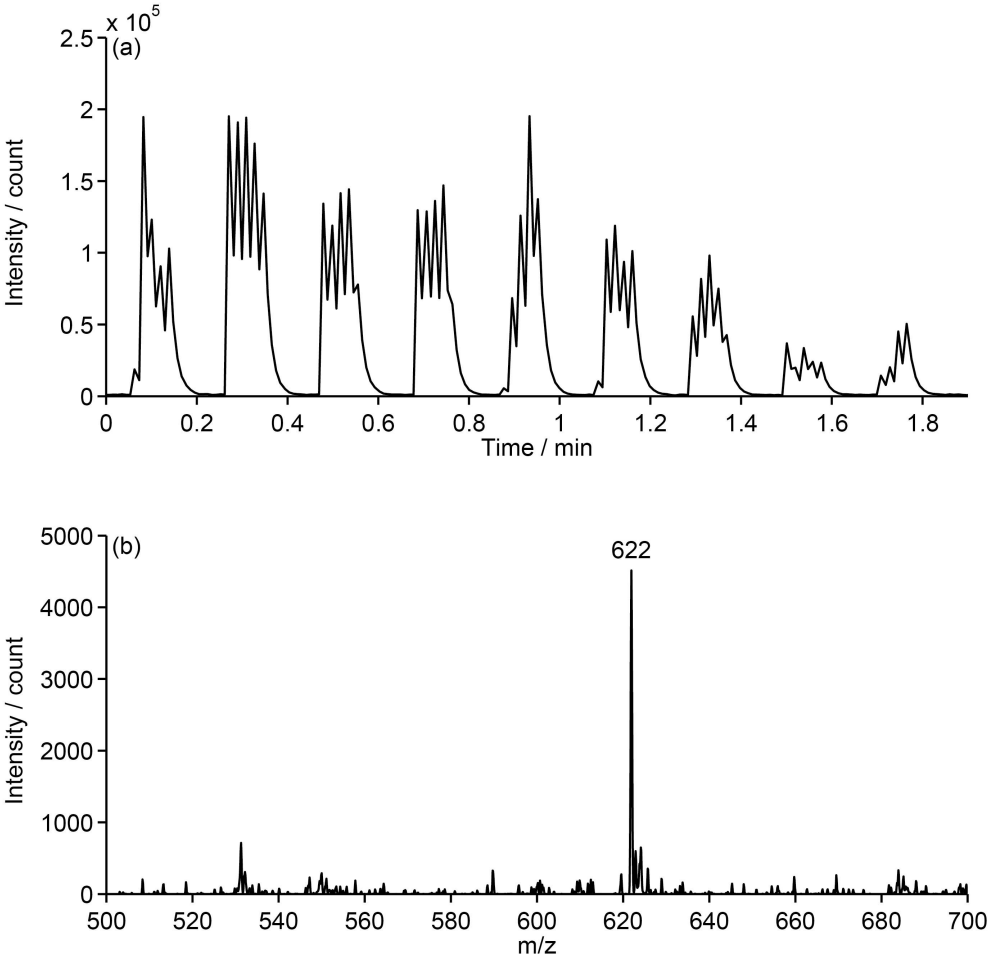

Figure 5.6: (a) Total ion current (TIC) of phosphazene compound (500 – 700 m/z) illustrating each row of the array. Due to the array scan path, every second row contributes to a peak of TIC. (b) The averaged PIRL-DIVE mass spectrum showing the protonated species of hexakis(2,2-difluoroethoxy) phosphazene.

5.3.2 Single Well Scan

The ultimate goal of using megapixel arrays is to analyze samples loaded into each isolated microwell. In order to achieve such a goal, the ion response from a single well was explored. The shutter was monitored to only open when the central well in each scanned row reached the position coaxial to the center of MS inlet. As the localized volume in each well can be measured and estimated by laser scanning confocal microscopy, the exact number of molecules in each well can be calculated when the concentration of the aqueous sample is known. Moreover, since the localized volume of liquid is on the few picoliter scale, which is usually much smaller than single pulse ablation to aqueous samples, the sensitivity of the LOC MS system is expected to be very high due to the low sample volume consumption.

In Figure 5.7(a), ion signals from single well response were demonstrated, in which peaks a – j correspond to the TIC of a single well each for a 24-row chip scan. The distance between two adjacent peaks along the 'time' axis were the same, suggesting that the optical shutter opened to the wells in the same column in the scanning area. In addition, it should be pointed out that not every well in the same column showed the ion signal. And ion signals from two wells were missing in Figure 5.7(a). This may come from the unsuccessful dynamic wetting of these wells, or fluctuations of laser fluence. However, as presented in Figure 5.7(b), even in the single well response with lowest TIC (peak h in Figure 5.7(a)), the corresponding averaged mass spectrum, which again isolates m/z range for hexakis(2,2-Difluoroethoxy) phosphazene from G2431a, was easily discernible. Moreover, Figure 5.8 demonstrates the averaged mass spectra of each TIC peak in single well response shown in Figure 5.7(a). It shows that all the mass spectra present the characteristic protonated spectra of the molecule. Although the absolute intensities of the spectra vary due to the TIC fluctuations, all the mass spectra exhibited extremely good S/N ratio, which indicates the successful acquisition of signal from isolated single well response from the megapixel arrays.

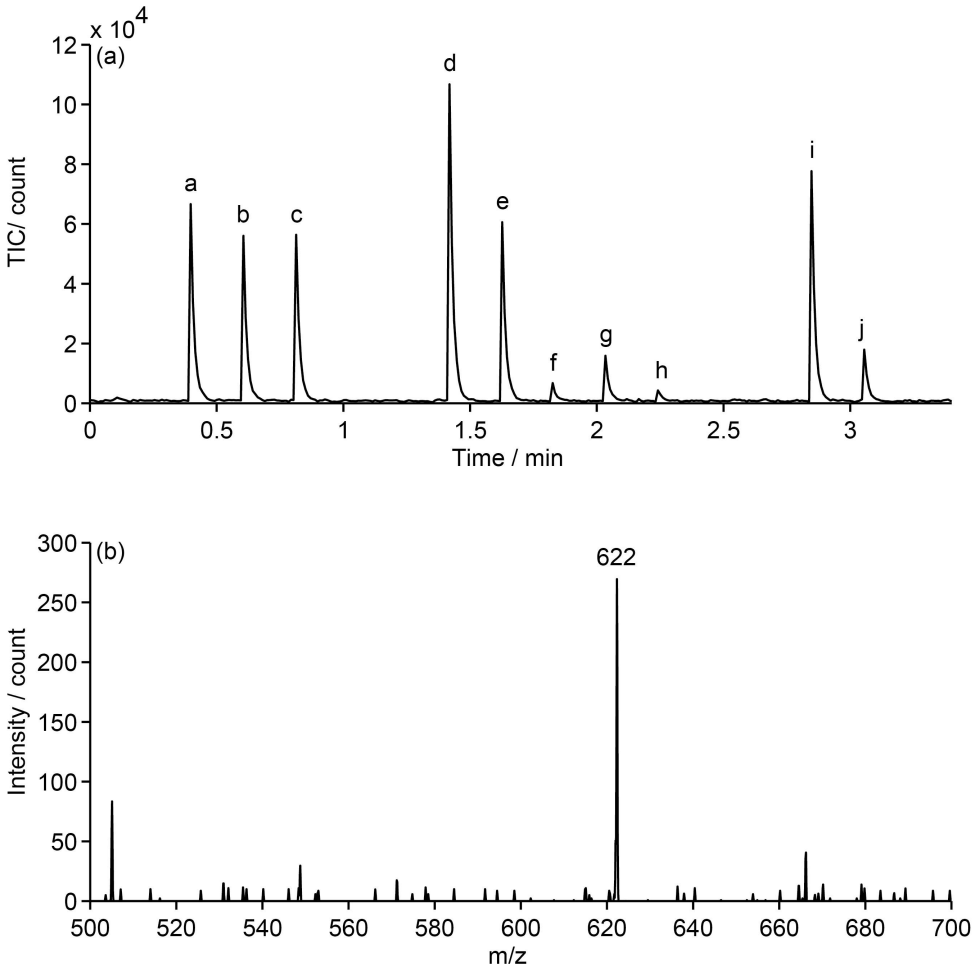

Figure 5.7: (a) The total ion current of an aqueous solution of hexakis(2,2-difluoroethoxy) phosphazene scanned and loaded into the array with only a single well sampled from each row. (b) The PIRL-DIVE mass spectrum averaged form peak h in Figure 5.7(a).

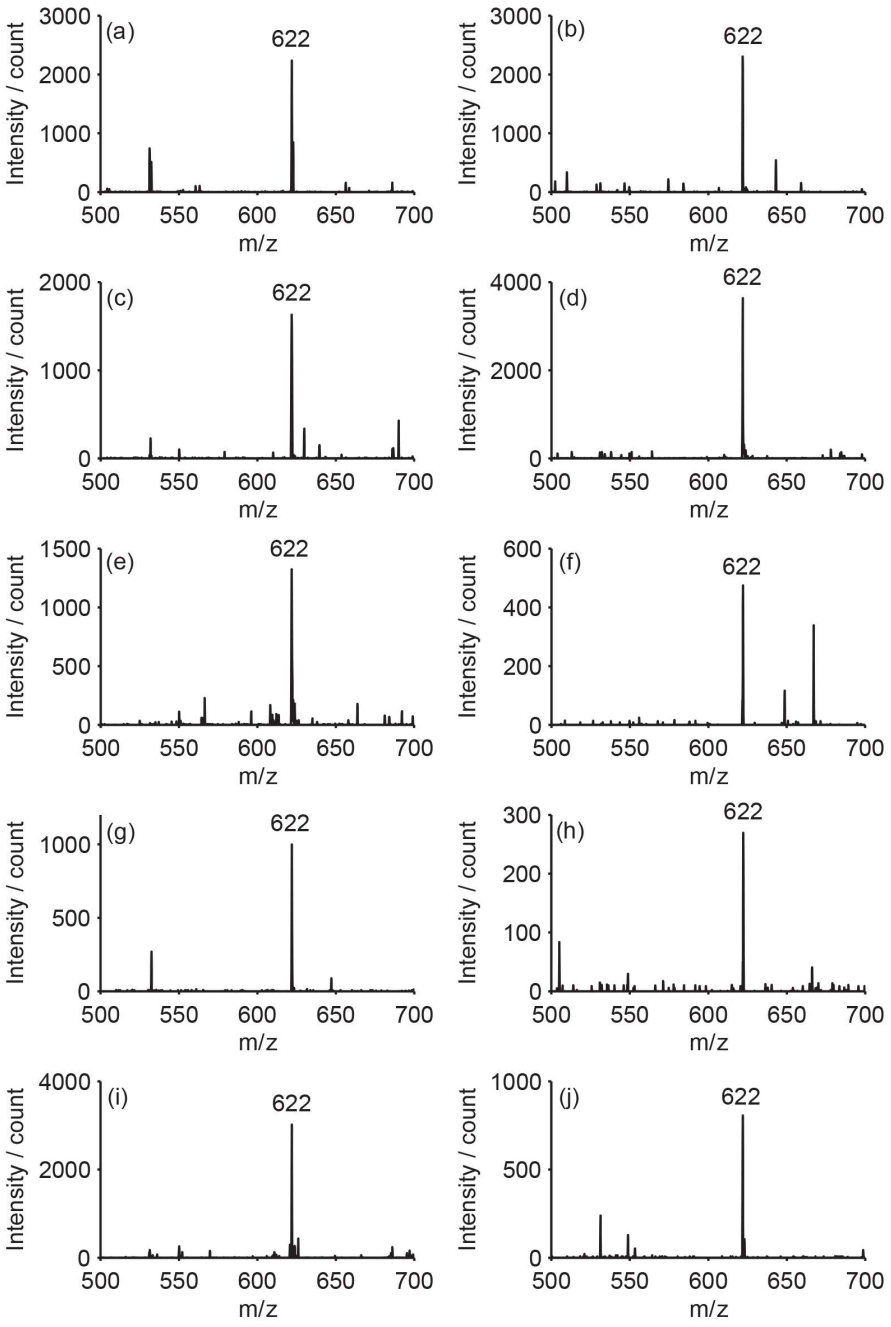

Figure 5.8: The PIRL-DIVE mass spectrum averaged from 5.7(a), showing the protonated species of hexakis(2,2-difluoroethoxy) phosphazene.

5.3.3 Peptides

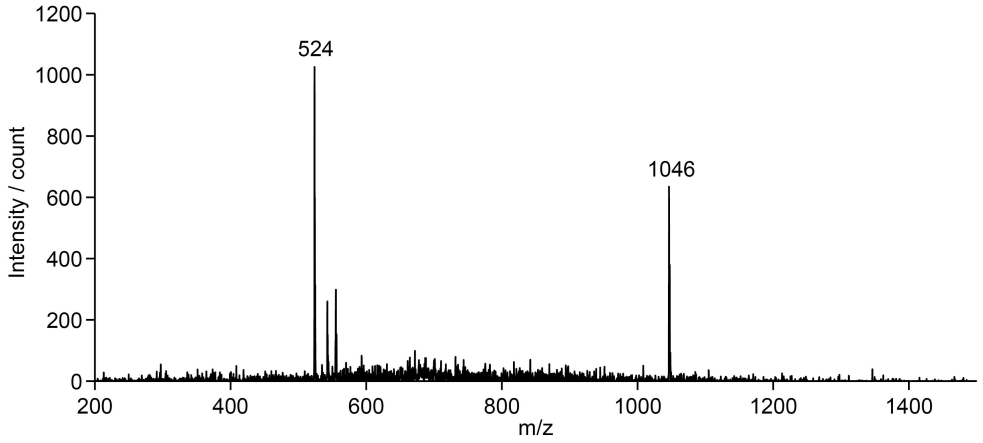

Figure 5.9: Mass spectrum of 1 μM angiotensin II in water with 0.05% acetic acid using chip scanning.

One of the major applications of the megapixel chip is to analyze biomedical samples in a fast, highly sensitive, and low sample consumption manner. Therefore it is of great importance to test whether the system can produce mass spectra from a biological sample. As shown in Figure 5.9, a sample solution of 10 μM of angiotensin II in water with 0.05% acetic acid was applied to the AP-DIVE LOC MS system for single row scan. Singly and doubly charged states of angiotensin II were successfully obtained by averaging the TIC over the complete scanning time. However, unlike the single row or single well responses from G2431a tuning mix shown above, in which each TIC peak contributes to the mass spectra of the sample molecule, only the first two peaks of TIC accounted for the mass spectrum of angiotensin II, while the remaining peaks contributed only noise. The same experiments were repeated several times, yet similar results were obtained. The possible reason resulting in this observation needs to be further explored by using different peptides or protein samples.

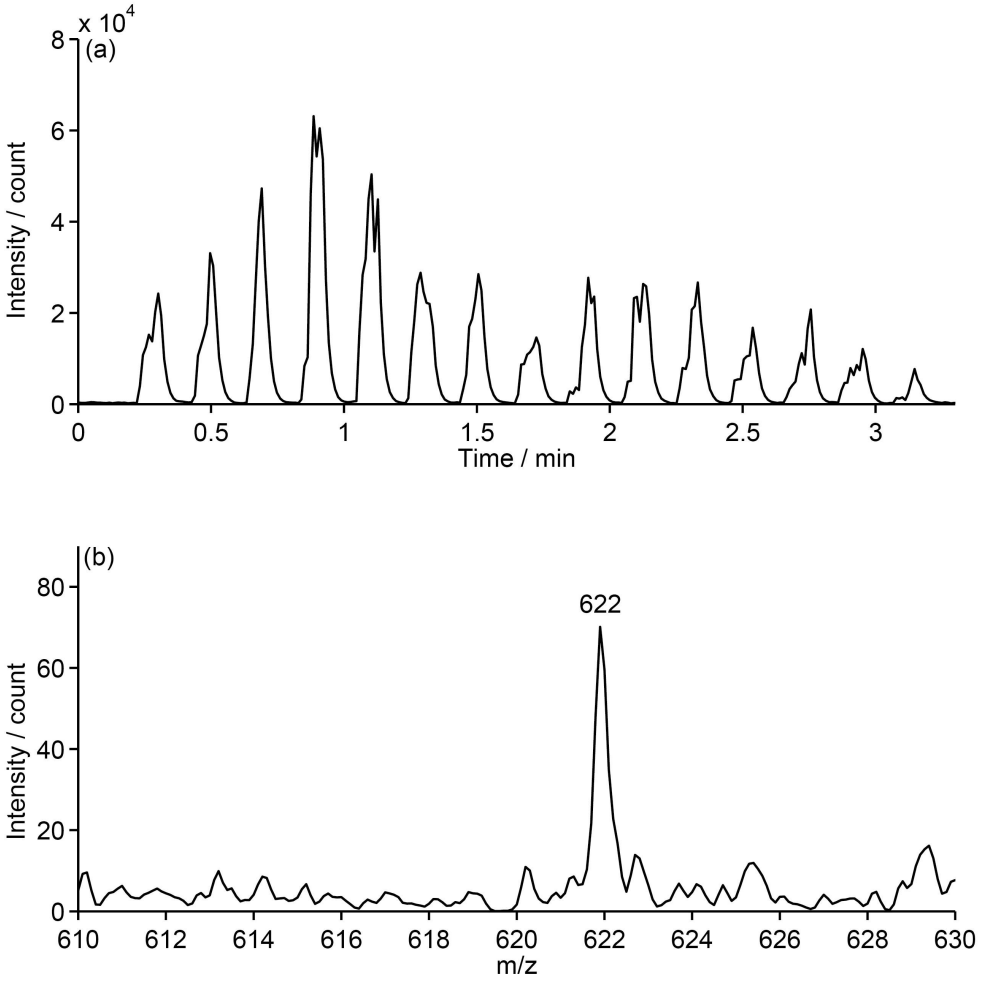

Figure 5.10: The PIRL-DIVE mass spectrum corresponding to 30 femtomoles of hexakis(2,2-difluoroethoxy) phosphazene of sample loaded and sampled directly from the aqueous self-sorting microwell array. (a) TIC of the complete chip scan. (b) The corresponding averaged spectrum for the complete scanning time in (a).

5.3.4 Sensitivity

The sensitivity of the AP-DIVE LOC MS was evaluated by using 150 nM hexakis(2,2-difluoroethoxy) phosphazene from a diluted G2431a tuning mix. A sample bead with 200 nl volume was loaded on the chip for single row scan. The TIC peak corresponds to the ion signal from each single row scan as shown in Figure 5.10(a), and the mass spectrum obtained by averaging the complete scanning time is presented in Figure 5.10(b). The 29.9 nM sample concentration with 200 nl volume resulted in a total consumption of $\sim$ 6 femtomoles of analyte. Note that 6 femtomoles is only a rough estimate of the sensitivity of the system, as only half of the rows in the scanning area contributed to the ion signal. A more accurate estimate of the sensitivity would be to get the ion signal from a single well with low concentration of analyte, which will be examined more carefully in future experiments.

5.4 Summary

To summarize this chapter, a LOC interface, that couples the self-localized picoliter chip directly to the MS inlet, was constructed and its functionality demonstrated in first experiments. The MS signals from single row and single well scans were obtained. The single well scan showed the acuity of the system to respond to a localized low picoliter volume sample. The current system sensitivity at the low femtomole level has a considerable potential to be improved by modifying the complete interface into a more quantitative one. The interface needs to be adapted such that different types of biological samples can be loaded into and studied by this system.

6. Summary and Outlook

In this PhD thesis, an experimental apparatus to directly couple a picosecond infrared laser (PIRL) to a Bruker ion trap mass spectrometer (MS) has been demonstrated in order to investigate the interaction of PIRL with biomedical samples. PIRL ablation on bio-samples works under the mechanism of desorption by impulsive vibrational excitation (DIVE), which has been theoretically and experimentally studied previously by Prof. R.J. Dwayne Miller's group. As demonstrated in this thesis, PIRL ablation to water-rich samples is considered to be 'soft' due to both the thermal and acoustic confinement inside the ablated volume as well as absence of multi-photon ionization. Therefore it is of great interest to investigate the characteristics (such as charging state, fragments, structure, etc.) of all types of small molecules, peptides and proteins inside the plume immediately after PIRL ablation by means of mass spectrometric analysis, which is able to investigate both the chemical and structural features of the analytes.

In order to achieve this goal, an atmospheric pressure desorption by impulsive vibrational excitation mass spectrometric (AP-DIVE-MS) interface with continuous sample supply has been constructed and demonstrated to achieve online analysis of analytes in aqueous solution ablated by PIRL. The interface developed here is the first one that directly couples PIRL to a MS inlet without the need of utilizing any post-ionization source or nebulizer under atmospheric pressure condition. Characterization of the interface was performed. Long stability of the total ion current over 30 min was demonstrated. A mass spectrum from single pulse ablation of a

27 picoliter volume of analyte solution was presented. The limit of detection of 10 nM, which corresponds to 39 amol of sample, was demonstrated. In addition, MS analysis of small molecules, molecular mixtures, peptides and proteins in both pure water and acetic water solutions was performed, where no fragments were found in the mass spectra. Moreover, nearly native mass spectra of proteins in buffer solutions were obtained, substantiating the softness of PIRL ablation. Compared to infrared matrix-assisted laser desorption/ionization (IR-MALDI) with water or ice as matrices, AP-DIVE yields much higher charging states, which is comparable to ESI. Yet the fact, that no nebulizer or high voltage need to be directly applied to the solution, indicates a possibly different charging mechanism from ESI. Consequently, the charging mechanism of AP-DIVE-MS has been discussed in this thesis, which tends to attribute the highly charging states to a combination of direct gas phase and droplets desolvation in the ablated plume. For the AP-DIVE-MS with continuous sample delivery, further experiments need to be performed to investigate the charging mechanism. And more MS studies on native protein and protein complexes are necessary and important for the ultimate goal of applying PIRL for cell mapping.

The other main application of AP-DIVE-MS demonstrated in this thesis is a lab-on-a-chip (LOC) interface, where low picoliter volume of aqueous sample can be localized inside a megapixel chip array and back-ablated by PIRL for further MS analysis. By applying a fiducial algorithm developed for this interface, automation of chip alignment was achieved and then synchronized with the laser shutter control. Signals from single-row scans were presented and the upper limit of sensitivity of 30 femtomole was estimated by the concentration and the initial volume of the sample before scanning starts. In addition, a MS signal from single-well response was successfully demonstrated, which shows the extreme sensitivity of the interface. Moreover, preliminary results of mass spectra from protein solution were demonstrated and current challenges have been discussed. Current results presented in this thesis show the promising future of this LOC interface. For example, by changing the aspect ratio of the current chip, the sample volume of each well can be further reduced. By lowering the concentration of solution for a single-well scan, sensitivity

of the system can be dramatically increased. By using the newly developed wetting tip with continuous sample supply, sample loading and consumption can be much more precisely quantified. By changing the material of the sample mount, the potential field issue in the system is expected to be solved, and better protein response and mass spectra can be obtained. By modifying the sample holder with a cold finger, a cryo-cooling chip system in atmosphere can be established for MS imaging. And a quick blood test device can be developed by either directly loading blood onto the chip, or by re-hydrating the dried blood on the chip with the wetting tip in the system.

To summarize, the development of AP-DIVE-MS interfaces introduced in this doctoral thesis is just a start and proof of concept for numerous promising applications of picosecond infrared laser in a variety of biomedical research areas. The unique advantages of PIRL make it an ideal tool for MS analysis towards the complete deciphering of the spatial and constitutional information on the single cellular level.

Bibliography

[1] Martin Chaplin, *Do we underestimate the importance of water in cell biology?*, Nature Reviews Molecular Cell Biology **7**(11), 861 (2006).

[2] Kresimir Franjic and R. J. Dwayne Miller, *Vibrationally excited ultrafast thermodynamic phase transitions at the water/air interface*, Physical Chemistry Chemical Physics **1**2(20), 5225 (2010).

[3] Bradley J Siwick, Jason R Dwyer, Robert E Jordan, and RJ Dwayne Miller, *An atomic-level view of melting using femtosecond electron diffraction*, Science **3**02(5649), 1382 (2003).

[4] AH Narten and HA Levy, *Water: A Comprehensive Treatise vol 1, ed F Franks* (1972).

[5] Philip Ball, *Water: water–an enduring mystery*, Nature **4**52(7185), 291 (2008).

[6] M. L. Cowan, B. D. Bruner, N. Huse, J. R. Dwyer, B. Chugh, E. T. J. Nibbering, T. Elsaesser, and R. J. D. Miller, *Ultrafast memory loss and energy redistribution in the hydrogen bond network of liquid H_2O*, Nature **4**34(7030), 199 (2005).

[7] KL Vodopyanov, *Saturation studies of H_2O and HDO near 3400 cm^{-1} using intense picosecond laser pulses*, The Journal of chemical physics **9**4(8), 5389 (1991).

[8] Stefan Berkenkamp, Michael Karas, and Franz Hillenkamp, *Ice as a matrix for IR-matrix-assisted laser desorption/ionization: mass spectra from a protein*

single crystal, Proceedings of the National Academy of Sciences **9**3(14), 7003 (1996).

[9] Guillaume Robichaud, Jeremy A Barry, and David C Muddiman, *IR-MALDESI mass spectrometry imaging of biological tissue sections using ice as a matrix*, Journal of the American Society for Mass Spectrometry **2**5(3), 319 (2014).

[10] Fan Huang and Kermit K. Murray, *Continuous flow infrared matrix-assisted laser desorption electrospray ionization mass spectrometry*, Rapid Communications in Mass Spectrometry **2**4(19), 2799 (2010).

[11] Peter Nemes and Akos Vertes, *Laser Ablation Electrospray Ionization for Atmospheric Pressure, in Vivo, and Imaging Mass Spectrometry*, Analytical Chemistry **7**9(21), 8098 (2007).

[12] Elizabeth J. Judge, John J. Brady, and Robert J. Levis, *Mass Analysis of Biological Macromolecules at Atmospheric Pressure Using Nonresonant Femtosecond Laser Vaporization and Electrospray Ionization*, Analytical Chemistry **8**2(24), 10203 (2010).

[13] Paul Flanigan and Robert Levis, *Ambient femtosecond laser vaporization and nanosecond laser desorption electrospray ionization mass spectrometry*, Annual Review of Analytical Chemistry **7**, 229 (2014).

[14] J Throck Watson and O David Sparkman, *Introduction to mass spectrometry: instrumentation, applications, and strategies for data interpretation* (John Wiley & Sons, 2007).

[15] Zoltán Takáts, Justin M. Wiseman, and R. Graham Cooks, *Ambient mass spectrometry using desorption electrospray ionization (DESI): instrumentation, mechanisms and applications in forensics, chemistry, and biology*, Journal of Mass Spectrometry **4**0(10), 1261 (2005).

[16] Malcolm Dole, LL Mack, RL Hines, RC Mobley, LD Ferguson, and MB d

Alice, *Molecular beams of macroions*, The Journal of Chemical Physics **4**9(5), 2240 (1968).

[17] J. V. Iribarne and B. A. Thomson, *On the evaporation of small ions from charged droplets*, The Journal of Chemical Physics **6**4(6), 2287 (1976).

[18] Paul Kebarle and Udo H. Verkerk, *Electrospray: from ions in solution to ions in the gas phase, what we know now*, Mass spectrometry reviews **2**8(6), 898 (2009).

[19] Lars Konermann, Elias Ahadi, Antony D Rodriguez, and Siavash Vahidi, *Unraveling the mechanism of electrospray ionization* (2012).

[20] Zoltán Takáts, Justin M Wiseman, Bogdan Gologan, and R Graham Cooks, *Mass spectrometry sampling under ambient conditions with desorption electrospray ionization*, Science **3**06(5695), 471 (2004).

[21] Peter Nemes and Akos Vertes, *Laser Ablation Electrospray Ionization for Atmospheric Pressure Molecular Imaging Mass Spectrometry* (Humana Press, Totowa, NJ, 2010), 159–171.

[22] Peter Nemes and Akos Vertes, *Ambient mass spectrometry for in vivo local analysis and in situ molecular tissue imaging*, TrAC Trends in Analytical Chemistry **3**4, 22 (2012).

[23] Bindesh Shrestha and Akos Vertes, *High-Throughput Cell and Tissue Analysis with Enhanced Molecular Coverage by Laser Ablation Electrospray Ionization Mass Spectrometry Using Ion Mobility Separation*, Analytical Chemistry **8**6(9), 4308 (2014).

[24] Jing Zou, Francis Talbot, Alessandra Tata, Leonardo Ermini, Kresimir Franjic, Manuela Ventura, Jinzi Zheng, Howard Ginsberg, Martin Post, Demian R. Ifa, David Jaffray, R. J. Dwayne Miller, and Arash Zarrine-Afsar, *Ambient Mass Spectrometry Imaging with Picosecond Infrared Laser Ablation Electrospray Ionization (PIR-LAESI)*, Analytical Chemistry **8**7(24), 12071 (2015).

[25] Peter B. O'Connor and Franz Hillenkamp, *MALDI Mass Spectrometry Instrumentation* (Wiley-VCH Verlag GmbH & Co. KGaA, 2007), 29–82.

[26] Michael Karas, Doris Bachmann, and Franz Hillenkamp, *Influence of the wavelength in high-irradiance ultraviolet laser desorption mass spectrometry of organic molecules*, Analytical chemistry **57**(14).

[27] Michael Karas, Doris Bachmann, U el Bahr, and Franz Hillenkamp, *Matrix-assisted ultraviolet laser desorption of non-volatile compounds*, International journal of mass spectrometry and ion processes **7**8, 53 (1987).

[28] Michael Karas and Franz Hillenkamp, *Laser desorption ionization of proteins with molecular masses exceeding 10,000 daltons*, Analytical Chemistry **6**0(20), 2299 (1988).

[29] A Overberg, M Karas, U Bahr, R Kaufmann, and F Hillenkamp, *Matrix-assisted infrared-laser (2.94 μm) desorption/ionization mass spectrometry of large biomolecules*, Rapid Communications in mass spectrometry **4**(8), 293 (1990).

[30] Michael Karas and Ralf Krüger, *Ion formation in MALDI: the cluster ionization mechanism*, Chemical reviews **1**03(2), 427 (2003).

[31] Michael Karas, Matthias Glückmann, and Jürgen Schäfer, *Ionization in matrix-assisted laser desorption/ionization: singly charged molecular ions are the lucky survivors*, Journal of Mass Spectrometry **3**5(1), 1 (2000).

[32] R Knochenmuss, A Stortelder, K Breuker, and R Zenobi, *Secondary ion–molecule reactions in matrix-assisted laser desorption/ionization*, Journal of mass spectrometry **3**5(11), 1237 (2000).

[33] Stefan Berkenkamp, Michael Karas, and Franz Hillenkamp, *Ice as a matrix for IR-matrix-assisted laser desorption/ionization: mass spectra from a protein single crystal*, Proceedings of the National Academy of Sciences **9**3(14), 7003 (1996).

[34] Christopher E Von Seggern, Ben D Gardner, and Robert J Cotter, *Infrared atmospheric pressure MALDI ion trap mass spectrometry of frozen samples using a Peltier-cooled sample stage*, Analytical chemistry **7**6(19), 5887 (2004).

[35] Alexander Pirkl, Jens Soltwisch, Felix Draude, and Klaus Dreisewerd, *Infrared Matrix-Assisted Laser Desorption/Ionization Orthogonal-Time-of-Flight Mass Spectrometry Employing a Cooling Stage and Water Ice As a Matrix*, Analytical Chemistry **8**4(13), 5669 (2012).

[36] Victor V. Laiko, Nelli I. Taranenko, Vadym D. Berkout, Mikhail A. Yakshin, Coorg R. Prasad, H. Sang Lee, and Vladimir M. Doroshenko, *Desorption/ionization of biomolecules from aqueous solutions at atmospheric pressure using an infrared laser at 3 μm*, Journal of the American Society for Mass Spectrometry **1**3(4), 354 (2002).

[37] Yue Li, Bindesh Shrestha, and Akos Vertes, *Atmospheric pressure molecular imaging by infrared MALDI mass spectrometry*, Analytical Chemistry **7**9(2), 523 (2007).

[38] Kenzo Hiraoka, Shimpei Saito, Jun Katsuragawa, and Ichiro Kudaka, *A new liquid chromatography/mass spectrometry interface: laser spray*, Rapid Communications in Mass Spectrometry **1**2(17), 1170 (1998).

[39] Ichiro Kudaka, Takanori Kojima, Shinpei Saito, and Kenzo Hiraoka, *A comparative study of laser spray and electrospray*, Rapid Communications in Mass Spectrometry **1**4(16), 1558 (2000).

[40] Kenzo Hiraoka, *Laser spray: electric field-assisted matrix-assisted laser desorption/ionization*, Journal of Mass Spectrometry **3**9(4), 341 (2004).

[41] Atsushi Takamizawa, Yoshiyuki Itoh, Ryo Osawa, Noriyuki Iwasaki, Yoshifumi Nishimura, Satoko Akashi, and Kenzo Hiraoka, *Selective dissociation of non-covalent bonds in biological molecules by laser spray*, Journal of Mass Spectrometry **3**9(9), 1053 (2004).

[42] Atsushi Takamizawa, Susumu Fujimaki, Jan Sunner, and Kenzo Hiraoka, *Denaturation of Lysozyme and Myoglobin in Laser Spray*, Journal of the American Society for Mass Spectrometry **1**6(6), 860 (2005).

[43] Atsumu Hirabayashi, Minoru Sakairi, and Hideaki Koizumi, *Sonic spray mass spectrometry*, Analytical Chemistry **6**7(17), 2878 (1995).

[44] Scott R. Heron, Rab Wilson, Scott A. Shaffer, David R. Goodlett, and Jonathan M. Cooper, *Surface Acoustic Wave Nebulization of Peptides As a Microfluidic Interface for Mass Spectrometry*, Analytical Chemistry **8**2(10), 3985 (2010).

[45] Yue Huang, Sung Hwan Yoon, Scott R. Heron, Christophe D. Masselon, J. Scott Edgar, Franti ek Ture ek, and David R. Goodlett, *Surface Acoustic Wave Nebulization Produces Ions with Lower Internal Energy than Electrospray Ionization*, Journal of The American Society for Mass Spectrometry **2**3(6), 1062 (2012).

[46] Sung Hwan Yoon, Yue Huang, J. Scott Edgar, Ying S. Ting, Scott R. Heron, Yuchieh Kao, Yanyan Li, Christophe D. Masselon, Robert K. Ernst, and David R. Goodlett, *Surface Acoustic Wave Nebulization Facilitating Lipid Mass Spectrometric Analysis*, Analytical Chemistry **8**4(15), 6530 (2012).

[47] Atsumu Hirabayashi, Minoru Sakairi, and Hideaki Koizumi, *Sonic Spray Ionization Method for Atmospheric Pressure Ionization Mass Spectrometry*, Analytical Chemistry **6**6(24), 4557 (1994).

[48] Atsumu Hirabayashi, Yukiko Hirabayashi, Minoru Sakairi, and Hideaki Koizumi, *Multiply-charged Ion Formation by Sonic Spray*, Rapid communications in mass spectrometry **1**0(13), 1703 (1996).

[49] Yukiko Hirabayashi, Atsumu Hirabayashi, Yasuaki Takada, Minoru Sakairi, and Hideaki Koizumi, *A sonic spray interface for the mass analysis of highly*

charged ions from protein solutions at high flow rates, Analytical chemistry **7**0(9), 1882 (1998).

[50] Zoltán Takáts, Sergio C. Nanita, R. Graham Cooks, Gitta Schlosser, and Karoly Vekey, *Amino Acid Clusters Formed by Sonic Spray Ionization*, Analytical Chemistry **7**5(6), 1514 (2003).

[51] Zoltán Takáts, Justin M. Wiseman, Bogdan Gologan, and R. Graham Cooks, *Electrosonic Spray Ionization. A Gentle Technique for Generating Folded Proteins and Protein Complexes in the Gas Phase and for Studying Ion-Molecule Reactions at Atmospheric Pressure*, Analytical Chemistry **7**6(14), 4050 (2004).

[52] Nicholas D. Chubatyi, Tongwen Wang, and Charles N. McEwen, *More inclusive or selective ionization for mass spectrometry using obstructive sonic spray ionization and voltage polarity switching*, Rapid Communications in Mass Spectrometry **2**6(23), 2763 (2012).

[53] Atsumu Hirabayashi, *Enhanced Ion Evaporation by Fast Gas Flow in Nano-Sonic Spray Ionization (nano-SSI)*, Journal of the Mass Spectrometry Society of Japan **6**0(4), 43 (2012).

[54] Abdil Ozdemir, Jung-Lee Lin, Yi Sheng Wang, and Chung-Hsuan Chen, *A deeper look into sonic spray ionization*, RSC Advances **4**(106), 61290 (2014).

[55] Ruedi Aebersold and Matthias Mann, *Mass spectrometry-based proteomics*, Nature **4**22(6928), 198 (2003).

[56] C. R. Blakley and M. L. Vestal, *Thermospray interface for liquid chromatography/mass spectrometry*, Analytical Chemistry **5**5(4), 750 (1983).

[57] John A. Koropchak, Marjan Veber, and Richard F. Browner, *Thermospray Sample Introduction to Atomic Spectrometry*, Critical Reviews in Analytical Chemistry **2**3(3), 113 (1992).

[58] Viswanatham Katta, Alan L. Rockwood, and Marvin L. Vestal, *Field limit for*

ion evaporation from charged thermospray droplets, International Journal of Mass Spectrometry and Ion Processes **1**03(2), 129 (1991).

[59] Marvin L. Vestal, *Ionization techniques for nonvolatile molecules*, Mass Spectrometry Reviews **2**(4), 447 (1983).

[60] Vincent S. Pagnotti, Nicholas D. Chubatyi, and Charles N. McEwen, *Solvent Assisted Inlet Ionization: An Ultrasensitive New Liquid Introduction Ionization Method for Mass Spectrometry*, Analytical Chemistry **8**3(11), 3981 (2011).

[61] Vincent S. Pagnotti, Shubhashis Chakrabarty, Andrew F. Harron, and Charles N. McEwen, *Increasing the Sensitivity of Liquid Introduction Mass Spectrometry by Combining Electrospray Ionization and Solvent Assisted Inlet Ionization*, Analytical Chemistry **8**4(15), 6828 (2012).

[62] Vincent S. Pagnotti, Shubhashis Chakrabarty, Beixi Wang, Sarah Trimpin, and Charles N. McEwen, *Gas-Phase Ions Produced by Freezing Water or Methanol for Analysis Using Mass Spectrometry*, Analytical Chemistry **8**6(15), 7343 (2014).

[63] Michael Wleklinski, Yafeng Li, Soumabha Bag, Depanjan Sarkar, Rahul Narayanan, T Pradeep, and R Graham Cooks, *Zero volt paper spray ionization and its mechanism*, Analytical chemistry **8**7(13), 6786 (2015).

[64] Satoshi Ashihara, Nils Huse, Agathe Espagne, Erik T. J. Nibbering, and Thomas Elsaesser, *Ultrafast Structural Dynamics of Water Induced by Dissipation of Vibrational Energy*, J. Phys. Chem. A **1**11(5), 743 (2007).

[65] Satoshi Ashihara, Nils Huse, Agathe Espagne, Erik T. J. Nibbering, and Thomas Elsaesser, *Vibrational couplings and ultrafast relaxation of the Oï¿½-H bending mode in liquid H_2O*, Chem. Phys. Lett. **4**24, 66 (2006).

[66] Nils Huse, Haidan Wen, Dennis Nordlund, Erzsi Szilagyi, Dan Daranciang, Timothy A. Miller, Anders Nilsson, Robert W. Schoenlein, and Aaron M.

Lindenberg, *Probing the hydrogen-bond network of water via time-resolved soft x-ray spectroscopy*, Phys. Chem. Chem. Phys. **1**1(20), 3951 (2009).

[67] Haidan Wen, Nils Huse, Robert W. Schoenlein, and Aaron M. Lindenberg, *Ultrafast conversions between hydrogen bonded structures in liquid water observed by femtosecond x-ray spectroscopy*, J. Chem. Phys. **1**31, 234505 (2009).

[68] Saeid Amini-Nik, Darren Krämer, Michael L. Cowan, Keith Gunaratne, Puviindran Nadesan, Benjamin A. Alman, and R. J. Dwayne Miller, *Ultrafast Mid-IR Laser Scalpel: Protein Signals of the Fundamental Limits to Minimally Invasive Surgery*, PLoS ONE **5**(9), e13053 (2010).

[69] Hannes Petersen, Fatemeh Tavakoli, Sebastian Kruber, Adrian Münscher, Alexandra Gliese, Nils-Owe Hansen, Stephanie Uschold, Dennis Eggert, Wesley D. Robertson, Tobias Gosau, Susanne Sehner, Marcel Kwiatkowski, Hartmut Schlüter, Udo Schumacher, Rainald Knecht, and R. J. Dwayne Miller, *Comparative study of wound healing in rat skin following incision with a novel picosecond infrared laser (PIRL) and different surgical modalities*, Lasers in Surgery and Medicine **4**8(4), 385 (2016).

[70] Arne Böttcher, Till S Clauditz, Rainald Knecht, Stanislav Kucher, Wolfgang Wöllmer, Waldemar Wilczak, Peter Krötz, Nathan Jowett, Carsten V Dalchow, Adrian Münscher, *et al.*, *A novel tool in laryngeal surgery: preliminary results of the picosecond infrared laser*, The Laryngoscope **1**23(11), 2770 (2013).

[71] Arne Böttcher, Stanislav Kucher, Rainald Knecht, Nathan Jowett, Peter Krötz, Rudolph Reimer, Udo Schumacher, Sven Anders, Adrian MÃ$\frac{1}{4}$nscher, CarstenV Dalchow, and R. J. Dwayne Miller, *Reduction of thermocoagulative injury via use of a picosecond infrared laser (PIRL) in laryngeal tissues*, European Archives of Oto-Rhino-Laryngology **2**72(4), 941 (2015).

[72] Markus Hess, Michael Dominik Hildebrandt, Frank Mueller, Sebastian Kruber, Peter Kroetz, Udo Schumacher, Rudolph Reimer, Michael Kammal, Klaus

Pueschel, Wolfgang Woellmer, and Dwayne Miller, *Picosecond infrared laser (PIRL): an ideal phonomicrosurgical laser?*, European Archives of Oto-Rhino-Laryngology **2**70(11), 2927 (2013).

[73] Nathan Jowett, Wolfgang Wöllmer, Alex M Mlynarek, Paul Wiseman, Bernard Segal, Kresimir Franjic, Peter Krötz, Arne Böttcher, Rainald Knecht, and RJ Dwayne Miller, *Heat generation during ablation of porcine skin with erbium: YAG laser vs a novel picosecond infrared laser*, JAMA Otolaryngology–Head & Neck Surgery **1**39(8), 828 (2013).

[74] Nathan Jowett, Wolfgang Wöllmer, Rudolph Reimer, Jozef Zustin, Udo Schumacher, Paul W Wiseman, Alex M Mlynarek, Arne Böttcher, Carsten V Dalchow, Balazs B Lörincz, *et al.*, *Bone ablation without thermal or acoustic mechanical injury via a novel picosecond infrared laser (PIRL)*, Otolaryngology–Head and Neck Surgery **1**50(3), 385 (2014).

[75] Stephan J. Linke, Andreas Frings, Ling Ren, Amadeus Gomolka, Udo Schumacher, Rudolph Reimer, Nils-Owe Hansen, Nathan Jowett, Gisbert Richard, and R. J. Dwayne Miller, *A New Technology for Applanation Free Corneal Trephination: The Picosecond Infrared Laser (PIRL)*, PLOS ONE **1**0(3), e0120944 (2015).

[76] L Ren, W D Robertson, R Reimer, C Heinze, C Schneider, D Eggert, P Truschow, N-O Hansen, P Kroetz, J Zou, and R J D Miller, *Towards instantaneous cellular level bio diagnosis: laser extraction and imaging of biological entities with conserved integrity and activity*, Nanotechnology **2**6(28), 284001 (2015).

[77] Marcel Kwiatkowski, Marcus Wurlitzer, Maryam Omidi, Ling Ren, Sebastian Kruber, Refat Nimer, Wesley D Robertson, Andrea Horst, RJ Miller, and Hartmut SchlÃ$\frac{1}{4}$ter, *Ultrafast extraction of proteins from tissues using desorption by impulsive vibrational excitation*, Angewandte Chemie International Edition **5**4(1), 285 (2015).

[78] M. Kwiatkowski, M. Wurlitzer, A. Krutilin, P. Kiani, R. Nimer, M. Omidi, A. Mannaa, T. Bussmann, K. Bartkowiak, S. Kruber, S. Uschold, P. Steffen, J. LÃ$\frac{1}{4}$bberstedt, N. KÃ$\frac{1}{4}$pker, H. Petersen, R. Knecht, N. O. Hansen, A. Zarrine-Afsar, W. D. Robertson, R. J. D. Miller, and H. SchlÃ$\frac{1}{4}$ter, *Homogenization of tissues via picosecond-infrared laser (PIRL) ablation: Giving a closer view on the in-vivo composition of protein species as compared to mechanical homogenization*, Journal of Proteomics **1**34, 193 (2016).

[79] J Zou, C Wu, WD Robertson, LV Zhigilei, and RJD Miller, *Molecular dynamics investigation of desorption and ion separation following picosecond infrared laser (PIRL) ablation of an ionic aqueous protein solution*, The Journal of Chemical Physics **1**45(20), 204202 (2016).

[80] Petra S Dittrich and Andreas Manz, *Lab-on-a-chip: microfluidics in drug discovery*, Nature Reviews Drug Discovery **5**(3), 210 (2006).

[81] Nauman Khalid, Isao Kobayashi, and Mitsutoshi Nakajima, *Recent lab-on-chip developments for novel drug discovery*, Wiley Interdisciplinary Reviews: Systems Biology and Medicine , e1381E1381 (2017).

[82] Yinfei Lu, Cornelius L. Pieterse, Wesley D. Robertson, and R.J.Dwayne Miller, *Soft Picosecond Infrared Laser Extraction of Highly Charged Proteins and Peptides from Bulk Liquid Water for Mass Spectrometry*, Analytical chemistry, submitted .

[83] Matthias Conradin Jecklin, David Touboul, CÃ©dric Bovet, Arno Wortmann, and Renato Zenobi, *Which electrospray-based ionization method best reflects protein-ligand interactions found in solution? A comparison of ESI, nanoESI, and ESSI for the determination of dissociation constants with mass spectrometry*, Journal of the American Society for Mass Spectrometry **1**9(3), 332 (2011).

[84] Yi Zhang, Nitin Mehrotra, Nageshwar R. Budha, Michael L. Christensen, and Bernd Meibohm, *A tandem mass spectrometry assay for the simultaneous*

determination of acetaminophen, caffeine, phenytoin, ranitidine, and theophylline in small volume pediatric plasma specimens, Clinica Chimica Acta **3**98(1–2), 105 (2008).

[85] R.K. Gilpin and W. Zhou, *Studies of the Thermal Degradation of Acetaminophen Using a Conventional HPLC Approach and Electrospray Ionization-Mass Spectrometry*, Journal of Chromatographic Science **4**2(1), 15 (2004).

[86] P. Roepstorff and J. Fohlman, *Letter to the editors*, Biological Mass Spectrometry **1**1(11), 601 (1984).

[87] T. D. Wood, R. A. Chorush, F. M. Wampler, D. P. Little, P. B. O'Connor, and F. W. McLafferty, *Gas-phase folding and unfolding of cytochrome c cations*, Proceedings of the National Academy of Sciences of the United States of America **9**2(7), 2451 (1995).

[88] David S. Wagner and Robert J. Anderegg, *Conformation of Cytochrome c Studied by Deuterium Exchange-Electrospray Ionization Mass Spectrometry*, Analytical Chemistry **6**6(5), 706 (1994).

[89] Lars Konermann and D. J. Douglas, *Unfolding of proteins monitored by electrospray ionization mass spectrometry: a comparison of positive and negative ion modes*, Journal of the American Society for Mass Spectrometry **9**(12), 1248 (1998).

[90] Maria Šamalikova, Irena Matečko, Norbert Müller, and Rita Grandori, *Interpreting conformational effects in protein nano-ESI-MS spectra*, Analytical and bioanalytical chemistry **3**78(4), 1112 (2004).

[91] Jiangjiang Liu and Lars Konermann, *Irreversible Thermal Denaturation of Cytochrome c Studied by Electrospray Mass Spectrometry*, Journal of the American Society for Mass Spectrometry **2**0(5), 819 (2009).

[92] Michael Wleklinski, Yafeng Li, Soumabha Bag, Depanjan Sarkar, Rahul

Narayanan, T. Pradeep, and R. Graham Cooks, *Zero Volt Paper Spray Ionization and Its Mechanism*, Analytical Chemistry **8**7(13), 6786 (2015).

[93] JN Israelachvili, *Intermolecular and Surface Forces (revised 3rd edition) Academic Press*, Waltham, MA (2011).

[94] Edward E. Dodd, *The Statistics of Liquid Spray and Dust Electrification by the Hopper and Laby Method*, Journal of Applied Physics **2**4(1), 73 (1953).

[95] Denis Duft, Tobias Achtzehn, Rene Müller, Bernd A Huber, and Thomas Leisner, *Coulomb fission: Rayleigh jets from levitated microdroplets*, Nature **4**21(6919), 128 (2003).

[96] Lloyd W. Zilch, Joshua T. Maze, John W. Smith, George E. Ewing, and Martin F. Jarrold, *Charge Separation in the Aerodynamic Breakup of Micrometer-Sized Water Droplets*, The Journal of Physical Chemistry A **1**12(51), 13352 (2008).

[97] Sarah Trimpin, Beixi Wang, Ellen D. Inutan, Jing Li, Christopher B. Lietz, Andrew Harron, Vincent S. Pagnotti, Diana Sardelis, and Charles N. McEwen, *A Mechanism for Ionization of Nonvolatile Compounds in Mass Spectrometry: Considerations from MALDI and Inlet Ionization*, Journal of The American Society for Mass Spectrometry **2**3(10), 1644 (2012).

[98] George M Whitesides, *The origins and the future of microfluidics*, Nature **4**42(7101), 368 (2006).

[99] Rosamund Daw and Joshua Finkelstein, *Insight: Lab on a chip*, Nature **4**42(7101), 367 (2006).

[100] Mian Yang, Randall Nelson, and Alexandra Ros, *Toward analysis of proteins in single cells: a quantitative approach employing isobaric tags with MALDI mass spectrometry realized with a microfluidic platform*, Analytical chemistry **8**8(13), 6672 (2016).

[101] R Daniel Pedde, Huiyan Li, Christoph H Borchers, and Mohsen Akbari, *Microfluidic-Mass Spectrometry Interfaces for Translational Proteomics*, Trends in Biotechnology (2017).

[102] Daniel Figeys, *Adapting arrays and lab-on-a-chip technology for proteomics*, Proteomics **2**(4), 373 (2002).

[103] RJ Beulig, R Warias, JJ Heiland, S Ohla, K Zeitler, and D Belder, *A droplet-chip/mass spectrometry approach to study organic synthesis at nanoliter scale*, Lab on a Chip **1**7(11), 1996 (2017).

[104] Kiarach Mesbah, Robert Thai, Sarah Bregant, and Florent Malloggi, *DMF-MALDI: droplet based microfluidic combined to MALDI-TOF for focused peptide detection*, Scientific Reports **7** (2017).

[105] Eric K Sackmann, Anna L Fulton, and David J Beebe, *The present and future role of microfluidics in biomedical research*, Nature **5**07(7491), 181 (2014).

[106] Jamil El-Ali, Peter K Sorger, and Klavs F Jensen, *Cells on chips*, Nature **4**42(7101), 403 (2006).

[107] Arash Zarrine-Afsar, Christina MÃ$\frac{1}{4}$ller, Francis O. Talbot, and R. J. Dwayne Miller, *Self-Localizing Stabilized Mega-Pixel Picoliter Arrays with Size-Exclusion Sorting Capabilities*, Analytical Chemistry **8**3(3), 767 (2011).

[108] Wesley D. Robertson, Lucas R. Porto, Candice J. X. Ip, Megan K. T. Nantel, Friedjof Tellkamp, Yinfei Lu, and R. J. Dwayne Miller, *Note: A simple image processing based fiducial auto-alignment method for sample registration*, Review of Scientific Instruments **8**6(8), 086105 (2015).

Abbreviations

AP: Atmospheric pressure

APCI: atmospheric pressure chemical ionization

CID-MS/MS: collision induced dissociation spectrum

CRM: charged residue model

DESI: desorption by electrospray ionization

DIVE: desorption by impulsive vibrational excitation

DMPS: diferential mobility particle size analyzer

ESSI: eletrosonic spray ionization

HPLC: high performance liquid chromatography

IDT: interdigitated piezoelectric transducer

IEM: ion evaporation model

IR-MALDESI: infrared matrix-assisted laser desorption electrospray ionization

IR-MALDESI: IR matrix-assisted laser desorption electrospray ionization

LAESI: laser ablation electrospray ionization

LC: liquid chromatography

LOC:lab-on-a-chip

LOD: limit of detection

MALDI: matrix-assisted inlet ionization

MS: mass spectrometry

PECVD: plasma-enhanced chemical vapor deposition

pI: isoelectrical point

PIRL: picosecond infrared laser

PIR-LAESI: picosecond infrared laser ablation electrospray ionization

PS: paper spray

SAII: solvent assisted Inlet ionization

SAWN: surface acoustic wave nebulization

SSI: sonic spray ionization

List of Publications

Publications in Refereed Journals

1. **Yinfei Lu**, Cornelius L. Pieterse, Wesley D. Robertson, and R. J. Dwayne Miller, *Soft Picosecond Infrared Laser Extraction of Highly Charged Proteins and Peptides from Bulk Liquid Water for Mass Spectrometry*, submitted to Analytical Chemistry

2. **Yinfei Lu**, Cornelius L. Pieterse, Dennis Eggert, Candice Ip, Frederik Busse, Sercan Kersin, Wesley D. Robertson, and R. J. Dwayne Miller, *Matrix-Free Laser Sampling of Water from Lab-on-a-Chip Devices for Mass Spectrometry*, manuscript in preparation

3. Wesley D. Robertson, Lucas R. Porto, Candice J. X. Ip, Megan K. T. Nantel, Friedjof Tellkamp, **Yinfei Lu**, and R. J. Dwayne Miller, *Note: A simple image processing based fiducial auto-alignment method for sample registration*, Review of Scientic Instruments 86(8), 086105 (2015).

Talks and Posters

1. **Yinfei Lu**, Cornelius L. Pieterse, Jean-Michel Boudreau, Frederik Busse, Wesley D. Robertson, and R. J. Dwayne Miller, *Direct Picosecond Infrared Laser (PIRL) Extraction of Highly Charged Biomolecules, Native Proteins and Non-Covalently Bound Protein Ligand Complexed from Bulk Water*, Oral presentation, Pittsburgh Conference on Analytical Chemistry and Applied Spectroscopy (PittCon), March 2017, Chicago

2. **Yinfei Lu**, Cornelius L. Pieterse, Wesley D. Robertson, and R. J. Dwayne Miller, *Atmospheric picosecond IR laser desorption by impulsive vibrational excitation mass spectrometry (PIRL-DIVE-MS)*, Poster, DPG-Frühjahrstagung 2016, Hannover

Acknowledgement

During my doctoral study, lots of people have offered me their great support, which has facilitated the completion of this thesis. First I would like to express my deepest gratitude to my supervisor Prof. R.J. Dwayne Miller for offering me this great opportunity to work on this exciting project. His supervision and advice have been accompanying me through every stage of my PhD to the final success in completing this thesis. His passion and optimism in academic research always inspire and encourage me to conquer the difficulties I meet during my research. I would like to also give my sincere thankfulness to my co-supervisor Prof. Nils Huse, who is always there to help me when I encountered confusions on my project and offers extremely important strategic advice.

I would like to thank Dr. Wesley D. Robertson, who is leading the DIVE-MS project. He has supported me from the start of my project and encouraged me by saying 'this is not the end of the world' when I failed with experiments or made mistakes. I would like to thank Cornelius Louwrens Pieterse for fruitful discussions and considerable amount of valuable time working together to solve problems of the experiments. I would like to thank Prof. Arwen Pearson for useful advice on the projects. I would like to thank Prof. Helmut Schlüter and Dr. Nils-Owe Hansen for initiating the superPIRL project from the UKE side. I would like to thank the former and current members of this joint project: Elke Gengler, Ling Ren, Frederik Busse, Johannes Kaub, Andrey Krutilin, Stephanie Maier, and Sebastian Kruber.

I would like to thank the former and current IMPRS coordinators Anja Bleidorn, Dr. Sonia Utermann, and Dr. Julia Quante for their fantastic jobs to support and help me during my PhD study. I would like to thank Gisbert Mantei for the great support to maintain our lab. I would like to thank the former and current group secretaries Nadja Bardenheuer and Christine Fricke for administrative help. I would like to thank our wonderful engineers Josef Gonschior and Djordje Gitaric for their design of the components of my projects. I would like to thank all the intern students who ever worked with me: Han Zhang, Erik Frieling, Jean-Michel Boudreau, Candice Ip, and Megan Nantel.

I would like to thank all my friends who ever shared happiness with me, and cheered me up even when I was extremely frustrated.

I would like to express my admiration to the scientific pioneers from my family, Prof. Rao Yu-Tai, who was one of the founders of modern physics in China. I learned from his example how one individual can change his country. I would like to thank my grandfather Prof. Zhou Bang-Ji, who is one of the founders of the polymer industry in China, for his attitude and methodology on doing research. I would like to thank my parents Zhou Hong and Lu Gang for their constant support and unconditional love. I would like to thank all other family members for their caring for me.

I would like to thank my boyfriend Dr. Oliver D. Mücke for his endless love and being my rock and soulmate.